Centro de Investigaciones Energéticas,
Medioambientales y Tecnológicas, Madrid

Departamento de Física Teórica y del Cosmos
Facultad de Ciencias de la Universidad de Granada

Ciemat
Centro de Investigaciones
Energéticas, Medioambientales
y Tecnológicas

Measurement of the Cosmic Muon Charge Ratio Using CMS Data and Discovery Potential of the Standard Model Higgs Boson in the $H \to ZZ^{(*)} \to 4\mu$ Channel

María Aldaya Martín

Memoria de tesis presentada
para optar al grado de Doctora en Física
Dirigida por el
Dr. Pablo García Abia (CIEMAT)

Madrid, Mayo 2008

Editor: Editorial de la Universidad de Granada
Autor: María Aldaya Martín
D.L.: GR.1610-2008
ISBN: 978-84-691-4846-4

Contents

Introduction

The Standard Model of particle physics is the currently accepted theory for the quantitative descriptions of the interactions of fundamental particles. Its validity up to the present energies (electroweak scale, a few hundred GeV) has been experimentally tested at the per mille level accuracy by the high-precision measurements of the last decades carried out at LEP, SLC and Tevatron. In spite of all, the Standard Model is still not completely satisfactory.

A cornerstone of the Standard Model is the mechanism of spontaneous electroweak symmetry breaking proposed to generate the masses of all the observed elementary particles by introducing a doublet of complex scalar fields. This so-called Higgs mechanism predicts the existence of one scalar particle, the Higgs boson, whose mass is the only unknown fundamental parameter of the theory. However, the Higgs particle has not been observed in experiments so far and only indirect constraints on its mass have been inferred from the high-precision data. Moreover, there are several reasons to believe that the Standard Model is only an effective description of the structure of matter up to some scale $\Lambda \approx$ TeV and that there must be a truly fundamental underlying theory.

Most of the extensions of the theory that have been proposed to solve the shortcomings of the Standard Model have a common intriguing feature: they predict the existence of new physics phenomena not considered by the Standard Model at the TeV energy scale, thus requiring energies higher than those reached by present particle accelerators.

This led to the design of the Large Hadron Collider (LHC), a high-energy, high-luminosity proton-proton collider, which is being installed at the European Laboratory for Nuclear Research (CERN) in Geneva (Switzerland) and will deliver the first beams in the summer of 2008. With a center-of-mass collision energy of $\sqrt{s} = 14$ TeV and a design luminosity of $2 \times 10^{34}\ \mathrm{cm}^{-2}\,\mathrm{s}^{-1}$, it is a machine of unprecedented complexity and potential. It will be the first accelerator to provide parton-parton collisions up to energies of about 1 TeV, the energy scale relevant to electroweak symmetry breaking and at which beyond the Standard Model phenomena are expected to appear.

One of the prime goals of LHC is to find the Higgs boson. If the Higgs boson exists, it will be able to be discovered by the Compact Muon Solenoid (CMS) experiment, one of the four detectors (together with ATLAS, LHCb and ALICE) that will operate at LHC. In order to exploit the experimental programme of LHC, we need a good understanding of the detector and the data to ensure the optimal performance of CMS when LHC delivers the first beams. In addition, we also need to prepare data analysis tools and develop analysis strategies to quantify the CMS discovery potential of the new physics we are looking for.

Since I started my Ph.D. in 2004, I have been involved in several tasks of the CMS experiment, from hardware commissioning to physics analysis. This thesis summarizes the research work I

have done as a member of the CMS collaboration in the CIEMAT group.

I have performed the first physics measurement using real data in CMS: the measurement of the cosmic ray muon charge ratio, which is the ratio of the number of positive- to negative-charge cosmic muons, obtained as a function of the muon momentum, using data collected at the *Magnet Test and Cosmic Challenge* (MTCC). The MTCC, a first combined test – on surface – of almost all subsystems of CMS, including the magnet, has been performed during the second half of 2006 using high energy muons from cosmic rays as a particle beam. Although the MTCC has been devoted to test the detector and physics studies are not among its primary goals, the large amount of high quality data collected has allowed performing measurements of physical quantities related to cosmic ray muons, which also provide a complementary check of the detector performance. We have succeeded to obtain a result of good quality, in agreement with previous measurements within the experimental uncertainty. For the CMS collaboration, it has meant a successful test of the complete analysis infrastructure that will be used with the data produced in the proton-proton collisions at LHC and a better understanding of the calibration and alignment procedures of the detector. This analysis is documented in a CMS Note[1] [1] and is described in the first part of the thesis (Chapter 2).

The second part of this dissertation presents the search analysis of the Standard Model Higgs boson in the $H \to ZZ^{(*)} \to 4\mu$ decay channel. It is a mass-independent, cut-based analysis using simulated data that exploits the log-likelihood ratio statistical method to quantify the CMS discovery potential of the Higgs boson signal, as a function of its mass, for integrated luminosities of 10 fb^{-1} and 30 fb^{-1} and in a wide range of masses. The method also allows the outlining of a search strategy for the Higgs boson, using confidence levels that characterize either the signal plus background or background likeliness of the data. I have participated in the selection of the simulated samples used in this analysis and have applied the log-likelihood ratio method to obtain the expected significance of the Higgs boson signal. This analysis is documented in a CMS Note [2] and described in Chapter 3. I have also developed, implemented and applied a fitting method to measure the Higgs boson mass, cross section and width in this channel. The fit is performed to the distribution of the reconstructed four-muon invariant mass, including the effect of the finite resolution of the detector, the internal bremsstrahlung radiation and the background contribution, and is used to obtain the precision in the determination of those parameters. This procedure is documented in a CMS Note [3] and described in Chapter 4. These two analyses, published in the CMS Physics TDR Vol.II [4], are official CMS results regarding the search for the Standard Model Higgs boson in the $H \to ZZ^{(*)} \to 4\mu$ channel.

The present thesis starts with an introductory chapter, in which a brief description of the Standard Model of particle physics, the Higgs boson physics and the experimental setup – LHC and CMS – is given. Then, the aforementioned analyses are described in detail (Chapters 2 to 4). Finally, the conclusions on the results of my research work are given in Chapter 5.

[1] CMS Notes are public documents that undergo an exhaustive revision process performed by editors and referees from the collaboration, and are only approved when their quality is considered that of a specialized paper.

Resumen (in Spanish)

El Modelo Estándar de física de partículas es la teoría aceptada en la actualidad para la descripción cuantitativa de las interacciones entre las partículas fundamentales. Las medidas de alta precisión de las últimas décadas, llevadas a cabo en los aceleradores LEP, SLC y Tevatron, han permitido confirmar experimentalmente su validez hasta el límite de las energías actuales (escala electrodébil, unos cientos de GeV), llegando a un nivel de precisión del 0.1%. A pesar de ello, el Modelo Estándar sigue sin ser completamente satisfactorio.

La piedra angular del Modelo Estándar es el mecanismo de ruptura espontánea de la simetría electrodébil, propuesto para generar las masas de todas las partículas elementales observadas mediante la introducción de un doblete de campos escalares complejos. El así llamado mecanismo de Higgs predice la existencia de una partícula escalar, el bosón de Higgs, cuya masa es el único parámetro fundamental no conocido de la teoría. La partícula de Higgs no ha sido observada en los experimentos hasta el momento y sólo ha sido posible inferir restricciones indirectas al valor de su masa a partir de los datos de alta precisión. Además, existen diversas razones para pensar que el Modelo Estándar es en realidad una descripción efectiva de la estructura de la materia hasta una escala de energía $\Lambda \approx$ TeV, y que debe haber una teoría subyacente verdaderamente fundamental.

Muchas de las extensiones de la teoría que se han propuesto para resolver los defectos del Modelo Estándar tienen una interesante característica en común: predicen la existencia de nuevos fenómenos físicos no contemplados en el Modelo Estándar a escalas de energía del orden del TeV y por tanto, requieren energías más altas de las alcanzadas hasta ahora en los aceleradores de partículas actuales para su verificación o rechazo.

Esto llevó al diseño del *Large Hadron Collider* (LHC), un colisionador protón-protón (pp) de alta energía y luminosidad, que está siendo instalado en el túnel de 26.6 km de circunferencia anteriormente utilizado por LEP, en el Laboratorio Europeo de Física de Partículas (CERN) en Ginebra (Suiza), y que entrará en funcionamiento en verano de 2008. Con una energía de colisión en el sistema de referencia de centro de masas de $\sqrt{s} = 14$ TeV y una luminosidad de diseño de 2×10^{34} cm^{-2} s^{-1}, es una máquina de complejidad y potencial sin precedentes. Será el primer acelerador que proporcione colisiones partón-partón a energías del orden del TeV, escala de energía relevante para la ruptura de la simetría electrodébil y a la que se espera que aparezcan fenómenos más allá del Modelo Estándar.

Uno de los principales objetivos de LHC es encontrar el bosón de Higgs. Si esta partícula existe, podrá ser descubierta en el experimento *Compact Muon Solenoid* (CMS), uno de los cuatro detectores (junto con ATLAS, ALICE y LHCb) que operarán en LHC. Se trata de un detector complejo, constituido por un barril cilíndrico cerrado por dos discos (*end-caps*), con

una longitud total de 21.6 m, un diámetro de 15 m y un peso total de unas 12500 toneladas. Su diseño está motivado por la elección de un intenso campo magnético solenoidal que permita una medida muy precisa del momento de las partículas cargadas y una excelente identificación de muones. En torno al imán superconductor se alojan los diversos subdetectores que componen CMS. Éstos se encuentran situados de forma concéntrica alrededor del tubo del haz. Desde el punto de interacción, situado en el centro del cilindro, hasta el exterior se encuentran: un detector central de trazas (*tracker*) encargado de medir con alta precisión el momento y la carga de las partículas cargadas generadas en la colisión; un calorímetro electromagnético (ECAL), que se encarga de detectar e identificar las partículas con interacción electromagnética; un calorímetro hadrónico (HCAL) hermético de muestreo, que permite la identificación de hadrones; el imán solenoidal superconductor, que proporciona un campo magnético uniforme de 4 T en su interior. Un espectrómetro de muones muy preciso y redundante, insertado en el hierro de retorno del imán y encargado de la detección e identificación de muones. El sistema de muones consta de tres subsistemas independientes: cámaras de tubos de deriva (DT) en el barril, cámaras CSC (*Cathode Strip Chamber*) en los *end-caps* y las llamadas *Resistive Plate Chambers* (RPC) en ambas zonas. La construcción del detector, a día de hoy, se encuentra finalizada, y se están llevando a cabo las últimas tareas de integración y puesta a punto de los distintos subsistemas que lo componen.

Una de las metas más importantes de CMS es el descubrimiento del bosón de Higgs tan pronto como sea posible. Esto requiere poseer un buen entendimiento del detector y de los datos que se recojan, para así garantizar el funcionamiento óptimo de CMS cuando los primeros haces empiecen a circular en el colisionador. Además, debemos preparar las herramientas de análisis de datos y desarrollar estrategias de análisis que nos permitan cuantificar el potencial de CMS para descubrir los nuevos fenómenos de física que estamos buscando.

Desde que empecé mi doctorado en 2004 he estado involucrada en diversas tareas dentro del experimento CMS, desde pruebas de *hardware* hasta análisis de física. Esta tesis resume el trabajo de investigación que he realizado como miembro de la colaboración CMS en el grupo de Física de Partículas del CIEMAT.

He realizado la primera medida de física usando datos reales en CMS: la medida de la razón de carga de muones procedentes de rayos cósmicos, en función del momento del muón (capítulo 2). Se trata del cociente del número de muones cósmicos con carga positiva entre el número de muones cósmicos con carga negativa, obtenido a partir de los datos recogidos en el *Magnet Test and Cosmic Challenge* (MTCC). El MTCC, primera prueba conjunta (en superficie) de casi todos los subsistemas de CMS, incluyendo el imán, se llevó cabo durante la segunda mitad de 2006 utilizando como haz de partículas los muones de alta energía procedentes de los rayos cósmicos. Aunque el MTCC se ha dedicado a pruebas del detector y los estudios de física no entraban dentro de sus prioridades, hemos sido capaces de obtener un resultado de gran calidad, consistente con las medidas previas realizadas por otros experimentos, dentro de las incertidumbres estadísticas:

$$\langle R^{\circ} \rangle = 1.266 \pm 0.008\,(\text{stat.}) \pm 0.026\,(\text{syst.})$$

Además del interés intrínseco de la medida, para la colaboración CMS ha supuesto una prueba

exitosa de la infraesctructura completa de análisis que se usará con los datos de las colisiones pp en LHC, así como una mejora en el entendimiento de los procedimientos de calibración y alineamiento del detector. Ha servido para desvelar y resolver problemas importantes relacionados tanto con las constantes de alineamiento del detector de muones como con el código de reconstrucción de CMS. Este análisis descrito en la primera parte de la tesis y documentado en una CMS NOTE [1].

La segunda parte de la memoria está dedicada al análisis de búsqueda del bosón de Higgs del Modelo Estándar en el canal de desintegración $\mathrm{H} \to \mathrm{ZZ}^{(*)} \to 4\mu$ (capítulo 3). Este proceso es particularmente interesante para el descubrimiento del bosón de Higgs, principalmente debido a que proporciona sucesos muy limpios, con cuatro muones aislados (dos positivos y dos negativos) y de alto momento transverso, a la vez que está afectado por una cantidad razonablemente pequeña de sucesos de contaminación de ZZ no resonante. La masa de los pares de muones es compatible con la del bosón Z, dependiendo de la restricción en el espacio de fases introducida por la propia masa del bosón de Higgs. La masa invariante de los cuatro muones es, dentro de la resolución del detector, la del bosón de Higgs. Es el canal de mayor sensibilidad, junto con los otros estados finales con cuatro leptones, dentro de un amplio rango de masas del bosón de Higgs. Esta región se extiende desde 130 GeV/c^2 a 500 GeV/c^2, exceptuando el rango de 160 GeV/c^2 $< m_{\mathrm{H}} <$ 180 GeV/c^2, donde domina el canal $\mathrm{H} \to \mathrm{W}^+\mathrm{W}^-$. Las muestras simuladas de señal del bosón de Higgs se seleccionan con alta eficiencia y pureza mediante un análisis basado en cortes y que no depende del valor que pueda tener la masa del bosón de Higgs. La significación estadística de la señal, determinada a partir de la distribución de masa invariante de cuatro muones mediante el método estadístico del *log-likelihood ratio*, está cerca de 5σ para una luminosidad integrada de 10 fb^{-1}, para masas en torno a 140 GeV/c^2 y entre 180 GeV/c^2 y 400 GeV/c^2. El método también permite elaborar una estrategia de búsqueda del bosón de Higgs que se seguirá con datos reales, basada en el uso de niveles de confianza que permiten caracterizar la compatibilidad de los datos con las distribuciones esperadas de señal más contaminación ó con la de contaminación sólo. He participado en la selección de las muestras simuladas que se usan en este análisis y aplicado el método del *log-likelihood ratio* para obtener la significación estadística esperada de la señal del bosón de Higgs. Este análisis está documentado en una CMS NOTE [2].

También he desarrollado y aplicado un procedimiento para medir la masa, la sección eficaz de producción y la anchura del bosón de Higgs usando este canal de desintegración, para masas del bosón de Higgs entre 130 GeV/c^2 y 600 GeV/c^2 (capítulo 4). Para ello, se realiza un ajuste de máxima verosimilitud a la distribución de masa invariante reconstruida de cuatro muones mediante una función que describe tanto la contribución de la señal como la de la contaminación. Dicha función tiene en cuenta, además, la resolución experimental y la cola radiativa debida a la emisión de radiación de *bremsstrahlung* interna en el estado final y depende de los parámetros que se estudian. Los valores verdaderos de los parámetros se recuperan con gran exactitud en todo el rango de masas para luminosidades integradas a partir de 30 fb^{-1}. Para ese valor de luminosidad integrada, la masa del bosón de Higgs se puede medir con precisiones entre el 0.1% y el 5.4%. La anchura intrínseca únicamente se puede medir si el bosón de Higgs tiene una masa superior a 190 GeV/c^2, con precisiones en torno al 35%. Para valores inferiores de m_{H} domina la resolución experimental. Por último, es posible determinar la sección eficaz de producción, para

masas en el rango 130 GeV/c^2 - 150 GeV/c^2 y por encima de 190 GeV/c^2, con precisiones en torno al 30%. Este procedimiento también está documentado en una CMS NOTE [3] y descrito en la memoria.

Estos dos análisis son mucho más realistas que los realizados anteriormente por varias razones. Respecto a las muestras de datos simulados, se han usado tanto la última versión del software oficial de simulación y reconstrucción de CMS disponible en el momento como los generadores de procesos más exactos disponibles para los procesos de señal y de contaminación. Respecto a los métodos de análisis, se utiliza un único conjunto de requisitos, independiente del valor de la masa del bosón de Higgs, para seleccionar de forma eficiente la señal de la contaminación. Estos cortes no están optimizados para ningún valor concreto de la masa del bosón de Higgs y no dependen críticamente de ninguna suposición sobre el comportamiento óptimo del detector, lo cual hace que el análisis sea menos sensible a efectos sistemáticos y a las características particulares de la simulación. Además, se han tenido en cuenta las incertidumbres sistemáticas, principalmente debidas a efectos experimentales e incertidumbres teóricas, en la normalización de la señal y de la contaminación esperadas. Por ello, estos dos análisis están publicados en el *Physics Technical Design Report, Vol. II* de CMS [4] y son los resultados oficiales del experimento CMS en relación con la búsqueda del bosón de Higgs en el canal $H \rightarrow ZZ^{(*)} \rightarrow 4\mu$.

Chapter 1

The Standard Model and the CMS experiment at LHC

This chapter gives a very brief overview of the Standard Model of particle physics, with the aim of introducing the open issues that LHC is expected to explore. Short descriptions of the LHC accelerator and the CMS experiment are also presented (for more details on the experimental setup, see [5–7]).

1.1 The Standard Model: Electroweak Symmetry Breaking

The Standard Model of elementary particles [8, 9] is a very successful description of the interactions[1] of the fundamental components of matter. It is a relativistic quantum field theory that describes the interactions of spin-$\frac{1}{2}$ fermions (matter), mediated by spin-1 gauge bosons (interactions). The existence of the gauge bosons and the form of their interactions are dictated by local gauge invariance, a manifestation of the symmetry group of the theory, $SU(3)_C \times SU(2)_L \times U(1)_Y$. It combines the electroweak theory proposed by Glashow, Salam and Weinberg [8] to describe the electromagnetic [10] and weak [11] interactions, based on the gauge symmetry group $SU(2)_L \times U(1)_Y$, with Quantum Chromodynamics [9], which is the theory of the strong interactions and is based on the symmetry group $SU(3)_C$. The theory is perturbative at sufficiently high energies [9] and renormalizable [12], and thus describes these interactions at the quantum level.

Fermions, fundamental constituents of matter lacking known internal structure to date, are classified in two groups: quarks and leptons. Quarks are triplets under the $SU(3)_C$ group, and therefore undergo strong interaction. Leptons, on the other hand, are singlets in $SU(3)_C$. The left-handed states of fermions are $SU(2)_L$ doublets, while their right-handed partners transform as $SU(2)_L$ singlets. Placing right-handed and left-handed fermions into different multiplets of the $SU(2)_L$ group describes parity violation within the framework of the theory. The Standard Model includes three generations or families of fermions, all of them identical except for the mass. Ordinary matter is composed by particles from the first generation. The other generations only

[1] except gravitation

appear in high-energy interactions (cosmic rays, accelerators...). The leptons are the electron (e^-), the muon (μ^-) and the tau (τ^-), each of which has electric charge $Q = -1$ (all charges are given in units of the elementary charge, e), and their corresponding neutrinos, ν_e, ν_μ and ν_τ, with $Q = 0$. The quarks are of six different flavours: u, d, c, s, t and b, and all have fractional charge $Q = \frac{2}{3}, -\frac{1}{3}, \frac{2}{3}, -\frac{1}{3}, \frac{2}{3}$ and $-\frac{1}{3}$, respectively. Experiments confirm that quarks do not freely exist in nature and are the constituents of a wide class of particles, the hadrons. The particle content in each family is:

$$\mathbf{1^{st}family}: \begin{pmatrix} \nu_e \\ e^- \end{pmatrix}_L,\ e_R^-,\ \begin{pmatrix} u \\ d \end{pmatrix}_L,\ u_R,\ d_R$$
$$\mathbf{2^{nd}family}: \begin{pmatrix} \nu_\mu \\ \mu^- \end{pmatrix}_L,\ \mu_R^-,\ \begin{pmatrix} c \\ s \end{pmatrix}_L,\ c_R,\ s_R$$
$$\mathbf{3^{rd}family}: \begin{pmatrix} \nu_\tau \\ \tau^- \end{pmatrix}_L,\ \tau_R^-,\ \begin{pmatrix} t \\ b \end{pmatrix}_L,\ t_R,\ b_R$$

and their corresponding antiparticles. The left-handed (L) and right-handed (R) fields are defined by means of the chirality operator γ_5 in the following way:

$$e_L^- = \frac{1}{2}(1-\gamma_5)e^-;\ e_R^- = \frac{1}{2}(1+\gamma_5)e^-$$

Every quark with a given flavour carries an additional *charge* referred to as colour, q_α, $\alpha = 1, 2, 3$. There is mixing between the three generations of quarks, which is parameterized in the Standard Model by the Cabibbo-Kobayashi-Maskawa (CKM) matrix [13]. However, the origin of this mixing remains unexplained.

In the Standard Model the strong interaction is described by the Quantum Chromodynamics (QCD), which is gauge invariant under $SU(3)_C$. The particles that mediate this interaction are eight vector bosons – gluons – which are massless, electrically neutral and carry colour charge. The consequence of the gluons carrying colour is that not only they interact with quarks, but also with themselves. Their interactions are such that they become stronger with distance. This makes the strong coupling constant (or equivalently, $\alpha_S = g_S^2/4\pi$) small at high transferred momenta but large at small momenta, leading to the confinement of quarks in hadrons, the colourless, experimentally-observed matter particles.

The $SU(2)_L \times U(1)_Y$ symmetry group describes the electroweak interactions of quarks and leptons. The particles that mediate this interaction are four gauge bosons: the three vector bosons $W^\pm$ and Z, mediators of the weak interactions, and the photon, γ, which is the particle exchanged in electromagnetic interactions. The weak bosons, $W^\pm$ and Z, are massive particles, couple only to left-handed doublets (weak interaction is chiral) and do interact between them. The $W^\pm$ have charge $Q = \pm 1$ respectively, and the Z is electrically neutral. The photon is massless, chargeless and does not interact with itself.

The main characteristics of strong, weak and electromagnetic interactions are summarized in Table 1.1.

The gauge symmetry of $SU(3)_C \times SU(2)_L \times U(1)_Y$ provides the bosons that serve as interaction mediators. Local gauge invariance makes the theory re-normalizable and requires the gauge

Interaction	**Electromagnetic**	**Weak**	**Strong**
Boson	Photon (γ)	$W^{\pm}, Z$	Gluons
Mass (GeV/c^2)	0	80.4, 91.2	0
Coupling Constant	$\alpha(Q = m_e) \approx \frac{1}{137}$	$G_F = 1.167 \times 10^{-5}\text{GeV}^{-2}$	$\alpha_S(m_Z) \approx 0.1$
Range (cm)	∞	10^{-16}	10^{-13}

Table 1.1: Fundamental interactions of the elementary particles.

bosons to be massless. However, $W^{\pm}$ and Z bosons have masses. The fact that the weak gauge bosons are massive particles indicates that $SU(2)_L \times U(1)_Y$ is not a symmetry of the vacuum. In contrast, the photon being massless reflects that $U(1)_{em}$ is a good symmetry of the vacuum. Thus, the Standard Model postulates the so-called Higgs mechanism [14], which spontaneously breaks the electroweak symmetry $SU(2)_L \times U(1)_Y$ to the electromagnetic $U(1)_{em}$ symmetry by introducing an $SU(2)$ doublet of complex scalar fields (Higgs field), Φ. The Lagrangian of this field must be invariant under $SU(2)_L \times U(1)_Y$ local gauge transformations, and takes the form:

$$\mathcal{L}_{Higgs} = (D_\mu \Phi)^\dagger (D^\mu \Phi) - V(\Phi) \tag{1.1}$$

The potential is:

$$V(\Phi) = -\mu^2 \Phi^\dagger \Phi + \lambda (\Phi^\dagger \Phi)^2, \tag{1.2}$$

with $\lambda > 0$.

The neutral component of the Higgs field develops a non-zero vacuum expectation value. As a consequence, the electroweak $SU(2)_L \times U(1)_Y$ symmetry is spontaneously broken to the electromagnetic $U(1)_{em}$ symmetry. Three of the four degrees of freedom of the doublet scalar field are absorbed by the $W^{\pm}$ and Z weak vector bosons to form their longitudinal polarizations and to acquire masses, that derive from the coupling of the boson fields with the non-zero vacuum value of the Higgs. However, this minimum is invariant under $U(1)_{em}$ transformations, which means that this symmetry is unbroken and the photon remains massless. The remaining degree of freedom corresponds to a scalar particle, the Higgs boson. This new particle must also be electrically neutral and massive. However, its mass – acquired through self-coupling in the Higgs potential $V(\Phi)$ – is not fixed in the theory and the Higgs boson has not been observed in experiments so far. This is the only particle predicted by the Standard Model that has not been confirmed experimentally yet.

The Higgs boson mass at tree-level is:

$$m_H^2 = 2\lambda v^2 \tag{1.3}$$

where $v \equiv \sqrt{\frac{\mu^2}{\lambda}}$ is the vacuum expectation value and is related to the boson masses and their gauge couplings to fermions (g, g') in the following way:

$$m_{W^\pm} = \frac{1}{2} g v; \quad m_Z = \frac{1}{2} v \sqrt{g^2 + g'^2} \tag{1.4}$$

The strength of the self-interaction of the Higgs boson, λ, can be expressed in terms of the Higgs and gauge boson masses and the gauge coupling as:

$$\lambda = \frac{1}{8} g^2 \frac{m_{\mathrm{H}}^2}{m_{\mathrm{W}^\pm}^2} \tag{1.5}$$

and is completely undetermined in the Standard Model. Therefore the Higgs boson mass is unknown.

The same mechanism is used to provide mass to the fermions, making them couple to the Higgs boson with different strength (Yukawa couplings) according to their mass. The value of each coupling constant, G_f, is directly related with the corresponding fermion mass, m_f:

$$m_f = G_f \frac{v}{\sqrt{2}} \tag{1.6}$$

The values of the Yukawa couplings are not fixed in the Standard Model either, and they are determined from the experimental measurements of the fermion masses.

Thus, the simplest version of the Standard Model contains 19 free parameters: 5 for the coupling constants (g_S, g, g', μ^2, λ), 9 masses (6 for the quarks and 3 for the leptons, assuming neutrinos are massless), the 4 independent elements of the CKM matrix that describes the quark flavour mixing, and 1 phase that accounts for a QCD interaction among gluons which can violate CP. The first five of these parameters correspond to the gauge and matter sectors and have been accurately determined in experiments [15]. The rest are related to the symmetry breaking sector, which remains without experimental verification.

1.1.1 Constraints to the Standard Model Higgs boson mass

Despite the lack of direct experimental evidence of the existence of the Higgs boson so far, the overwhelming efforts dedicated to its study, both from the theoretical and from the experimental points of view, have established strict limits to its possible properties. The experimental search for the Higgs boson represents a challenge because even if the way it couples to fermions and gauge bosons is now completely fixed by the experiments, there is no theoretical prediction for the value of its mass. The difficulty in the design of experiments to search for the Higgs boson lies precisely in the fact that they must be sensitive to all possible mass values.

Theoretical constraints

From the theoretical point of view, there are consistency arguments of the Standard Model that impose severe constraints on the Higgs boson mass [16]. First of all, the Higgs potential described in Eq. 1.2 is affected by radiative corrections which involve the mass of fermions and bosons and depend on the renormalization scale. These radiative corrections may modify the shape of the potential in a way such that an absolute minimum no longer exists and no stable spontaneous symmetry breaking occurs. The requirement of *vacuum stability*, that is, that the λ coefficient is large enough to avoid instability up to a certain scale Λ, implies a lower bound on m_{H}.

On the other hand, the Higgs boson mass is required to be large enough to cancel the divergences arising from the scattering of longitudinally-polarized W bosons in the high energy limit [17]. However, according to Eq. 1.5, if $m_{\mathrm{H}} \gg m_{\mathrm{W}}$, the scalar self interaction becomes strong, and violates unitarity. Therefore, the Higgs boson mass should be less than about 850 GeV/c^2. Also, the dependency of the coupling with the energy scale results in an increase of λ with the energy scale. The requirement that λ remains non-zero and finite up to a scale Λ (*triviality*) corresponds to an upper bound on m_{H}.

The parameter Λ represents the energy scale beyond which the Standard Model is no longer valid and new physics is expected to appear. For low energy scales ($\Lambda \sim 10^3$ GeV), the allowed Higgs boson mass is lower than 1 TeV/c^2, while for larger Λ values (up to the Planck scale, $\Lambda \approx 10^{19}$ GeV), the upper bound on m_{H} descends to around 160 GeV/c^2 to 200 GeV/c^2. The theoretical bounds on m_{H} as a function of Λ are shown in Figure 1.1 [16] (left).

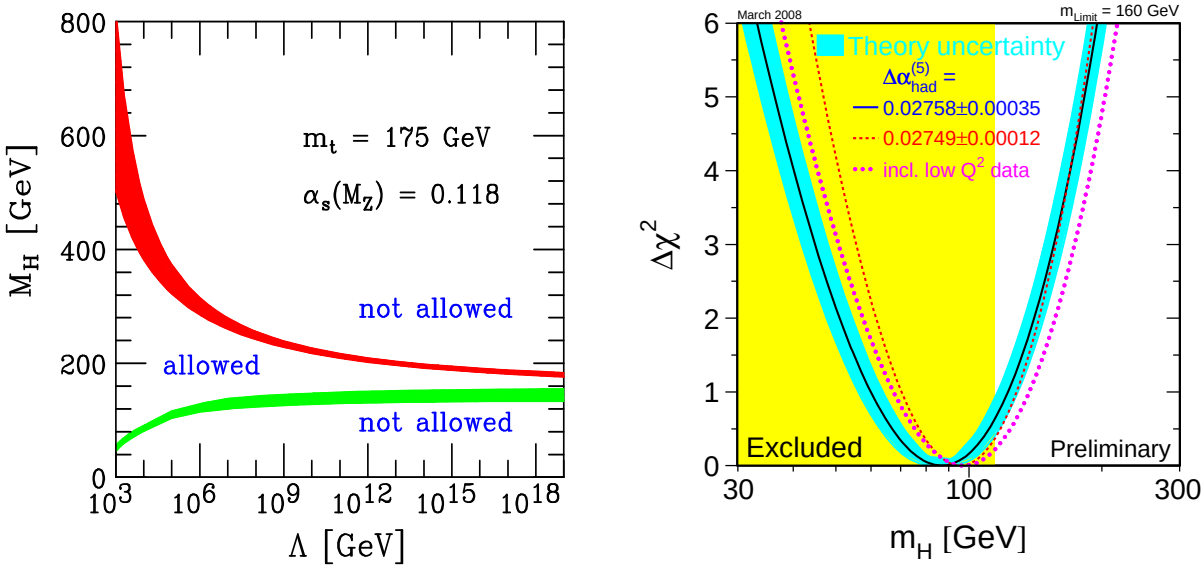

Figure 1.1: (Left) Theoretical bounds on the Higgs boson mass as a function of the cut-off energy scale Λ, up to which the Standard Model is assumed to remain valid. The upper solid area indicates the triviality upper bound. The width of the area indicates the sum of the theoretical uncertainties in m_{H}. The lower solid area represents the lower bounds derived from stability requirements using $m_{\mathrm{t}} = 175$ GeV/c^2 and $\alpha_S(m_{\mathrm{Z}}) = 0.118$. (Right) $\Delta\chi^2$ curve derived from high-Q^2 precision electroweak measurements, performed at LEP and by SLD, CDF and D0, as a function of the Higgs boson mass. The minimum of the curve is below the excluded value by direct searches (light shaded area).

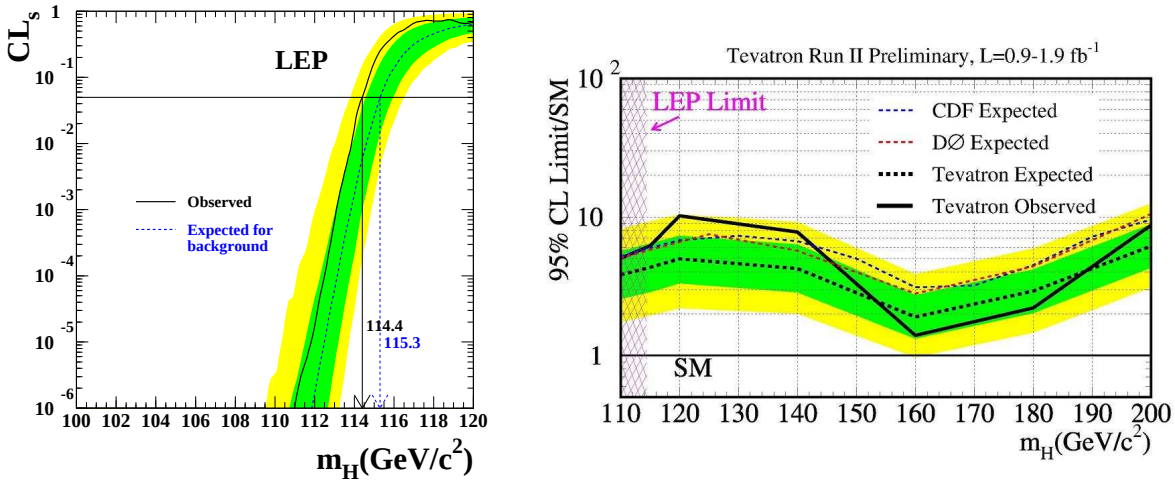

Figure 1.2: (Left) Confidence level CL_s for the *signal plus background* hypothesis, as a function of the Higgs boson test mass, at LEP. The intersection of the horizontal line at $CL_s = 0.05$ with the observed curve defines the 95% C.L. lower bound on the mass of the Standard Model Higgs boson. (Right) Observed and expected (median, for the *background-only* hypothesis) 95% C.L. upper limits on the ratios to the Standard Model cross section, as functions of the Higgs boson test mass, for the combined CDF and D0 experiments. Results are also shown for CDF and D0 separately. In both plots, the bands indicate the 68% and 95% probability regions in which the limits can fluctuate, in the absence of signal

Experimental constraints

Experimental bounds on the Higgs boson mass are provided by measurements at different experiments. The most sensitive direct search has been carried out at the LEP accelerator at CERN. No evidence for a signal was observed in data from e^+e^- collisions up to center-of-mass energies of 209 GeV (Figure 1.2, left [18]). An experimental lower bound is set to $m_H > 114.4$ GeV/c^2 at the 95% confidence level (C.L.) [18]. The search for the Standard Model Higgs particle still continues at Tevatron. Figure 1.2 (right) [19] shows the most recent update for the joint CDF/D0 sensitivity curves, together with the Standard Model prediction. The Tevatron experiments are close to the Standard Model predictions, nearly by a factor of 2 for some Higgs boson masses.

An indirect measurement of m_H within the Standard Model framework is possible using the precision measurements of the fundamental parameters, e.g., m_Z, Γ_Z, $m_{W^\pm}$. Such measurements have been performed by several experiments and a global fit to these electroweak observables with the Higgs boson mass as a free parameter sets limits on m_H [18,20]. Figure 1.1 [20] (right) shows the $\Delta\chi^2$ curve, derived from high-Q^2 electroweak precision measurements, performed at LEP and by SLD, CDF, and D0, as a function of the Standard Model Higgs boson mass. The preferred value for its mass, corresponding to the minimum of the curve, is at 87 GeV/c^2, with an experimental uncertainty of +36 and -27 GeV/c^2 (at 68% C.L. derived from $\Delta\chi^2 = 1$ for

the black line, thus not taking into account the theoretical uncertainty shown as the blue band nor the excluded values by direct search). This is not a proof that the Standard Model Higgs boson actually exists. However, it does serve as a guideline in what mass range to look for it. The electroweak precision measurements indicate that the mass of the Higgs boson is lower than about 160 GeV/c^2 (one-sided 95% C.L. upper limit derived from $\Delta\chi^2 = 2.7$ for the blue band, thus including both the experimental and the theoretical uncertainty). This limit increases to 190 GeV/c^2 when including the LEP2 direct search limit of 114 GeV/c^2 shown in yellow.

1.1.2 Open questions in the Standard Model

Despite the experimental success of the Standard Model, there are strong conceptual indications that this model does not describe nature completely, but it is a low-energy effective theory of a more fundamental, self-contained theory. As it has already been pointed out, there are at least nineteen absolutely arbitrary parameters in the Standard Model and many more parameters are needed to accommodate non-accelerator observations. For example, neutrino masses and mixing require at least seven additional parameters: three masses, three mixing angles and one CP-violating phase. Cosmological inflation implies at least one new mass scale of order 10^{16} GeV, the cosmological baryon asymmetry and the description of the non-baryonic dark matter requires a still non-determined number of additional parameters, and the cosmological constant may be non-zero. In a fundamental physical model all these parameters should not appear as totally free.

In fact, during the last ten years experimental evidence appeared that demonstrated that the Standard Model is incomplete: non-baryonic dark matter [21]; dark energy [22–24]; neutrino mass [25]; nearly scale-invariant, Gaussian, and apparently acausal density perturbations [23]; baryon asymmetry [26]. Moreover, the confirmed existence of non-baryonic dark matter requires new particles that are not present in the Standard Model.

From a more theoretical point of view, we already observed that theoretical bounds on the Higgs mass can be derived from the request that, once radiative corrections are included, the theory remains valid up to a given energy scale. It is natural to think that at higher energy scales some more general theory should be valid, possibly describing all interactions. In the Standard Model, the strong interaction is described by the $SU(3)_C$ symmetry group, which however is not unified with the electroweak description. Another shortcoming of the Standard Model comes from its inability to include gravity, whose strength should become comparable with that of other interactions at the Planck scale (10^{19} GeV).

In addition, the Higgs mass suffers from divergences caused by radiative corrections which are proportional to the energy cutoff; for the Standard Model to be valid up to very high energy scales, extremely precise cancellations should be present at all perturbation levels. Such cancellations are formally possible, but there is no reason why such a fine tuning should occur (*naturalness problem*).

Also, there is no explanation both for the origin of the three-family structure and the breaking of the generational symmetry (flavour symmetry) and for the fact that the particle masses would be significantly smaller than the energy scale up to which the theory remains valid (*hierarchy problem*).

Several solutions for these problems have been proposed. Some of the (known) extensions of

the Standard Model are supersymmetry (new fermion-boson symmetry) or extra dimensions (dimensions of invisible size up to now), both motivated by the superstring theories, *little higgs*-type models (new boson-boson and fermion-fermion symmetry) or the existence of new fundamental interactions at energy scales not yet explored. The most intriguing feature of all these theoretical models is that they predict the existence of new physics phenomena not considered by the Standard Model at the TeV energy scale.

1.2 LHC and the CMS experiment

Given the experimental situation of the Standard Model 25 years ago, it became necessary to build a new accelerator capable of reaching higher energies than those achieved up to date, in order to produce and study the Higgs boson and any other new physics phenomena. This accelerator is the Large Hadron Collider at the European Laboratory for Nuclear Research (CERN) [27]. It will be the first accelerator to provide parton-parton collisions up to energies of about 1 TeV, the energy scale relevant to electroweak symmetry breaking and at which beyond the Standard Model phenomena are expected to appear.

1.2.1 The Large Hadron Collider

The *Large Hadron Collider* (LHC) [5] is a proton-proton collider that is being installed in the 26.6 km circumference tunnel formerly used by the LEP electron-positron collider at CERN (Figure 1.3 [5]), at a depth ranging from 50 to 175 m underground. The center-of-mass collision energy is $\sqrt{s} = 14$ TeV and the design luminosity is 2×10^{34} cm^{-2} s^{-1}. The luminosity is the number of collisions per unit-time and cross-sectional area of the beams, $L = f\frac{n_1 n_2}{A}$, where f is the collision frequency of bunches composed by n_1 and n_2 particles and A is the overlapping cross-sectional area of the beams. It is specific to the collider parameters and does not depend on the considered interaction. It is expressed in cm^{-2} s^{-1}. Normally, the *integrated luminosity*, $\mathcal{L} = \int L\,dt$, expressed in fb^{-1} or pb^{-1}, is used.

LHC is composed by a set of two synchroton rings along which two independent proton beams will circulate in opposite directions. It will also operate at certain stages as a heavy ion (Pb, for example) collider in order to study the quark-gluon plasma and the QCD phase diagram. LHC will use SPS, PS and all the pre-accelerators that already exist at CERN as injectors. The beams intersect at four points where experiments are placed. Two of these are high luminosity regions and house the ATLAS [28] and CMS [29] detectors, general-purpose experiments with similar physics goals that are located in opposite positions along the ring. The other two detectors are devoted to specific research topics: LHC-b [30] is optimized to study b-quark physics and CP-symmetry violation in particular, and ALICE [31] is to be used for the study of heavy ion collisions. These detectors will be placed at the insertion points from SPS. Protons coming from SPS will enter the LHC rings with an energy of 0.45 TeV and will be accelerated using superconducting cavities until they reach 7 TeV per beam. Both beams share the superconducting magnets responsible for their orientation and focusing. The most relevant parameters of LHC are summarized in Table 1.2.

Currenlty, LHC is in the final stages of construction and commissioning (Figure 1.3, upper), with some sections already being cooled down to their final operating temperature of ~ 2 K,

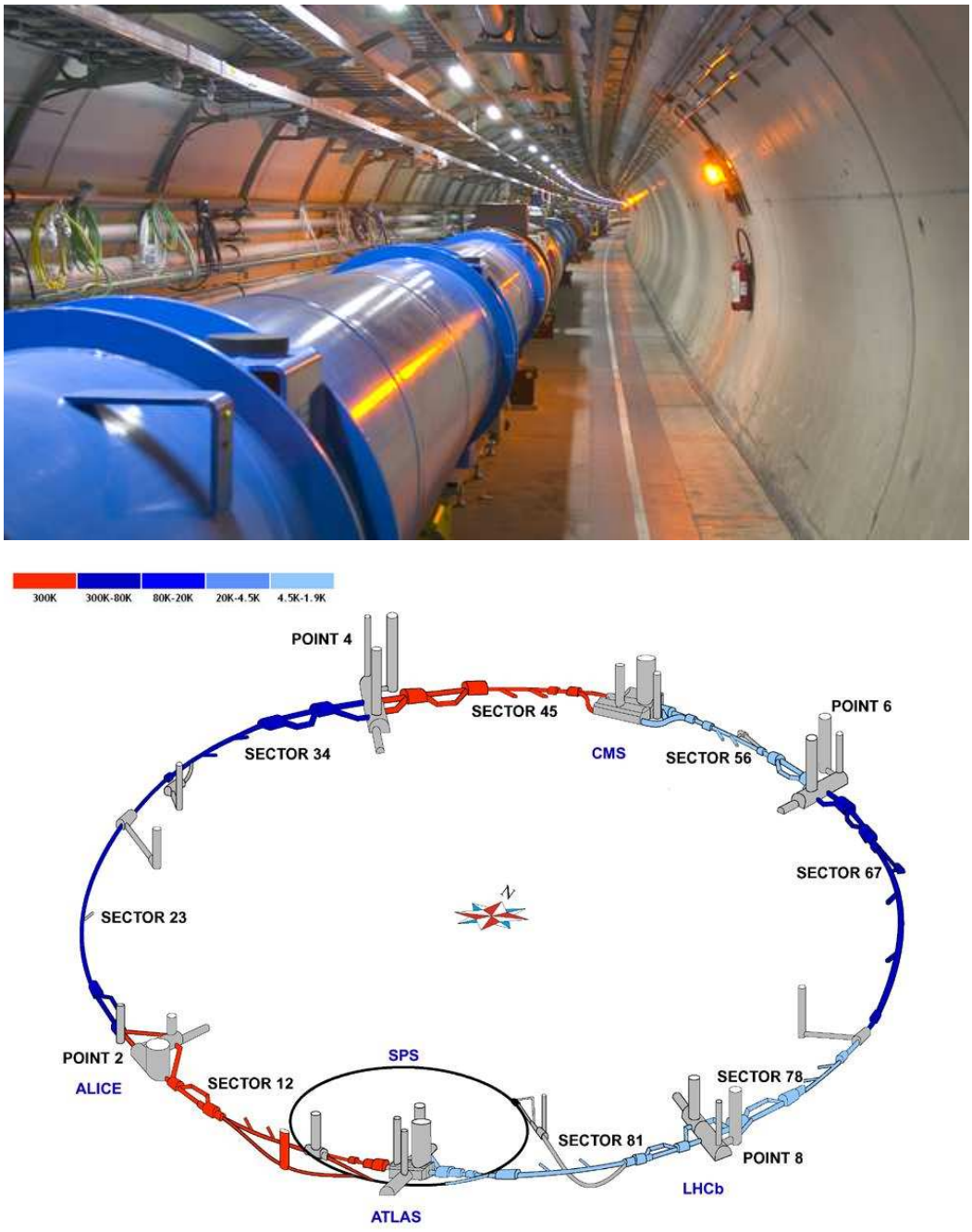

Figure 1.3: (Upper) View of the LHC accelerator. (Lower) Overview of LHC and location of the different experiments. The current status of the cooling of the LHC sections is shown in blue colour, where light blue corresponds to the sectors that have reached the final operating temperature of ~ 2 K. The cooling process will be completed by the end of June 2008.

shown in light blue in Figure 1.3 (lower). The first beams will be due for injection soon after the cooling down is completed (planned for end of June 2008) and the first collisions will follow two months later [32]. It will undergo a series of accelerator/detector commissioning stages at the beginning of its operation. Physics runs are planned to start with "low luminosity" runs of up to 2×10^{33} cm^{-2} s^{-1} for a few years before upgrading to the design "high luminosity" regime of 2×10^{34} cm^{-2} s^{-1}. The initial collision energy will be 10 TeV (instead of 14 TeV) due to technical problems with few superconducting magnets.

Parameter	Nominal value
Center-of-mass energy	14 TeV
Injection energy in LHC	450 GeV
Number of particles per bunch	1.15×10^{11}
Number of bunches per ring	2808
Design luminosity	10^{34}cm^{-2} s^{-1} = 10 nb^{-1} s^{-1}
Luminosity lifetime	10 h
Time between collisions	24.95 ns
Bunch crossing rate	40.08 MHz
Interaction rate	1 GHz
Bunch length	53 mm
Beam radius at interaction point	16 μm
Circumference	26.659 km
Dipole Field	8.3 T
Magnet temperature	$\leq$ 2 K

Table 1.2: Design LHC parameters for proton-proton collisions

The cross-section and event production rates for different processes as a function of the center-of-mass energies in proton-proton collisions is depicted in Figure 1.4 [33]. It can be seen that the Higgs boson production cross-section increases steeply with the center-of-mass energy, while the total cross-section (that is, the background cross-section), remains almost constant. In order to observe processes with extremely low cross-section ($\sim 10^{-9} - 10^{-11}$ with respect to background), the LHC must have an enormously high luminosity. Luminosities of up to 10^{34} cm^{-2} s^{-1} are expected to be achieved by means of collisions of approximately 2800 bunches of 10^{11} protons per bunch every 25 ns. The interaction rate at these luminosities will be 10^9 Hz. This has the drawback that the proton density per bunch will be such that several interactions will overlap in the same bunch crossing (pile-up). This difficult environment forces LHC detectors to have a data discrimination system (trigger) capable of managing the information collected in several collisions every 25 ns and able to perform a strong data reduction, eliminating all the non-interesting collisions online. After the online preselection system, the rate of accepted events will be reduced to about 150 Hz. The registered information of each event is 1.5 MB, approximately. Taking into account that the accelerator will operate around 10^7 seconds per year, the total storaging needs are about 2×10^6 Gigabytes per year to save all the information coming from the detector. Several tens of thousands of current PCs will be needed to reconstruct,

simulate and analyze such enormous amount of data. For this purpose, a whole infrastructure called Grid [34] is being developed, which will allow confronting this unprecedented challenge and represents a technological challenge by itself.

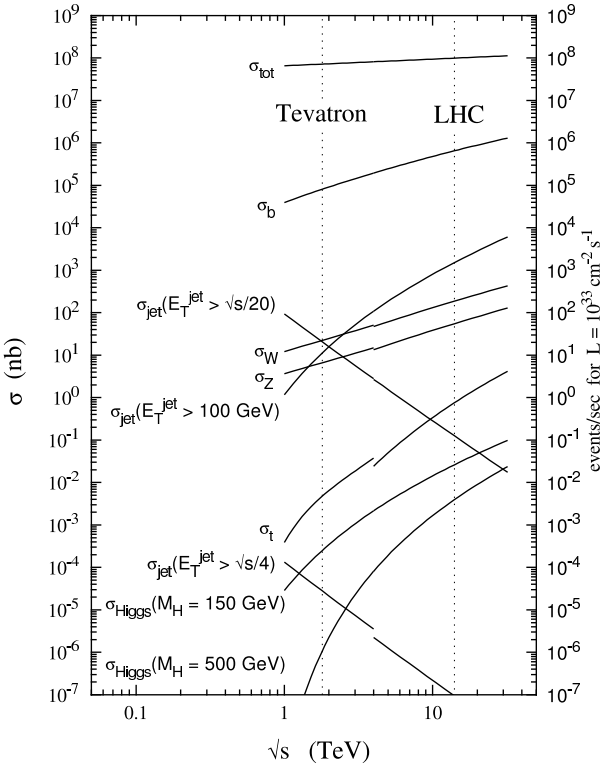

Figure 1.4: Cross-section and event production rates for different processes as a function of the center-of-mass energies in proton-proton and proton-antiproton collisions.

1.2.2 The CMS experiment

The total proton-proton cross-section $\sqrt{s} = 14$ TeV is roughly 100 mb. At design luminosity, CMS will observe an event rate of approximately 10^9 inelastic events per second. This leads to a number of experimental challenges. The online event selection process (trigger) must reduce the approximately 1 billion interactions per second to no more than about 100 events per second for storage and subsequent analysis. The short time between bunch crossings, 25 ns, has major implications for the design of the readout and trigger systems.

At high luminosity, a mean of about 20 inelastic (hard scattering) collisions will be superimposed on the event of interest. This implies that around 1000 charged particles will emerge from the interaction region every 25 ns. The products of an interaction under study may be confused with those from other interactions in the same bunch crossing. This problem becomes more severe when the response time of a detector element and its electronic signal is longer than 25

ns. The effect of the pile-up can be reduced using high-granularity detectors with good time resolution, resulting in low occupancy. This requires a large number of detector electronic channels (several millions), making necessary very good synchronization. Finally, the large flux of particles coming from the interaction region leads to high radiation levels, requiring radiation-hard detectors and front-end electronics.

In addition to these technical conditions, the CMS detector must fulfill strong requirements [6, 7, 35] from the scientific point of view, in order to meet the goals of the LHC physics programme that can be summarized as follows:

- Good muon identification and momentum resolution over a wide range of momenta and angles, good dimuon mass resolution ($\approx 1\%$ at 100 GeV/c^2), and the ability to determine unambiguously the charge of muons with p < 1 TeV/c.
- Good charged particle momentum resolution and reconstruction efficiency in the inner tracker. Efficient triggering and offline tagging of τ's and b-jets, requiring pixel detectors close to the interaction region.
- Good electromagnetic energy resolution, good diphoton and dielectron mass resolution ($\approx$ 1% at 100 GeV/c^2), wide geometric coverage, correct localization of the primary interaction vertex, π^0 rejection and efficient photon and lepton isolation at high luminosities.
- Good missing-transverse-energy and dijet-mass resolution, requiring hadron calorimeters with a large hermetic geometric coverage and with fine lateral segmentation.

The chosen design of CMS to meet all these conditions is briefly discussed below, and is driven by the election of a strong solenoid magnetic field to achieve a precise measurement of the momentum of charged particles and a very good identification of muons. A detailed description can be found in [6, 7, 35].

Overall design

The CMS (*Compact Muon Solenoid*) experiment [36] is formed by an international collaboration composed by more than 2880 scientists from over 184 different institutions from around 35 countries. It is one of the two general-purpose detectors that will operate in LHC. The main distinguishing features of CMS are: a very precise and redundant muon spectrometer; a fully active scintillating crystal-based electromagnetic calorimeter consistent with the muon spectrometer; a full silicon-based inner tracking system, compatible with both the electromagnetic calorimeter and the muon system; a sampling and hermetic hadronic calorimeter. The design of CMS is driven by the choice of the magnetic field configuration for the measurement of the momentum of muons. Its compact design is achieved by means of a very intense magnetic field, which is generated by a 4 Tesla superconducting solenoid and is kept uniform by a massive iron return yoke. This solenoid is large enough to accommodate the inner tracker and the calorimeters, allowing precision measurements of electrons and photons. The 4 T magnetic field provides the large bending power needed to measure precisely the momentum of charged particles and reduces the pile-up from soft hadrons in the muon system, which is installed in the return yoke.

The detector is composed of a cylindrical barrel closed by two end-cap discs, with a total length of 21.6 m, a diameter of 14.6 m and a total weight of around 12500 tons. It comprises several detection subsystems, each of which is specialized in the detection of certain types of particles. The overall layout of CMS is shown in Figure 1.5 (upper).

The coordinate system adopted by CMS is a right-handed system, with the origin centered at the nominal collision point inside the experiment, the y-axis pointing vertically upward, the x-axis pointing radially inward towards the center of the LHC and the z-axis pointing along the beam direction. The azimuthal angle, ϕ, is measured from the x-axis in the x-y plane, and the polar angle, θ, is measured from the z-axis. The *pseudorapidity* is normally used instead of the θ angle and is defined as $\eta \equiv -\ln\left(\tan\frac{\theta}{2}\right)$. Thus, the momentum and energy measured transverse to the beam direction, denoted by p_{T} and $\mathrm{E_T}$, respectively, are computed from the x and y components. The detector presents cylindric symmetry in the low pseudorapidity region (barrel) and is arranged in discs in the end-caps, which correspond to the high $|\eta|$ regions. The beam pipe is set along the central axis of the cylinder. The collision of the two beams takes place at the center of the cylinder.

In a radial path outwards the detector, from the interaction point to the outermost layers, the following subsystems are found (picture on page 18):

The Inner Tracking System. The inner tracker [37] (picture on page 19) is devoted to measure the trajectories of the charged particles emerging from the LHC collisions as well as precise reconstruction of secondary vertices. It surrounds the interaction point and has a length of 5.8 m and a diameter of 2.5 m. The CMS solenoid provides a homogeneous magnetic field of 4 Tesla over the full volume of the tracker. At the LHC design luminosity of 10^{34} $\mathrm{cm^{-2}\,s^{-1}}$ there will be on average about 1000 particles from more than 20 overlapping proton-proton interactions traversing the tracker for each bunch crossing, i.e. every 25 ns. Therefore, a detector technology featuring high granularity and read-out speed is required, such that the trajectories can be identified reliably and attributed to the correct bunch crossing. The large particle flux also imposes special requirements on radiation hardness. All these requirements on granularity, speed and radiation hardness lead to a tracker design entirely based on silicon detector technology. The CMS tracker is composed of a pixel detector with three barrel layers at radii between 4.4 cm and 10.2 cm and a silicon strip tracker with 10 barrel detection layers extending outwards to a radius of 1.1 m. Each system is completed by end-caps which consist of 2 disks in the pixel detector and 3 plus 9 disks in the strip tracker on each side of the barrel, extending the acceptance of the tracker up to a pseudorapidity of $|\eta| < 2.5$. With about 200 $\mathrm{m^2}$ of active silicon area, the CMS tracker is the largest silicon tracker ever built.

For isolated leptons of up to 100 GeV the expected transverse momentum resolution is $\Delta p_{\mathrm{T}}/p_{\mathrm{T}} < 10\%$ and a track reconstruction efficiency higher than 95% is expected in the $|\eta| < 2.5$ range.

The Electromagnetic Calorimeter. The goal of the electromagnetic calorimeter of CMS (ECAL) [38] (picture on page 20) is to accurately measure the energy and position of electrons and photons, help in the identification of electrons and charged pions and contribute to the

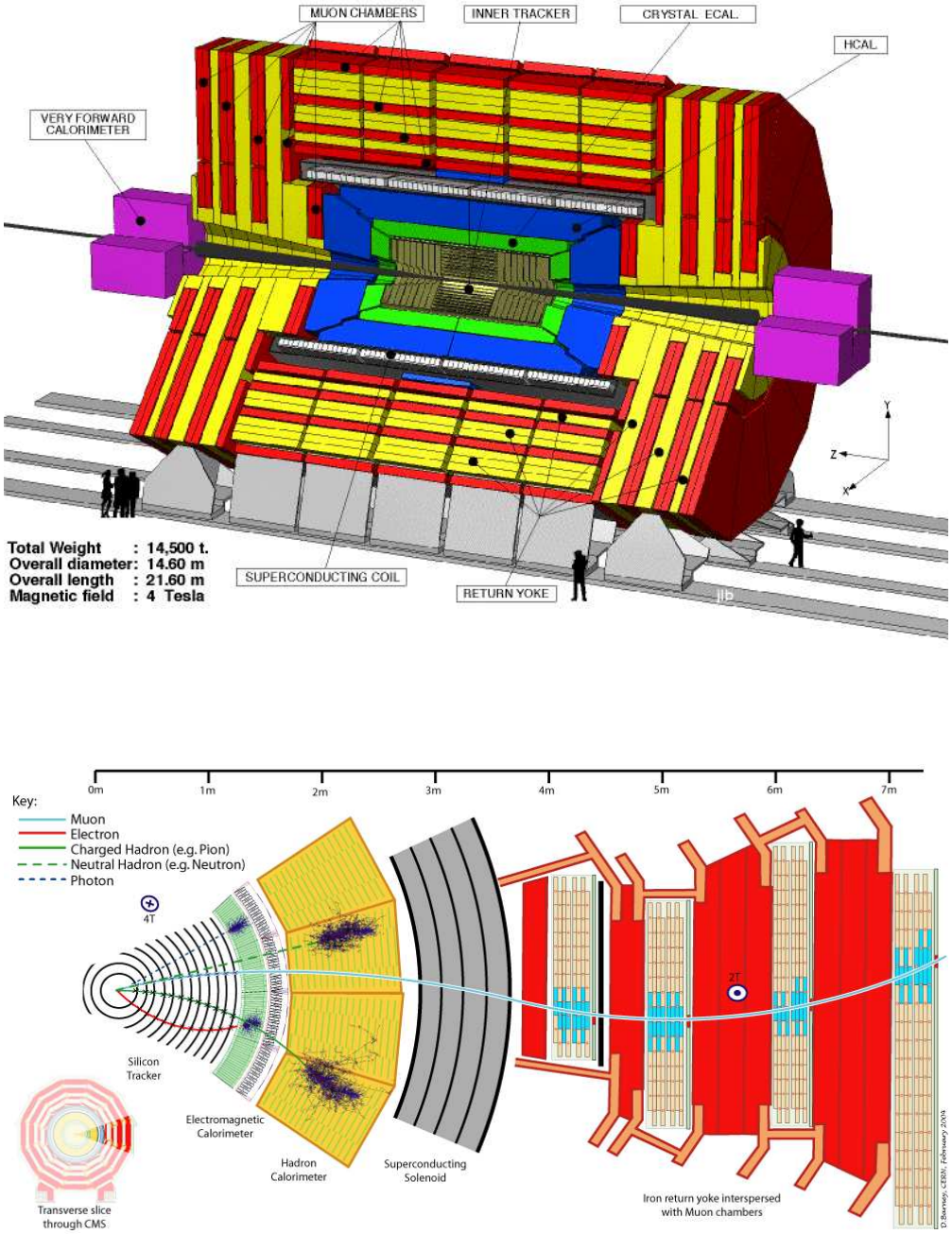

Figure 1.5: (Upper) An exploded view of the CMS detector. (Lower) Example of particle tracks, in a sector of the CMS detector, leaving signal in the different subsystems.

measurement of the energy of hadronic cascades. It comprises around 80000 finely segmented lead tungstate ($PbWO_4$) crystals with coverage in pseudorapidity up to $|\eta| < 3.0$. The crystals have different dimensions depending on their location in either the central barrel part or the two end-caps. Lead tungstate is a fast, radiation-hard scintillator characterized by a small Molière radius (21.9 mm) and a short radiation length (8.9 mm), that allows good shower containment in the limited space available for the ECAL. One of the driving criteria in the design was the capability to detect the Higgs boson decay to two photons. This capability is enhanced by the good energy resolution provided by a homogeneous crystal calorimeter.

The energy resolution of the ECAL for electromagnetic particles is better than 1 % for energies above 30 GeV and always better than 10 %.

A lead/silicon preshower detector is placed in front of the end-caps crystals. The principal aim of the CMS Preshower detector is to identify π^0's in the end-caps within a fiducial region $1.653 < |\eta| < 2.6$. It also helps the identification of electrons against minimum ionizing particles, and improves the position determination of electrons and photons with high granularity.

The Hadron Calorimeter. The ECAL is completely surrounded by a sampling hadron calorimeter (HCAL) [39] (picture on page 21) with coverage up to $|\eta| < 3.0$. The goal of the HCAL is the measurement of the direction and energy of hadron jets High hermeticity is required to be sensitive to the detection of missing transverse energy due to neutrinos or exotic particles. For this reason, the central barrel and end-cap HCAL sub-detectors (HB and HE, respectively), fully immersed within the high magnetic field of the solenoid, are complemented by very forward calorimeters (HF) which are located outside the muon system to complete the coverage up to $|\eta| < 5.2$. The HB and HE are brass/scintillator calorimeters. In the barrel, full shower containment is not possible within the magnet volume and an additional array of scintillators is placed outside the magnet (HO). The HF are iron/quartz-fibre calorimeters which are located outside the muon system at 11.2 m from the interaction point.

The performance of the HCAL is given in terms of jet energy resolution and missing transverse energy resolution. The jet energy depends on effects like the jet-finding algorithm, the fragmentation process or the pile-up, therefore the granularity of the sampling in the 3 main parts of the HCAL (HB, HE and HF) has been chosen such that the jet energy resolution, as a function of E_T, is similar in all 3 parts. The resolution of the missing transverse energy in QCD dijet events with pile-up in given by $\sigma(E_T^{miss}) \approx 1.0\sqrt{\Sigma E_T}$ if energy clustering corrections are not made, while the average E_T^{miss} is given by $\langle E_T^{miss} \rangle \approx 1.25\sqrt{\Sigma E_T}$.

The Superconducting Magnet. Both the tracker and the calorimeters are installed inside a 13-m-long, 6-m-inner-diameter superconducting solenoid [40]. Cooled with liquid helium, it is capable of generating an axial and uniform magnetic field of 4 T in the central region of the CMS detector. The goal of this strong magnetic field is to induce enough bending of the charged particle trajectories so that the momentum of the particles can be measured up to the highest momentum expected at LHC. In order to determine without ambiguities the sign for muons of ≈ 1 TeV/c, a momentum resolution of $\Delta p_T/p_T \approx 10\%$ is required. This resolution scales with 1/B, where B is the strength of the magnetic field. The flux is returned through a 10000 ton iron yoke comprising 5 wheels and 2 end-caps composed of three disks each.

The Muon System. The muon system [41] is CMS's most external sub-detector and it is interleaved with the iron wheels that serve as the return yoke of the magnet. Its goal is to identify muons and to provide, together with the inner tracker, an accurate measurement of their transverse momenta. This is crucial for CMS due to the fact that high-p_{T} muons provide very clean and clear signals for a wide variety of physics processes. For this reason, the muon spectrometer plays a very important role in the trigger. The thickness of the iron and the chain of sub-detectors that particles have to traverse before reaching the muon detectors ensure good muon identification, both in the barrel and in the end-caps regions.

The muon system is composed by three independent subsystems.

In the barrel, where the track occupancy and the residual magnetic field are low, Drift Tube (DT) chambers are installed (picture on page 22). The chamber segmentation follows that of the iron plates of the yoke, consisting in 5 wheels along the z-axis – named YB-2, ..., YB+2 – each one divided into 12 sectors. Chambers are organized into 4 stations – named MB1, ..., MB4 – forming concentric cylinders around the beam line: the first three of them consist of 60 drift chambers each, the fourth, of 70. The first 3 stations each contain 12 DT layers, providing 8 measurements of the muon track in the r-ϕ bending plane and 4 measurements in the z direction. The fourth station does not contain z-measuring planes. Within a single station, spatial resolutions of 100 μm in the r-ϕ plane and 150 μm in the r-θ plane are achieved.

In the two end-caps, Cathode Strip Chambers (CSC) are used, since in these regions the muon rates and background levels are high and the residual magnetic field between the plates of the yoke is large (up to 3.5 T) and non-uniform (picture on page 23). They are multi-wire proportional chambers with fast response time, fine segmentation, and radiation resistance. The CSCs are arranged in four disks (*stations*) perpendicular to the beam line and placed between the iron disks of the yoke. They are labelled ME1, ..., ME4. The cathode strips of each chamber run radially outward and provide a precision measurement in the r-ϕ bending plane. The anode wires run approximately perpendicular to the strips and are also read out in order to provide measurements of η and the beam-crossing time of a muon. Each 6-layer CSC provides robust pattern recognition for rejection of non-muon backgrounds and efficient matching of hits to those in other stations and to the CMS inner tracker. A final spatial resolution within a single station for CSCs of 80-150 μm, depending on the station, is achieved.

The DT and CSC systems cover the pseudorapidity region $|\eta| < 2.4$ and provide efficient muon track reconstruction and precise momentum measurement using the bending radius induced by the magnetic field.

Redundancy is obtained with a system of Resistive Plate Chambers (RPC), gaseous parallel-plate detectors that are installed both in the barrel and in the end-caps and cover the region $|\eta| < 1.2$. The RPCs have acceptable spatial resolution but very fast response and excellent time resolution, of the order of a few nanoseconds, providing unambiguous bunch crossing identification. Therefore, they are dedicated for the triggers and are also used to complement DTs and CSCs in the measurement of p_{T}. A total of 6 layers of RPC chambers are embedded in the barrel iron yoke, two located in each of the first and second muon stations and one in each of the two last stations. In the end-caps 4 layers are present.

The layer structure of the CMS detector described in this Section allows performing a clear and efficient identification of the particles emerging from the beam collision. Every type of particle leaves a distinct signal in the different detectors, as is shown in Figure 1.5 (lower):

- Photons: neutral electromagnetic particles. They deposit their energy in the ECAL and do not leave track in the tracker.
- Electrons: charged electromagnetic particles. They leave their energy in the ECAL and a track in the tracker.
- Hadrons: they deposit their energy in the HCAL (in different ways, depending on the type of hadron). Many of them have minimum interaction in the ECAL, although a fraction of them has strong interaction and initiates the hadronic cascade in that calorimeter. Charged hadrons leave track in the tracker, while neutral hadrons do not.
- Muons: these are the only particles that leave a track in the muon detectors. They are minimum ionizing particles in the calorimeters and leave track in the tracker.

1.3 Conclusions

My research work has addressed two of the main issues depicted in this Chapter, which are particularly relevant in the last few years of the construction phase of the experiment: first, demonstrating the capabilities of the CMS detector (an existing fraction of it) to perform a measurement using real data from cosmic muons (Chapter 2), and, second, establishing the CMS discovery potential for a Standard Model Higgs boson using the state-of-the-art software and analysis tools (Chapters 3 and 4).

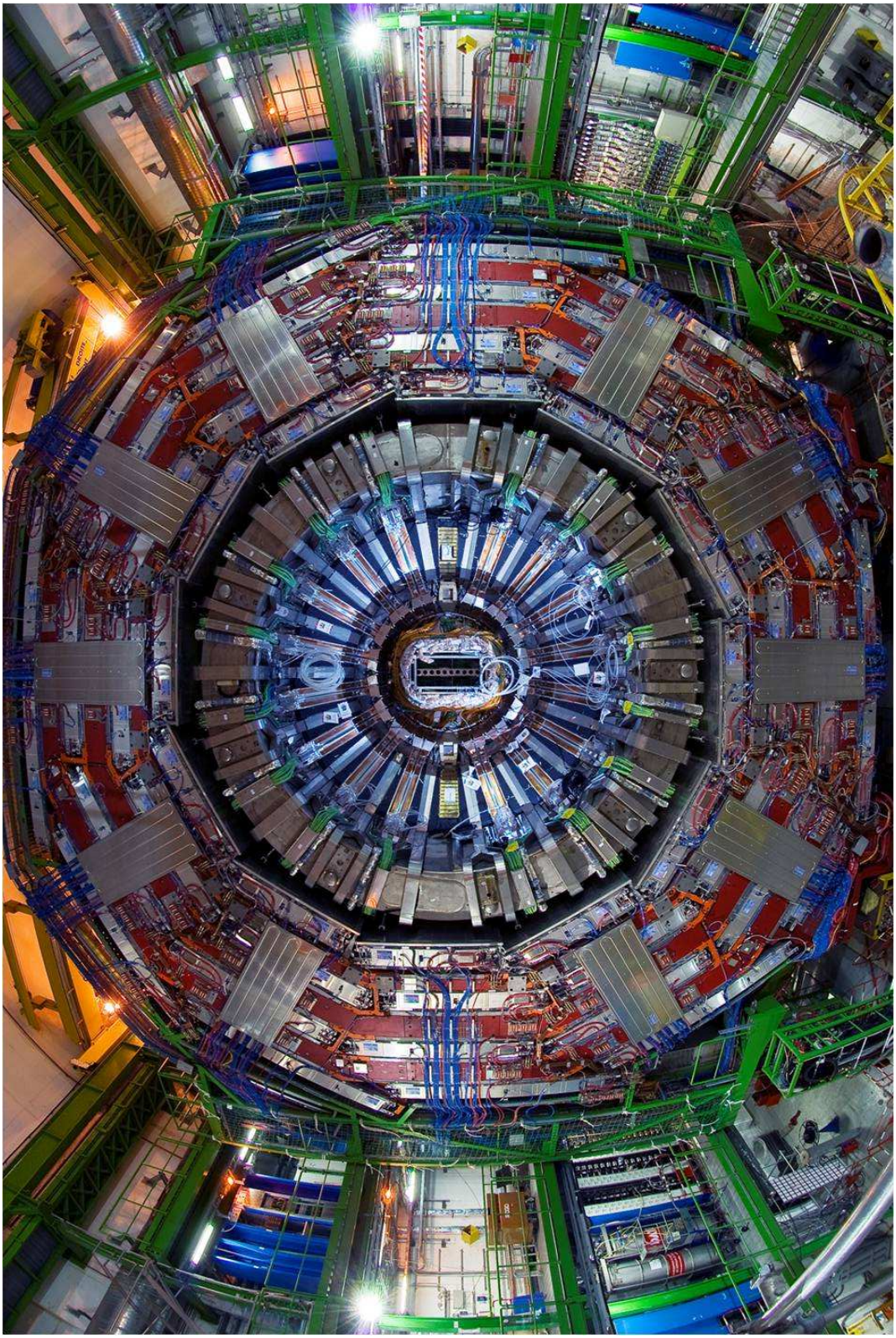

View of one wheel of the CMS detector showing the tracker, ECAL, HCAL, magnet and the muon barrel drift tubes.

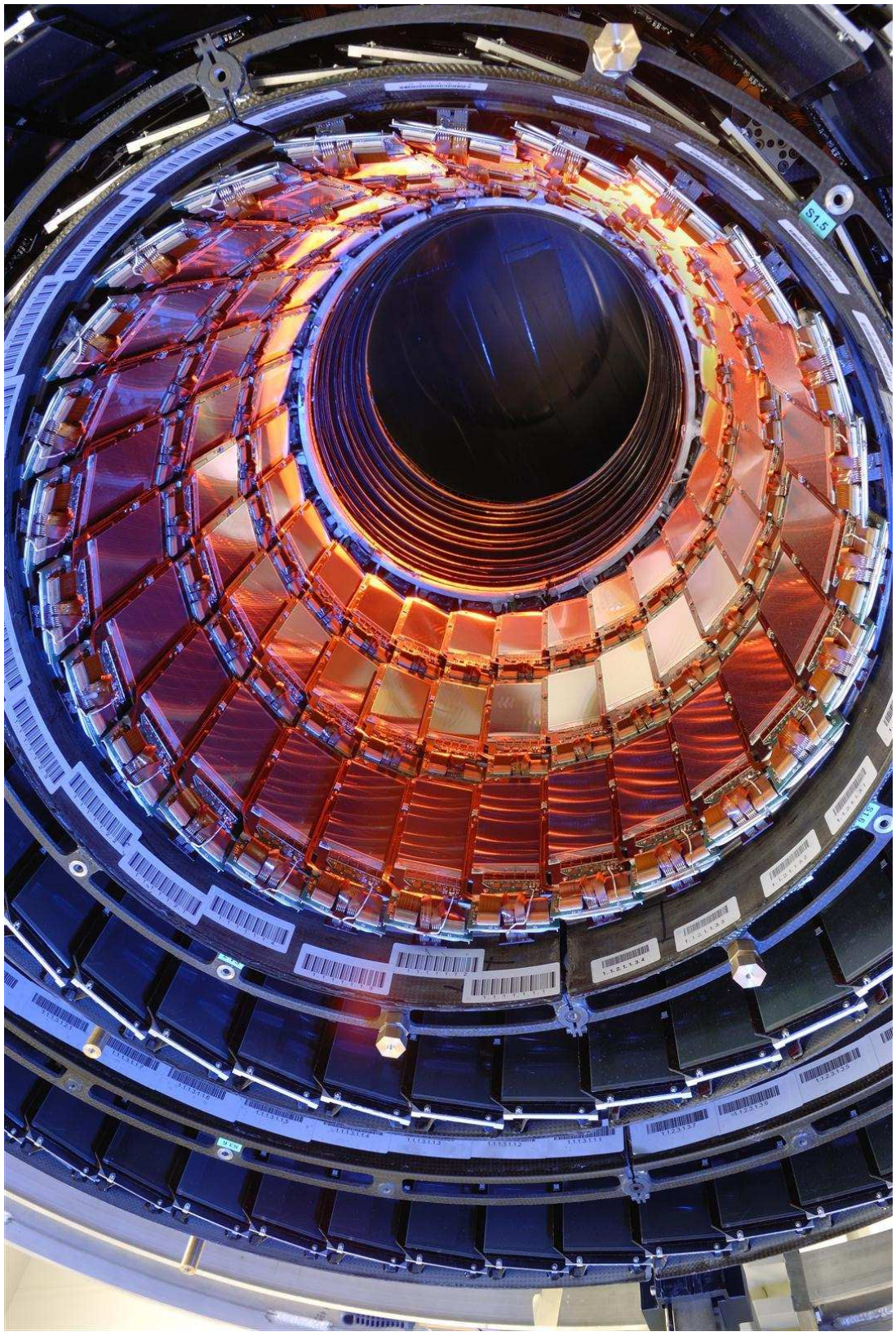

The CMS tracker.

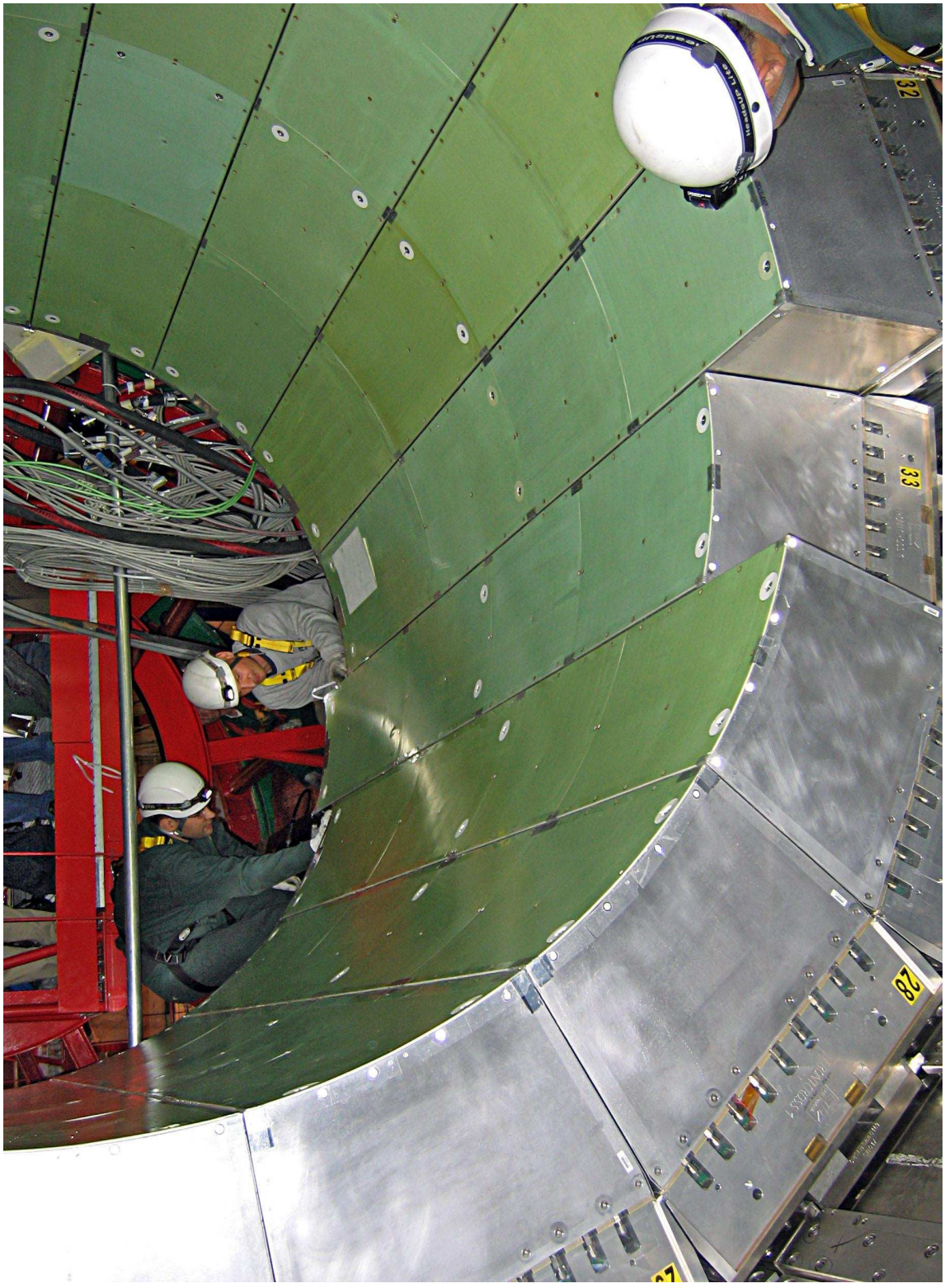

The CMS Electromagnetic Calorimeter.

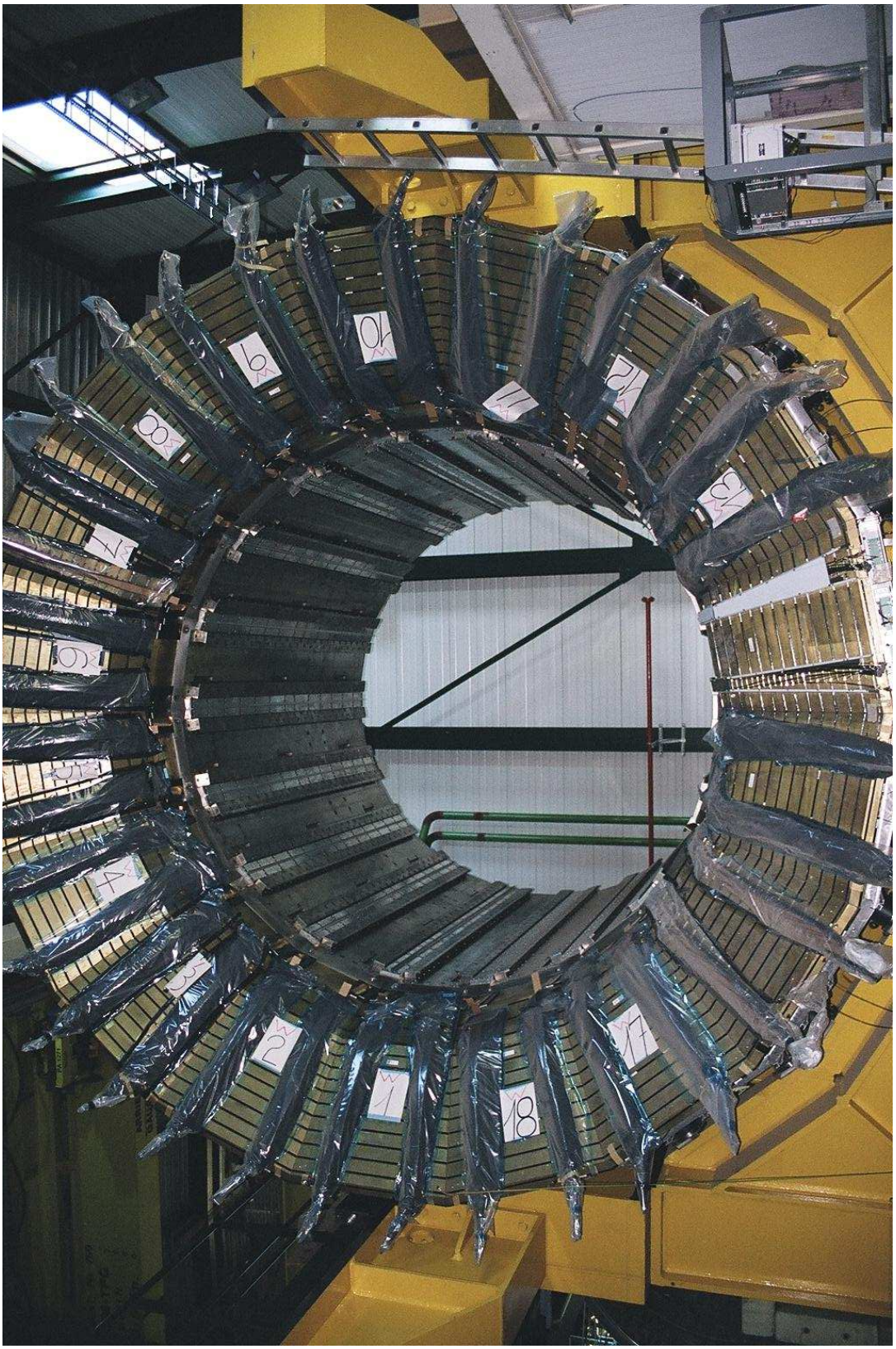

The CMS Hadron Calorimeter.

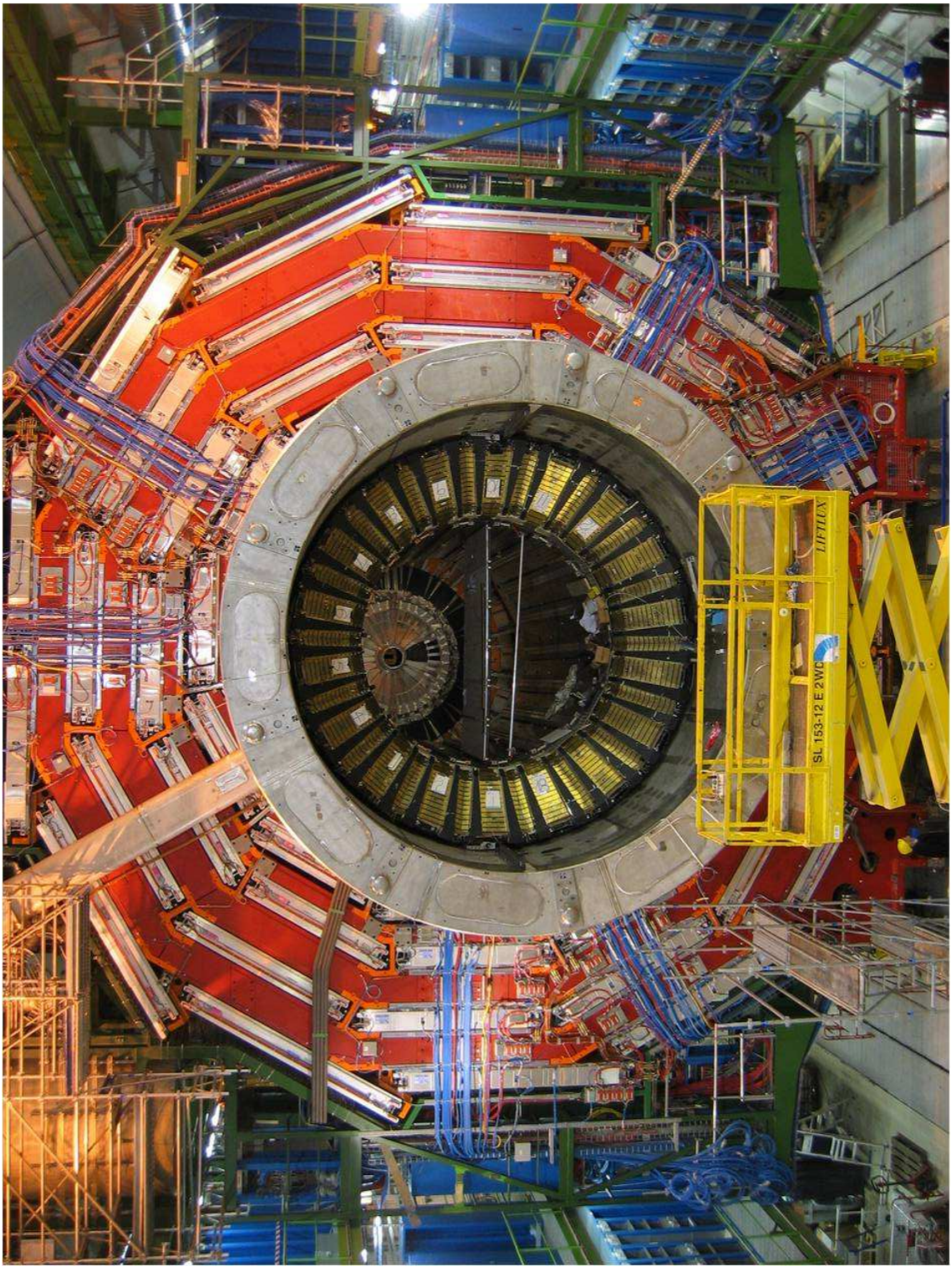

View of one of the wheels installed with barrel muon chambers.

View of one of the end-cap discs installed with muon chambers.

Chapter 2

Measurement of the charge ratio of cosmic ray muons using CMS data

In this chapter we present the measurement of the muon charge ratio using CMS data, collected at the *Magnet Test and Cosmic Challenge*, exploiting the capabilities of the drift-tube muon chambers of CMS. The analysis is performed using the standard CMS reconstruction software, as well as data distribution and job submission Grid tools, in a way similar to that designed for the analysis of the data produced in the proton-proton collisions at LHC.

Given the high complexity of the CMS detector, it is essential to test and verify all its components at every step of the construction and assembly procedure, in order to ensure the optimal functioning of CMS when LHC delivers the first beams in 2008.

The detector was pre-assembled in a surface hall (SX5) before being lowered to the cavern. A crucial milestone in the construction of CMS is the *Magnet Test and Cosmic Challenge* (MTCC) [42], a major test of a slice of CMS –performed on the surface– devoted to test the detector: magnet, readout electronics, trigger and data acquisition system (DAQ), alignment, calibration and reconstruction algorithms. High energy muons from cosmic rays are used as a particle beam for this test. Physics studies are not among the primary goals of the magnet test, however it provides high quality data –from a large number of cosmic muons– that can be used to perform measurements of physical quantities related to cosmic muons.

The *muon charge ratio*, R, is defined as the ratio of the number of positive- to negative-charge cosmic muons. Atmospheric muons stem from cosmic ray showers, produced via interactions of high-energy cosmic-ray particles entering the upper layers of the atmosphere with air nuclei: (p, He, ..., Fe) + A $\rightarrow$ hadrons, $\mathrm{e}^{\pm}\gamma$, where ($\pi^{\pm}$, $\mathrm{K}^{\pm}$) $\rightarrow \mu^{\pm} + \nu_{\mu}\,(\bar{\nu}_{\mu})$ and $\mu^{\pm} \rightarrow \mathrm{e}^{\pm} + \nu_{\mu}\,(\bar{\nu}_{\mu}) + \nu_{\mathrm{e}}\,(\bar{\nu}_{\mathrm{e}})$. The charge and momentum dependence of R is determined by the meson production cross sections in these high-energy hadronic interactions. The collisions of cosmic rays with air (both are mainly protons and nuclei) favour the production of positive mesons, hence more positive muons are expected. In a compilation of measurements, the charge ratio was approximately constant, $N_{\mu^+}/N_{\mu^-} \approx 1.27$, with uncertainties increasing from 1% at a few hundred MeV/c to 6% at 300 GeV/c [43]. A more recent and precise measurement by the L3+C experiment at CERN found similar results in the range 20 GeV/c – 500 GeV/c [44]. At energies greater than a

few hundred GeV, a growing influence of kaons is predicted and therefore a resulting increase of the charge ratio is observed [45]. These measurements are used to constrain parameters relevant to low energy hadronic interactions and to better determine the atmospheric neutrino flux.

2.1 Experimental setup

The MTCC took place in the second half of 2006. Its main goal was to test the CMS detector using cosmic-ray muons, before it was lowered to the experimental cavern. Important parts of this challenge were: testing and commissioning the superconducting magnet (including cooling, power supply and control system), measuring the map of the magnetic field, checking the movement of the detector when the magnetic field was switched on/off, testing the functionality of the muon alignment system and performing a combined test of the sub-detectors available (tracker, ECAL, HCAL and muon system) in a 20° slice of the CMS detector, using as far as possible final readout, data acquisition and trigger systems. There are documents reporting the operational details of the MTCC [42] and a comparison of commissioning results with simulations [46].

The MTCC was split in two distinct phases of data taking with different objectives: phase I was devoted to test the integration of the different sub-detectors and the alignment, and phase II concentrated on performing a mapping of the magnetic field and dedicated muon system and trigger studies. In phase I, six tracker layers (comprising 133 single and double-sided Silicon Strip modules), two ECAL and fifteen HCAL modules were used. In phase II, a field mapper replaced the ECAL and tracker detectors. In both phases, the muon system consisted of a reduced setup of the DT (*Drift Tubes*), RPC (*Resistive Plate Chambers*) and CSC (*Cathode Strip Chambers*) detectors, including final cabling and electronics. A total of 36 CSC chambers in stations ME+1, ME+2, ME+3 from trigger sector 5 were instrumented in the end-cap at $z > 0$ (covering a 60° sector, together with the RPCs).

From the installed muon barrel detectors, a total of 21 RPC chambers and 14 DT chambers were read out. Concerning the DTs, which are the detectors that provide the information for this analysis, the setup comprised stations MB1 to MB4 in sector 10 of wheel YB+1 and in sectors 10 and 11 of wheel YB+2 (covering a 30° and a 60° sector, respectively). The MB4 station at the bottom of sector 10 is split in two chambers, which is particularly relevant to the analysis.

The basic detection element of a drift tube chamber is a 42 mm × 13 mm drift cell (wire-length ≈ 2.5 m, depending on the chamber type) filled with an Ar/CO_2 gas mixture. Four layers of staggered drift cells form a superlayer (SL) and three superlayers build up a chamber or station (St), with a total 12 layers of drift cells. The signal left in the drift cell due to the passage of a muon is called *hit*. As mentioned in Section 1.2.2, the bending of the muon trajectory in the r-ϕ plane of CMS is measured by the two ϕ-SL while the third, the θ-SL, determines the perpendicular coordinate in the r-z plane. A honeycomb panel of $\sim$ 128 mm thickness placed between the θ-SL and one ϕ-SL gives rigidity and a bigger lever arm to the ensemble. The only exception of this scheme are the outermost MB4 chambers containing only two ϕ-superlayers. Figure 2.1 (top) depicts the experimental setup of the MTCC in the muon barrel system. A cosmic muon detected in CMS during the MTCC is displayed in Figure 2.1 (bottom).

Around 25 million "good" events were recorded with at least DT triggers, of which 15

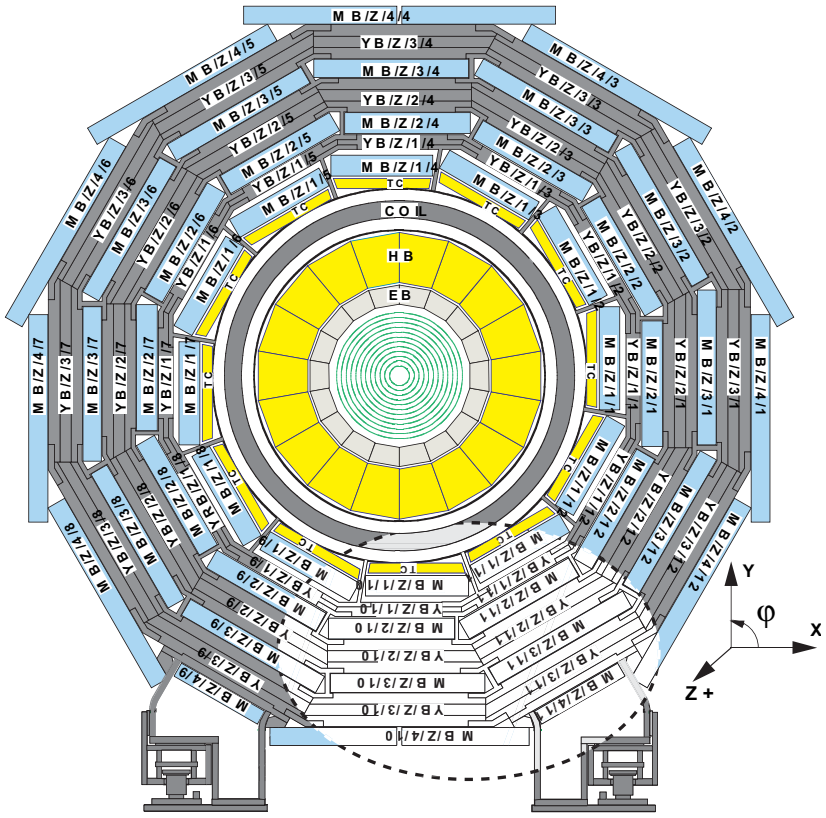

Barrel wheels YB+2 (S10, S11) and YB+1 (S10)

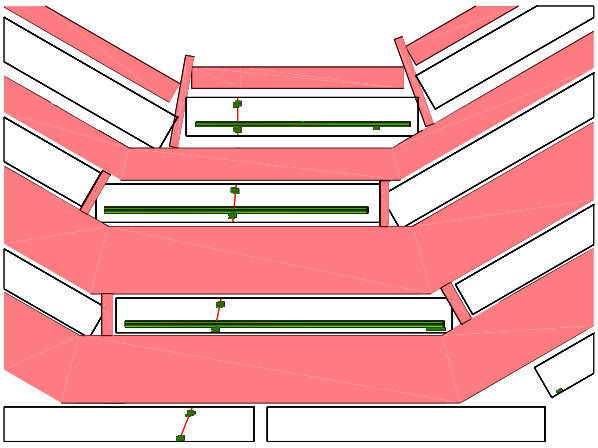

Figure 2.1: (Top) Transverse, r-ϕ, view of the muon barrel experimental setup of the MTCC. The slice used in the test, in lighter colour, is enclosed in an ellipse-shaped dashed line. (Bottom) A cosmic muon observed with the CMS detector during the MTCC. The green dots and straight lines indicate the hits in the muon system, the thin red lines showing the reconstructed muon track.

million were at a stable magnetic field above 3.8 T. The data files were transferred from SX5 to a disk pool (CASTOR) at the CERN site (Tier-0) and processed quasi-online. Both raw and processed data were distributed to several Tier-1 centers (Fermilab and PIC, for example) using PhEDEx [47] and subsequently transfered to various Tier-2 centers (like CIEMAT). Skimming jobs were submitted to LCG (the LHC Computing Grid), using the standard CMS job submission tool [48], and the output was collected at Tier-3 centers where the final analysis was performed.

2.2 Data samples

One important milestone of the MTCC was to establish the proper functioning of the data acquisition system using different trigger configurations.

In the MTCC a subset of the final readout and trigger electronics [49] was operated for triggering and data taking. A first level trigger was provided by the DT system, the CSC system and the barrel RPCs. The trigger input was processed and distributed to CMS by the Local Trigger Control (LTC) which assigned a trigger bit for the sub-detector generating the trigger signal. This information was used to select events triggered by, for example, drift tube chambers. The trigger logic had to be modified with respect to LHC operation conditions to take into account that cosmic muons traverse the detector mainly from above. The angular acceptance per chamber was maximal in order to allow for muons arriving from all directions and not only from the interaction point. This yielded a large amount of data collected in quite different working conditions of the detector.

In order to guarantee the uniformity of the muon sample, only events triggered by the DTs are accepted for the analysis presented in this chapter. Furthermore, the analysis is performed with the information from the DT muon chambers alone hence, nearly vertical muons are selected. Data samples corresponding to five MTCC runs are used in this analysis, all taken under similar trigger conditions and at nominal or close-to-nominal values of the magnetic field. Run 2377 was taken during phase I, before the tracker modules were replaced by the instruments to map the magnetic field. The rest of runs correspond to phase II, either at an early stage (run 4045) or at the end of the data taking (runs 4406, 4407, 4409). At this last stage, the experience and improvements gained in operating the magnet and the muon system resulted in the better quality of the data compared to earlier runs. Table 2.1 details the MTCC runs used in the analysis, along with their magnetic field, trigger configuration, numbers of events and fraction of events triggered by the DTs relative to the total number of triggered events. All the runs used in the analysis have a common trigger configuration of stations MB2 and MB3, a condition that provides a uniform muon sample, trigger-wise, for all the runs. A run collected at $B = 0$ T (run 3809, from phase II) is used as a control sample to perform detailed checks of the detector performance, as will be shown in Section 2.3.

The CMS detector is built to detect and measure the properties of particles produced in a central vertex from LHC-delivered proton-proton collisions. The flight direction of cosmic-ray muons and the randomness of their arrival time make these particles behave quite differently, CMS wise, from those coming from the nominal interaction vertex, requiring special reconstruction software and calibration procedures, as well as special trigger configurations.

The events are reconstructed using the standard reconstruction software [50] of the CMS

Run	B(T)	Trigger conditions	Events	DT trigger rate
2377	3.67	DT (MB2, MB3), CSC (first 160703 events); CSC, DT, RPC (from event 160704)	613 174	20 %
4045	3.8	DT (MB1, MB2, MB3) or CSC	3 110 980	32 %
4406	4	DT (MB2, MB3) or CSC	1 825 273	23 %
4407	4	DT (MB2, MB3) or CSC	1 665 440	23 %
4409	4	DT (MB2, MB3) or CSC	2 563 020	23 %
3809	0	any two DT chambers coincidence	611 407	99 %

Table 2.1: Run numbers, magnetic field (values in Tesla), numbers of events and fraction of events triggered by the DTs relative to the global trigger rate, for the MTCC runs used in the analysis. All runs are from MTCC phase II, except run 2377.

experiment. The so-called *standalone muon reconstruction* was adapted for dealing with the specific spatial configurations of cosmic muons [51]. The measured muon momentum and angles are calculated with respect to the entry point of the muon in the innermost DT station (MB1 or MB2) The reconstruction procedure uses special DT calibration constants, in order to have a common reference for trigger synchronization [52]. This special calibration is crucial to account for the random arrival time of cosmic muons. Alignment corrections [53], calculated from survey data [54], are applied to the measured hits before the track reconstruction. Alignment, being the main source of systematic uncertainty in this analysis, in particular for particles with momentum higher than about 100 GeV/c, deserves a more detailed study (Section 2.4).

While this analysis is mostly data driven, simulated samples of cosmic muons that reproduce the MTCC setup exist [46] and are used for cross checks and to extract some corrections (Section 2.4). Two samples of about one-million events are generated with the CMSCGEN program [46], one with zero magnetic field and the other with $B = 4$ T. After full simulation, digitization, reconstruction and trigger simulation (the latter is done as explained in [46]), less than 1% of these simulated events fulfill the MTCC acceptance and trigger conditions.

In order to select events containing well-reconstructed muons, the following preselection criteria are required:

1. more than 6 hits in both ϕ superlayers of the MB2 and MB3 stations, for both wheels YB+1 and YB+2,
2. at least one reconstructed muon track in the DTs,
3. all the hits of the muon track must be in sector 10,
4. the point of closest approach of the muon track to the nominal CMS center must be inside the magnet volume, which is a special feature of the *CosmicMuonReco* code [51].

The numbers of events surviving these criteria are listed in table 2.2 (left), together with the relative efficiencies of the cuts (relative to the numbers of events triggered by the DTs), for the runs used in the analysis. The number of preselected events in the simulated sample is 4 090.

Distributions for preselected events corresponding to three runs and the simulation (MC) are displayed in Figure 2.2: transverse momentum of the muon tracks for low- and high-p_{T} ranges, their azimuthal (ϕ) and polar (θ) angles, and their incidence angle with respect to the vertical direction – all measured at the innermost station –, together with the number of reconstructed hits per track. Run 4406 is representative for 4407 and 4409, since the three runs were taken under identical conditions. The prominent peaks in Fig. 2.2 (lower right) at 24 hits, 32 hits, 36 hits and 44 hits correspond to tracks leaving signals in different chambers; MB1, MB2 and MB3 can contribute with 12 hits at most while MB4 only contains 8 layers, thus the combination of the different chambers explains the observed pattern. The distributions are normalized to one and only error bars are shown for the simulated events, due to the tiny size of the statistical errors for the data histograms, as compared to the simulated events. The global CMS coordinate system is used, in which the z axis goes along the beam-line, that is, $\phi = -90°$ and $\theta = 90°$ for vertical muons.

Preselection		
Run	Events	Relative efficiency
2377	40 650	35 %
4045	280 165	28 %
4406	147 471	35 %
4407	135 209	35 %
4409	207 985	35 %
Total	811 480	32 %

Selection		
Run	Events	Relative efficiency
2377	3 693	9 %
4045	37 748	13 %
4406	18 311	12 %
4407	16 568	12 %
4409	25 786	12 %
Total	102 106	12 %

Table 2.2: Numbers of events and relative efficiencies of the cuts, per run and for all runs together, after preselection (left) and selection (right) criteria are applied. The definitions of the relative efficiencies are detailed in the text.

The agreement among data from the different runs is excellent, in particular for those with the same trigger conditions. A slight difference in the ϕ distribution is observed for run 4045, which is due to its different trigger configuration. Run 2377 serves as a good example of the difficulties found in the analysis of the MTCC data, especially during phase I: the trigger configuration changed with time, there were problems in wheel YB+2 and instabilities in the global DAQ. All this caused a lower efficiency and some distortions visible in the distributions of Figure 2.2.

Good agreement of the simulations with the data is also observed, after scaling the momentum of the simulated events by a factor of 1.25 to better describe the data. Some disagreement is visible at very low momentum, due to the cut $p > 7$ GeV/c for simulated events, and in the number of hits per track, as noise and dead cells are not included in the simulations.

2.3 Analysis and event selection

The analysis aims to select a sample of high quality muons, obtaining the momentum spectra for positive and negative muons, and calculating the charge ratio as a function of the momentum, $R(p)$. Given the experimental setup, the mean value of the charge ratio and its uncertainty are expected to be dominated by the measurements at low momentum, below $p \sim 100$ GeV/c.

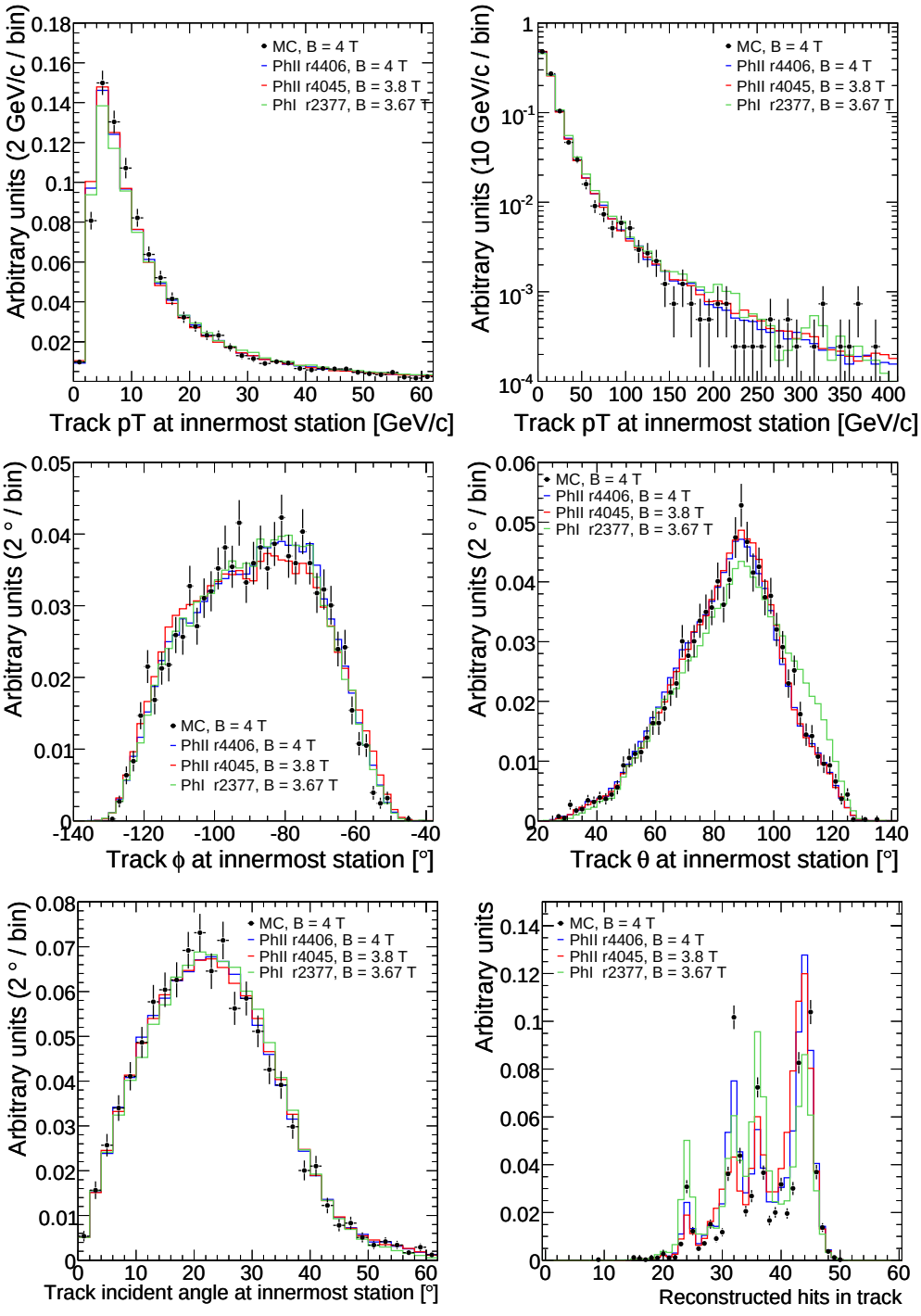

Figure 2.2: Normalized distributions of the p_T-momentum of the muon tracks (upper two), their azimuthal (central left), polar (central right) and incidence (lower left) angles, measured at the innermost station, and the number of reconstructed hits per track (lower right), for preselected events. The coloured lines correspond to data from different runs and dots with error bars to the simulated events (MC). This unusual choice is due to the tiny size of the statistical errors for the data histograms, as compared to the simulated events.

In order to make the analysis mostly data driven, that is, to avoid its dependence on detailed simulation studies and corrections, some important considerations are taken into account. Muons leaving signals in either two (*doublets*), three (*triplets*) or four (*quadruplets*) DT stations, have different numbers of hits, yielding different momentum resolutions. The μ^+ and μ^- populations must have similar momentum resolution, therefore the analysis is done in a way not to favour any particular charge and quality (at the same time), which is achieved by requiring good muons to be quadruplets in the muon system. This is particularly important at high momentum, $p \gtrsim 100$ GeV/c, where momentum resolution worsens significantly.

Due to the magnetic field, unlike-sign charged particles bend in opposite directions in the r-ϕ plane (transverse to the beam axis), populating different regions of the detector. This, together with the trigger configuration (MB2+MB3) and the geometry of the detector, introduces a bias in the relative detection efficiency of μ^+ and μ^-. The trigger-induced asymmetry is visible, for example, in the distribution of hits in the detector, shown in Figure 2.3 (left) for run 3809. Since this run was collected at $B = 0$ T, the observed effect is independent of the muon charge. In order to avoid such bias in the relative efficiency of μ^+ and μ^-, the fiducial geometric acceptance of the detector is constrained to be left-right symmetric with respect to the axial (vertical) axis of the detector in the r-ϕ plane. In addition, the detector efficiency within the fiducial volume must also be left-right symmetric in r-ϕ (though not necessary flat). The graph in Figure 2.3 (right) helps understanding the influence of the geometric acceptance in the relative efficiency for μ^+ and μ^- with the same momentum, entering the detector in symmetric points, and with the same angle, with respect to the vertical axis.

A high-quality sample of *golden* muons that avoids biasing the relative acceptance of positive and negative muons is selected as follows:

- All reconstructed muon tracks must have at least one hit per chamber (quadruplets). This ensures a precise measurement of momentum and angles.
- Only tracks going through a single wheel are considered: by discarding the small amount of wheel-crossing tracks, non-vertical muons are rejected and, more important, the relative alignment between wheels becomes irrelevant.
- The left-right symmetric fiducial geometry is imposed by requiring all the track hits to have a global X coordinate inside the region $[-60, 60]$ cm (Figure 2.3 (right)). The MB2+MB3 trigger efficiency is uniform and very high in this region. Furthermore, the muons selected in this geometry are close to vertical, with an entry angle to the DTs that ensures a good measurement in all the stations. The incidence angle for the golden muons is lower than 40°.

The requirement of having hits in all the stations ensures a number of hits per muon track close to the maximum, as illustrated in Figure 2.4(a) for run 4406. The resolution[1] in the

[1]The resolution in the momentum measurement is obtained from the simulation and is given by:

$$\sigma_\mu = \frac{1/p_{\mathrm{T}}(\text{reconstructed}) - 1/p_{\mathrm{T}}(\text{generated})}{1/p_{\mathrm{T}}(\text{generated})}$$

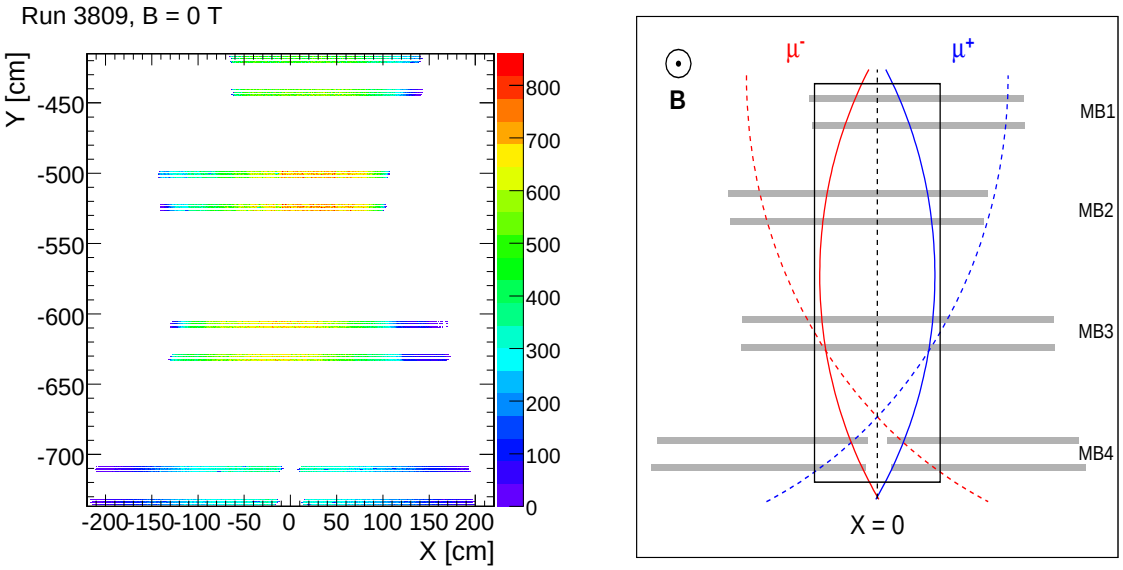

Figure 2.3: (Left) Distribution of preselected hits in global XY coordinates for run 3809 in sector 10, collected at $B = 0$ T. The non-uniform cell occupancy, due to the trigger configuration, is evident before symmetrizing the fiducial volume. (Right) Definition of the left-right symmetric fiducial geometry (black solid polygonal line) in the muon system. The dashed lines depict two muon tracks with the same momentum crossing sector 10, the negative one satisfying the MB2+MB3 trigger condition and the positive one failing it. The solid curves represent two muons with the same p in the fiducial geometry, both of them passing the golden muon selection criteria.

momentum measurement is better for this sample than for samples in which a smaller number of stations is required (Figure 2.4(b)) . In addition, possible asymmetries caused by trigger or detection inefficiencies are avoided by imposing the chosen fiducial region, $[-60, 60]$ cm. This is depicted in Figures 2.4(c) and 2.4(d) for runs 4406 and 4045, respectively, where the number of reconstructed hits for MB2 and MB3 stations is shown as a function of X for the whole range in sector 10. Both distributions are uniform within the fiducial region (marked by the vertical lines), hence no bias related to geometric position, and therefore charge, is introduced. The slightly different shape observed in these distributions for run 4045 is due to the different DT trigger conditions, as compared to other runs, and illustrates that this effect is larger outside the fiducial region.

Another high-quality selection [1], performed by considering a wider left-right symmetric region in each chamber and including MB1+MB2+MB3 triplets in the sample, yields consistent results.

The distributions of hits for selected events of run 4406, collected at $B = 4$ T, are displayed in Figure 2.5, separately for positive and negative muons in the fiducial volume of wheel YB+1. The two graphs are mirror images of each other (due to the different muon charges), reflecting the left-right symmetry of the fiducial geometry in the r-ϕ plane.

The numbers of events and efficiency of the cuts per run, after the selection criteria above are applied, are listed in Table 2.2 (right). The number of selected events in the simulated sample is 540. The distributions of the transverse momentum of the muon tracks, their azimuthal, polar and incidence angles, and of the number of reconstructed hits per track, are shown in Figure 2.6 for the selected events from runs 2377, 4045 and 4406, and for the simulation. The selection of golden events improves the quality of the distributions, making the differences among runs very small. Simulation reasonably agrees with data, despite its relative lack of realism: detector noise, dead cells and cell inefficiencies are not in the simulation, and the trigger is modeled only approximately. The ratio of selected to preselected events is consistent among runs, both for μ^+ and μ^-.

Quality control of the detector performance

Non-uniformities of the detector –hot spots, dead or inefficient regions– would impact differently the detection efficiency of unlike-sign charged particles, introducing a bias in the measurement of the charge ratio. Both the uniformity of the detector and the left-right symmetry of its efficiency within the fiducial volume are verified at different levels of the selection procedure. This is done using our control data sample collected at $B = 0$ T, run 3809, which is therefore not used in the analysis.

Almost vertical straight muons are further selected requiring tracks with an incidence angle below 20°. In addition, a lower cut on the track momentum is imposed at 15 GeV/c, in order to reject tracks significantly bent by multiple scattering in the magnet yoke. These selected muons uniformly illuminate the fiducial volume of the muon detector. The symmetric behaviour of the detector –in terms of cell occupancy– is assessed, in a layer-by-layer basis, using the distribution of hits as a function of the global X coordinate in two halves of the selected region, folding the $-X$ side onto the $+X$ one, in the $[0, 60]$ cm range, and checking the compatibility. This is done for all the 64 r-ϕ layers of the muon detector (4 r-ϕ layers per superlayer, 2 ϕ superlayers

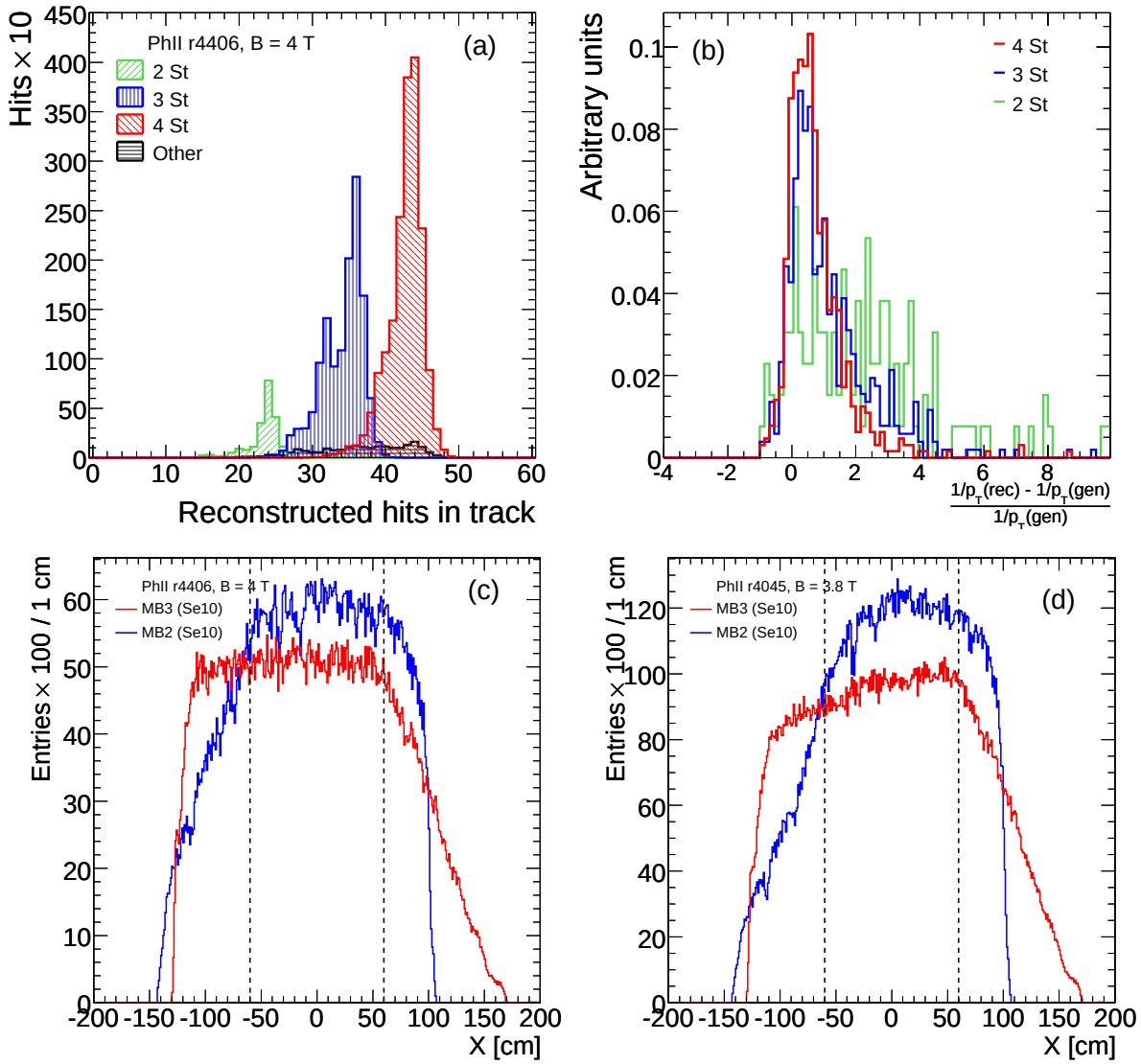

Figure 2.4: (a) Number of cell hits contributing to doublets (2 St), triplets (3 St) and quadruplets (4 St) in the selected region for run 4406. For the golden muons (quadruplets), the number of hits per track is higher (centered at 44 hits). (b) Resolution in momentum measurement for doublets, triplets and quadruplets in the selected region, obtained from the simulation. The distributions are normalized to 1. The resolution is better for quadruplets (narrower and with shorter tails) than for triplets and doublets. (c), (d) Number of cell hits, as a function of the global X coordinate, for MB2 and MB3 stations in the whole range in sector 10. Both distributions are uniform within the chosen fiducial region (marked by vertical lines). Results shown for runs 4406 (c) and 4045 (d).

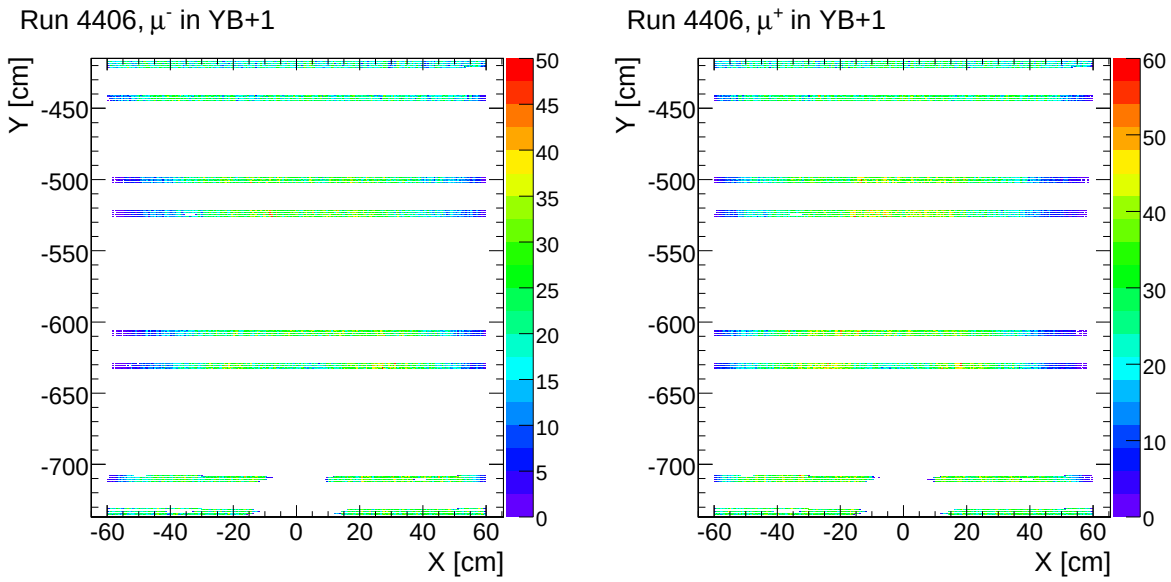

Figure 2.5: Distribution of hits in global XY coordinates, for (left) negative and (right) positive muons of run 4406 ($B = 4$ T) in wheel YB+1, after selection cuts are applied.

per station, 8 stations in total). As an example, Figure 2.7 shows these distributions for four particular layers. The dead cells (less than 1% of the total) have a negligible effect in the track reconstruction.

2.4 Results

The measurement of the muon charge ratio, R, is computed as the ratio of the p spectrum of positive muons to that of negative muons, as a function of the reconstructed muon momentum (p),

$$R(p) = \frac{N_{\mu^+}(p)}{N_{\mu^-}(p)}$$

The momentum spectrum rapidly decays for increasing p values, hence the size of the p bins is chosen so as to have a minimum number of events that allow proper calculation of that ratio. The bin edges, in GeV/c, are 0, 5, 10, 15, 30, 60, 100, 200 and 1000 (infinity, indeed). In the charge ratio graphs, the average momentum in each bin is taken as the p value, rather than the center of the bin.

The measured muon charge ratio and its statistical uncertainty are displayed in Figure 2.8 for the individual runs analyzed and their combination (large red dots). The latter will be referred to as *MTCC data* hereafter. The charge ratio is mostly momentum independent, up to $p \simeq 200$ GeV/c. The deviations observed among different runs are consistent with statistical fluctuations, giving confidence on the result.

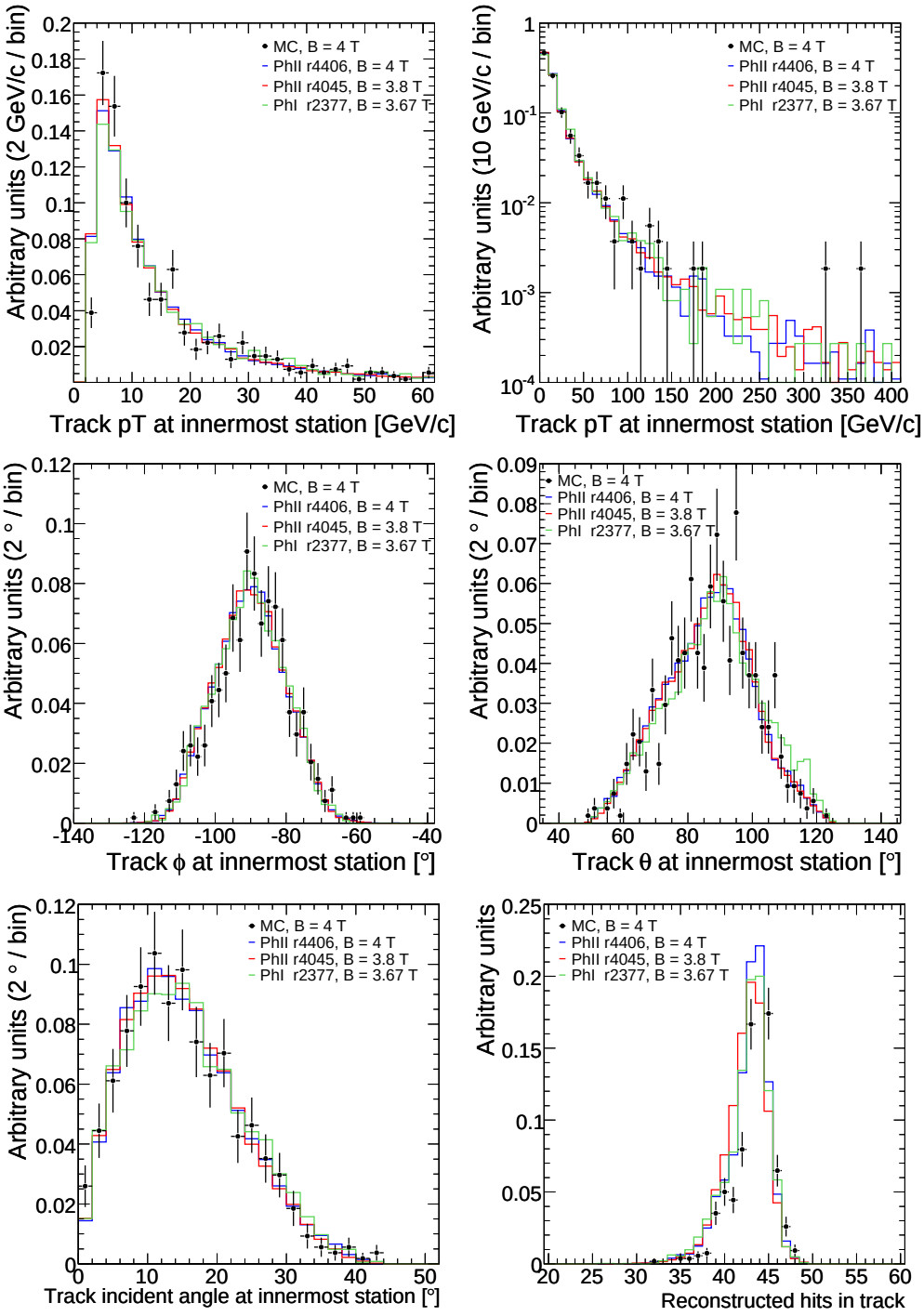

Figure 2.6: Normalized distributions of the p_T-momentum of the muon tracks (upper two), their azimuthal (central left), polar (central right) and incidence (lower left) angles, measured at the innermost station, and the number of reconstructed hits per track (lower right), for selected events. The coloured lines correspond to data from different runs and dots with error bars to the simulated events.

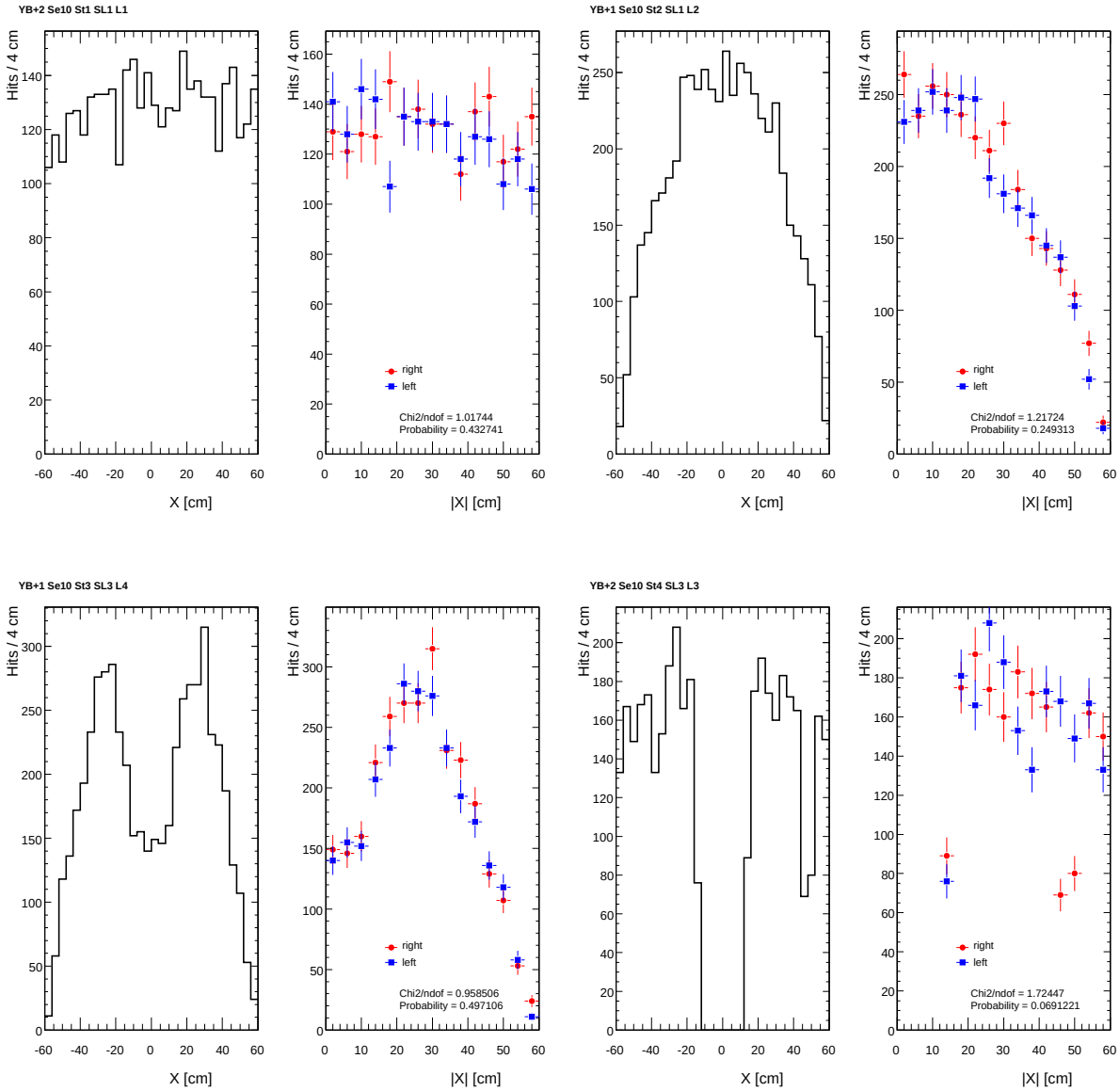

Figure 2.7: Distribution of hits as a function of the global X coordinate (histograms), in the $[-60, 60]$ cm range for four r-ϕ layers. Comparison of the left (dots) and right (squares) sides of the hit distribution in those layers as a function of the absolute value of X. The compatibility between both sides is given in terms of the $\chi^2/ndof$ of the distributions. The data of the distributions are from run 3809, taken at $B = 0$ T.

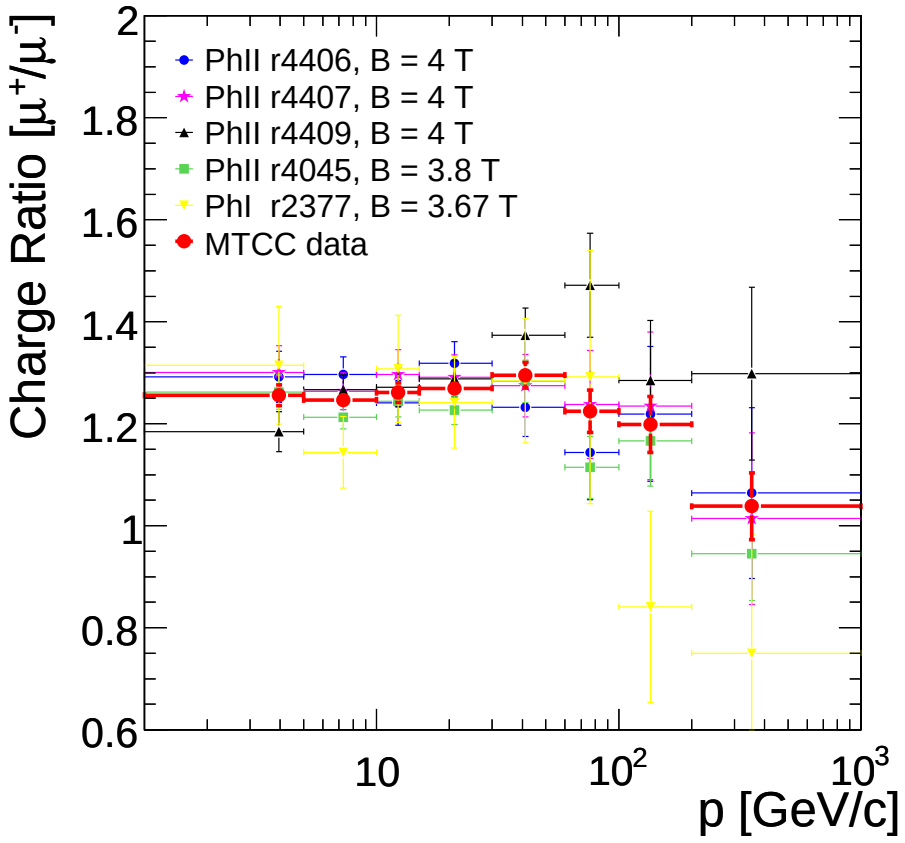

Figure 2.8: Measured muon charge ratio, as a function of the reconstructed muon momentum, for the individual runs and their combination (large red dots). The error bars indicate the statistical uncertainty.

Charge confusion correction

Due to the detector momentum resolution, the probability for the correct assignment of the muon charge is not 100%, making the measured charge ratio deviate from the true value. Assuming the muon charge misidentification probability (charge confusion), $C(p)$, is charge symmetric, the observed numbers of μ^+ and μ^- ($N_{\mu^\pm}$) are functions of the true numbers of μ^+ and μ^- ($N^\circ_{\mu^\pm}$),

$$N_{\mu^\pm} = (1 - C)\, N^\circ_{\mu^\pm} + C\, N^\circ_{\mu^\mp}$$

where the p dependence is not made explicit for clarity. The *true* muon charge ratio, R°, expressed in terms of the observed quantity, is

$$R^\circ = \frac{R - C\,(1 + R)}{1 - C\,(1 + R)}$$

It is important to realize that the charge ratio must be corrected for charge confusion. The unavoidable presence of charge confusion will always lead to a measured charge ratio closer to one than the actual charge ratio. When the charge confusion is maximal ($C_{\max}(p) = 50\%$), all significance on the charge measurement is lost: the chance of measuring the correct charge sign is as large as the chance of measuring the opposite sign. The measured charge ratio will obviously approach 1. The level of charge confusion itself also naturally limits the maximum possible charge ratio that can be measured.

A linear parameterization of $C(p)$ is made, as a function of p, using simulated events that pass the selection cuts (Figure 2.9 (left)). The value of C is less than 2% for low momentum tracks, below $p \simeq 30$ GeV/c, and increases significantly (up to 25%) for high momentum muons, above $p \simeq 200$ GeV/c. The effect of the charge confusion correction in the measurement of the charge ratio is displayed in Figure 2.9 (right).

2.4.1 Consistency checks

A number of checks have been performed in order to test the robustness of the analysis. In particular, the charge ratio R is calculated, integrated over p, as a function of the polar and incident angles, as displayed in Figure 2.10 (left and right). No structure is found in any of the two distributions.

As an additional cross check, R is depicted in Fig. 2.10 (bottom) as a function of the momentum for run 3809, collected at $B = 0$ T. Since there is no magnetic field, the tracks – reconstructed as if B was 4T – are straight and there is no valuable information about the muon momentum and charge. In this case, the charge confusion is maximal in the whole range of momentum and therefore R is consistent with 1. This result supports the robustness of the analysis even in odd conditions.

2.4.2 Estimation of systematic uncertainties

Given the constraints imposed by the experimental setup – not being optimized to perform physics studies – a conservative approach in the estimation of systematic errors has been adopted. The main sources of systematic uncertainty affecting the measurement of the charge ratio are

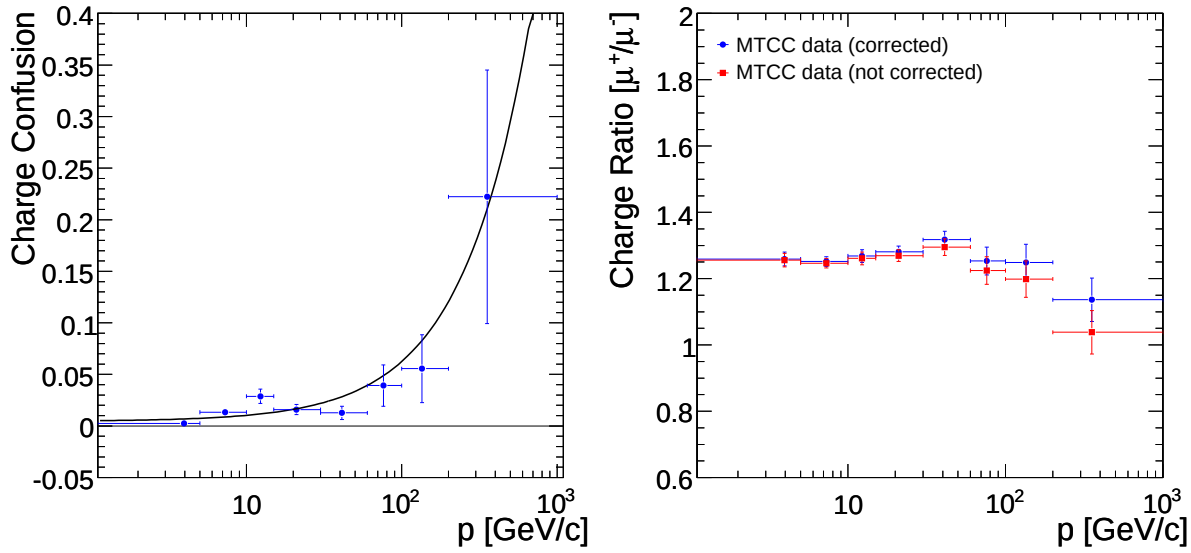

Figure 2.9: (Left) Charge confusion calculated using simulated events. (Right) Effect of applying the correction due to charge confusion to the measured charge ratio, for the MTCC data. The error bars indicate the statistical errors in both cases.

the selection cuts, mainly the choice of the geometrical fiducial region, the charge confusion and the alignment of the muon detector. Neither significant effect of the value of the magnetic field on the charge ratio nor variations of the charge ratio as a function of the incidence angles of the muons, have been observed. Therefore, no systematic errors are associated to either the magnetic field or the angular variables.

Fiducial region

The fiducial geometry used in the analysis is a rectangular box with horizontal dimension 120 cm, corresponding to the global X range $[-60, 60]$ cm. Arbitrarily varying the size of the box in this coordinate by 10%, where effects like lower trigger efficiency, physical end of the MB1 station or reduced statistics play a role, produces deviations of the charge ratio within 1%, independent of the muon momentum.

Charge confusion

While the charge confusion in the simulations is not expected to accurately reproduce that of data to a very high degree of accuracy, the large errors in the parameters of $C(p)$, dominated by the small number of simulated events, exceed the expected accuracy. Hence, these errors are considered a systematic uncertainty in the determination of the charge ratio. The systematic uncertainty due to charge the confusion correction is less than 1% for $p \lesssim 100$ GeV/c and increases up to 7% at 1 TeV/c.

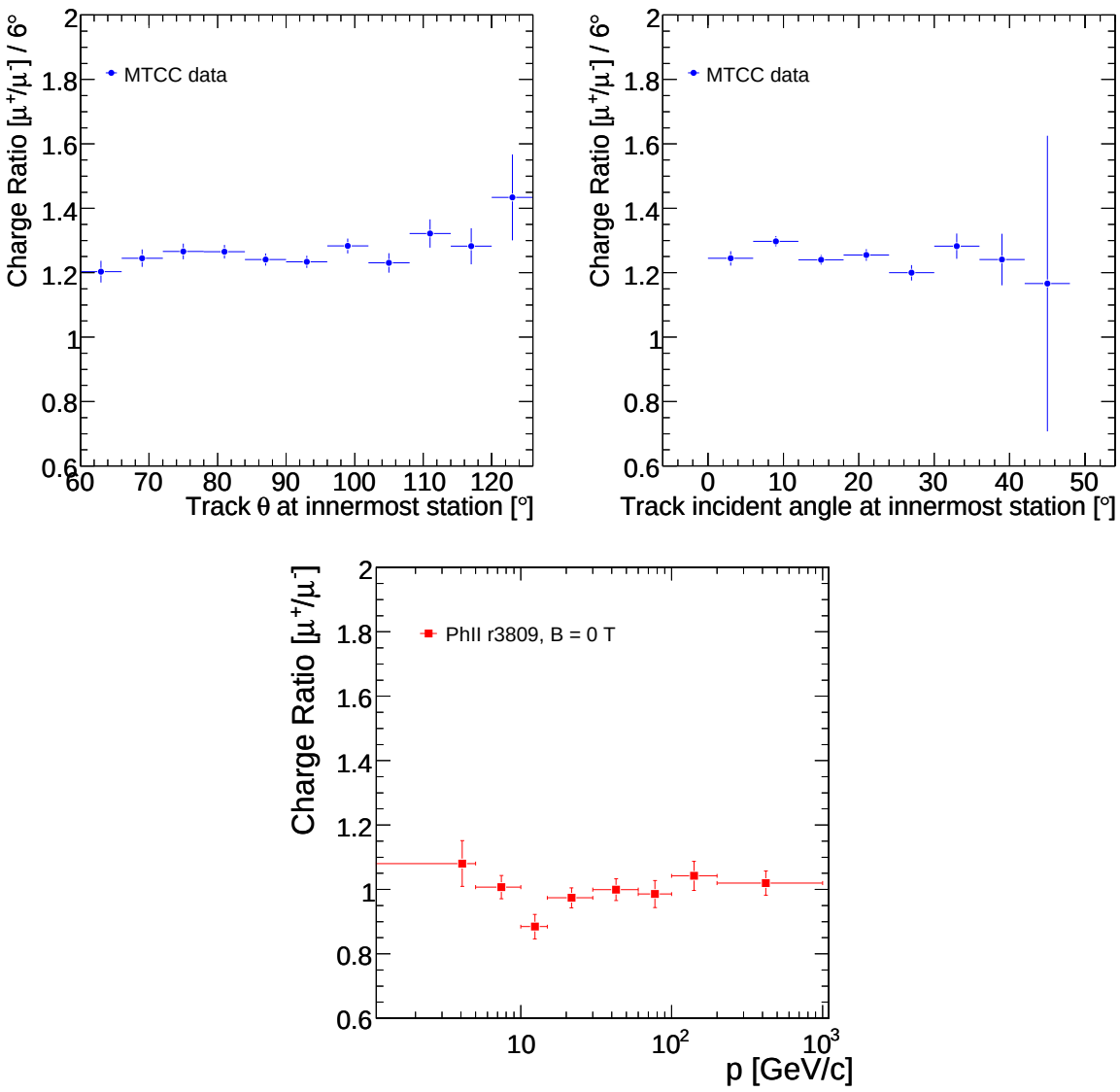

Figure 2.10: (Left) Charge confusion calculated using simulated events. (Right) Effect of applying the correction due to charge confusion to the measured charge ratio, for the MTCC data. The error bars indicate the statistical errors in both cases.

Alignment

The relative alignment of the muon chambers plays a crucial role in the analysis. Deviations from an ideally aligned detector yield systematic shifts in the measured muon momentum and, at high momentum, even swap the muon charge. Most important, these deviations are non-symmetric for μ^+ and μ^-, having a potentially large impact in the measurement of the charge ratio, in particular for high momentum muons. The golden sample of muons used in this analysis is composed by quadruplets, therefore it is particularly important the alignment of the two MB4 stations in each sector 10, since they are mechanically decoupled.

The alignment constants used to correct the hit positions prior to track reconstruction are extracted from survey data [53,54]. The impact of the alignment on the measurement is evident in Figure 2.11, where the charge ratio is displayed in two scenarios: aligned and not-aligned. Results are shown for the combination of all runs within each wheel and their average value (two upper plots) and for the individual runs in each wheel (two lower plots).

The charge ratio measurement averaged over the two wheels (whole sample), presents a flat shape for the aligned scenario with respect to the case in which misalignment is not corrected for. In both cases, aligned and not-aligned, there is a systematic difference in the charge ratio calculated in the two wheels separately for high momentum, $p \gtrsim 100$ GeV/c, which is consistent for all runs.

The systematic error due to misalignment is estimated by varying the alignment constants within their errors, and quantifying the variation induced in the charge ratio. These errors are smaller (around 4 to 8 times) than the correction itself, which reflects the importance of the alignment correction. R is obtained in two rather pessimistic scenarios in order to test the stability of the result: "+ - - +", which consists in displacing stations MB1 and MB4 "1σ" in global X coordinate to the left and stations MB2 and MB3 "1σ" to the right, and "- + + -", which is exactly the opposite displacement of the chambers. This is illustrated in Figure 2.12 as a function of the measured momentum (histograms). The reference values of R in each wheel are shown again for comparison. A complementary treatment of the misalignment uncertainties [1] based on a toy Monte Carlo study yields consistent results for the systematic uncertainty.

The systematic uncertainty is obtained by rescaling the difference of the reference value of R to the probed scenario by a factor of 2, which is the expected value for more realistic scenarios and consistent with the difference in the charge ratio measured in the two wheels separately.

The individual systematic uncertainties on the charge ratio measurement are summarized in Figure 2.13, as a function of the measured muon momentum, together with the statistical error. The most important contribution arises from the alignment correction, especially for $p \gtrsim 100$ GeV/c. The total systematic uncertainty is lower than 5% for muon momentum below 60 GeV/c and increases up to 30% for higher momentum.

2.4.3 Final result

The measurement of the *true* charge ratio, R°, using CMS data is depicted in figure 2.14 as function of the measured muon momentum, along with the statistical and systematic uncertainties, and the corresponding values are listed in Table 2.3. Given the experimental accuracy,

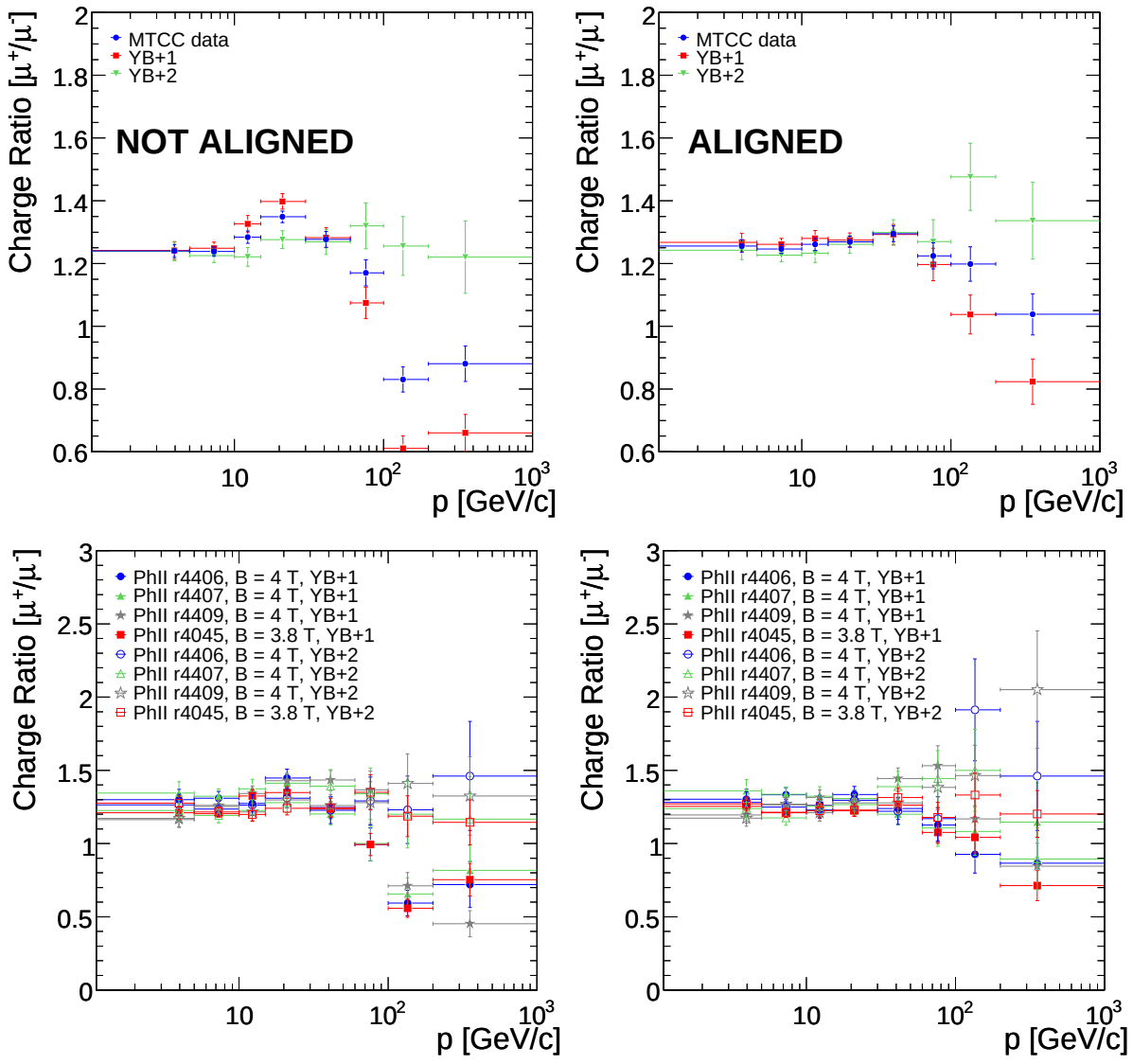

Figure 2.11: Charge ratio, as a function of the measured muon momentum, without (upper left) and with (upper right) the alignment correction, in the two wheels (red squares and green triangles) and their average value (blue dots) for the MTCC data. The charge ratio as a function of the measured momentum in each wheel is also displayed for the individual runs, both in the not-aligned (lower left) and aligned (lower right) scenarios. The filled markers correspond to wheel YB+1 and the empty markers to YB+2. The error bars in all the plots denote the statistical error.

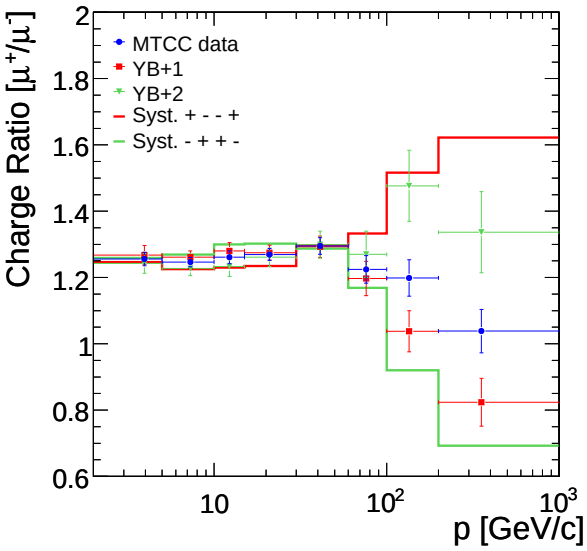

Figure 2.12: Charge ratio, as function of the measured muon momentum, obtained for two rather pessimistic alignment scenarios: "+ - - +", which consists in displacing stations MB1 and MB4 "1σ" in global X coordinate to the left and stations MB2 and MB3 "1σ" to the right (red histogram), and "- + + -", which consists in displacing stations MB1 and MB4 "1σ" to the right and stations MB2 and MB3 "1σ" to the left (green histogram).

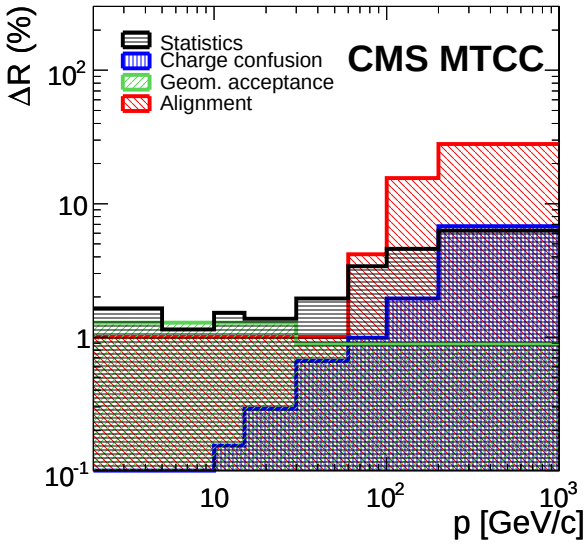

Figure 2.13: Summary of the individual contributions to the total systematic uncertainty, expressed as a function of the measured muon momentum. The statistical error is also shown for comparison.

the charge ratio is consistent with being independent of the muon momentum in the considered momentum range. Under this assumption, the mean value of the charge ratio, integrated over the muon momentum, is

$$\langle R^{\circ} \rangle = 1.266 \pm 0.008\,(\text{stat.}) \pm 0.026\,(\text{syst.})$$

This value is obtained combining the charge ratio measurement at the various momentum bins, taking into account the statistical weights and considering the systematic uncertainties are fully correlated bin by bin. The mean value and its uncertainties are dominated by the measurements at low momentum, below $p \simeq 100$ GeV/c, those at high p being largely dominated by the systematic uncertainty (Figure 2.13). This result is consistent with the value obtained in [1], supporting the robustness of the analysis presented here.

In order to compare the CMS results with the measurements from other experiments, the charge ratio is expressed in terms of the muon momentum *before entering CMS*, referred to as the *true* muon momentum. For that, a mapping of the measured into the true muon momentum is performed using simulated events. The overall effect of this correction is an almost constant momentum increase of about 7 GeV/c, having a negligible impact in the charge ratio measurement.

The CMS result nicely compares to those from the most precise experiments [43, 44], as is shown in Figure 2.15.

$\langle p \rangle$	$\langle p^{\circ} \rangle$	N_{μ^+}	N_{μ^-}	R	R°	ΔR°_{stat}	ΔR°_{syst}	ΔR°_{total}
3.95	12.60	8 375	6 669	1.256	1.259	0.020	0.020	0.029
7.29	15.02	17 179	13 781	1.247	1.252	0.014	0.020	0.025
12.29	18.64	9 767	7 744	1.261	1.268	0.019	0.021	0.028
20.98	24.95	12 012	9 462	1.270	1.281	0.017	0.021	0.027
41.16	39.58	6 040	4 663	1.295	1.318	0.025	0.019	0.032
76.14	64.95	1 920	1 568	1.224	1.253	0.042	0.054	0.068
135.11	107.72	1 043	870	1.199	1.249	0.055	0.188	0.196
354.29	266.67	516	497	1.038	1.136	0.065	0.299	0.306

Table 2.3: Numbers of positive and negative muons selected ($N_{\mu^{\pm}}$), measurement of the charge ratio (R) and measurement of the true charge ratio (R°), using CMS data, in various bins of the measured (p) and *true* (p°) muon momentum, along with the statistical (ΔR°_{stat}) and systematic (ΔR°_{syst}) uncertainties. The total error (ΔR°_{total}) in each bin, calculated as the quadratic sum of the statistical and systematic error, is also shown.

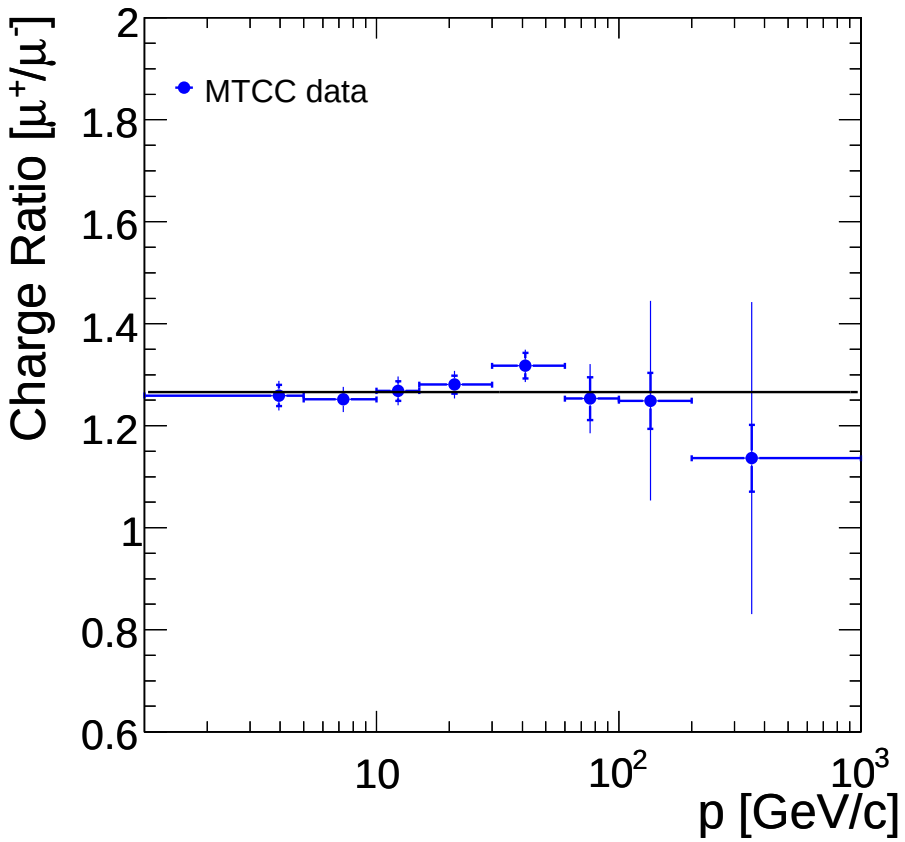

Figure 2.14: Muon charge ratio, R°, as a function of the measured muon momentum in CMS. The thick bars correspond to the statistical error and the thin bars are the systematic errors. The line represents the mean value of the charge ratio, integrated over the muon momentum.

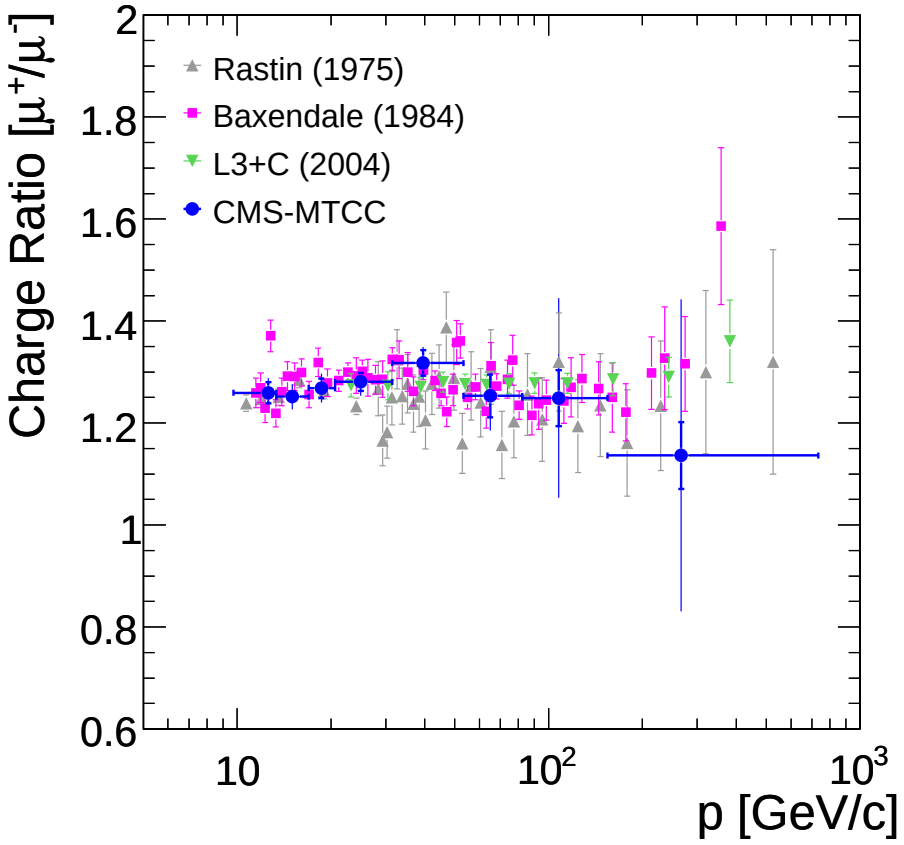

Figure 2.15: Muon charge ratio measured by CMS (blue dots) with statistical (thick bars) and systematic errors (thin bars), together with results from other experiments (other colours).

2.5 Conclusions

We have measured the ratio of positive- to negative-charge cosmic muons, as a function of the muon momentum, using data collected by the CMS experiment at the *Magnet Test and Cosmic Challenge* (MTCC). The analysis has been performed in an environment, CMS and Grid wise, similar to that designed for the analysis of the data coming from proton-proton collisions at LHC, using standard CMS reconstruction software, data distribution and job submission tools. Thanks to this analysis, we have unraveled important issues concerning both the alignment constants of the muon detector and the reconstruction code of CMS. While physics studies were not among the goals of the MTCC, we have succeeded to obtain a result of good quality, also accounting for the most important systematic uncertainties that affect the measurement. The cosmic muon charge ratio is found to be independent of the muon momentum in the considered range, which is in good agreement with previous measurements within the experimental uncertainties. This is the first measurement of a physical quantity performed by the CMS experiment.

Chapter 3

Discovery potential of the Standard Model Higgs boson in the $H \rightarrow ZZ^{(*)} \rightarrow 4\mu$ decay channel

One of the fundamental goals of the CMS experiment is the discovery of the Higgs boson and the study of its properties, despite its very small production cross section at LHC, up to nine orders of magnitude smaller, compared to that of the background processes. The design of CMS allows for its detection and the measurement of its properties.

This chapter presents the CMS discovery potential as well as the search strategy for the Standard Model Higgs boson, using the $H \rightarrow ZZ^{(*)} \rightarrow 4\mu$ decay channel. The analysis, cut-based and independent of the Higgs boson mass, m_H, exploits the relatively narrow shape of the invariant mass distribution of the four muons in the final state. Using the log-likelihood ratio statistical method, the expected significance of the Higgs boson signal is determined as a function of m_H, for integrated luminosities of 10 fb^{-1} and 30 fb^{-1}. Systematic uncertainties on the normalization of the signal and background expectations are taken into account in the analysis. These are mainly due to experimental effects and theoretical uncertainties. The search strategy for the Higgs boson is based on using confidence levels that characterize either the signal plus background or background likeliness of the data.

3.1 Production and decay of the Standard Model Higgs boson

3.1.1 Production mechanisms

The gauge couplings that govern the Higgs boson interactions are proportional to the masses of the particles it couples to, making the Higgs boson to be dominantly produced in association with massive particles (including loop-induced processes).

The most relevant processes contributing to the Higgs boson production at LHC (Figure 3.1) are: $gg \rightarrow H$ (gluon fusion through heavy quark loop), $qq \rightarrow VVqq \rightarrow qqH$ (weak vector boson, W/Z, fusion), $gg \rightarrow t\bar{t}H$ ($t\bar{t}$ associated production) and $q\bar{q} \rightarrow V \rightarrow VH$ (weak vector boson associated production).

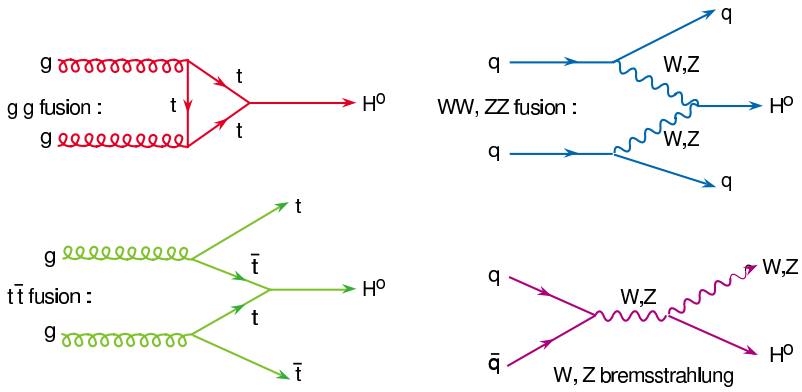

Figure 3.1: Feynman diagrams of the main Higgs boson production mechanisms at tree level in proton-proton collisions. From left to right and from top to bottom: gluon fusion, vector boson (W/Z) fusion; $t\bar{t}$ fusion; W/Z associated production.

The relative importance of these processes depends on the Higgs boson mass, as can be appreciated in Figure 3.2 (left) [35, 55], where the corresponding cross-sections are shown as a function of m_H. Due to the large size of the top Yukawa couplings and the gluon densities, the gluon fusion, $pp \rightarrow gg \rightarrow H$, is the dominant process in the entire mass range, and only for very high m_H values the weak boson fusion process contributes in a significant way. In the analysis presented in this thesis, the Next-to-Leading-Order (NLO) cross sections and branching ratios (decay partial widths) for the Higgs boson are calculated with the programs HDECAY and HIGLU [55], as well as the NLO cross sections for the background processes, when available. QCD NLO corrections significantly increase the Higgs boson production cross section, 50% to 100%, and Next-to-Next-to-Leading-Order (NNLO) corrections are of the order of 20%.

3.1.2 Decay channels

The Higgs boson decays to the heaviest particle pair allowed by energy-momentum conservation, its decay partial widths depending on m_H (Figure 3.2, right [35, 55]). The discovery potential of the Higgs particle at LHC essentially depends on the number of events of a given decay mode and the abundance of Standard Model processes with a similar topology (background). For $m_H \leq 135$ GeV/c^2, the Higgs boson mainly decays into $b\bar{b}$ and $\tau^+\tau^-$ pairs with branching ratios of about 85% and 8% respectively. The QCD jet background is so high at LHC that will make almost impossible the discovery of the Higgs boson via these two decay modes. While the decays into $c\bar{c}$ and gluon pairs (the latter mediated by top and bottom quark loops) accumulate a branching ratio of about 10%, they do not play a relevant role at LHC, due to the huge QCD background level.

The most promising channel in this mass range is the decay into photon pairs, $H \rightarrow \gamma\gamma$, which is mediated by W boson, top and bottom quark loops. In spite of the very low branching ratio ($\sim 10^{-3}$), this decay mode has a very clean signature. The CMS ECAL has the excellent angular

and energy resolutions required to detect this signal and to reject the large QCD background induced by the mesons $\pi^0 \to \gamma\gamma$ decays.

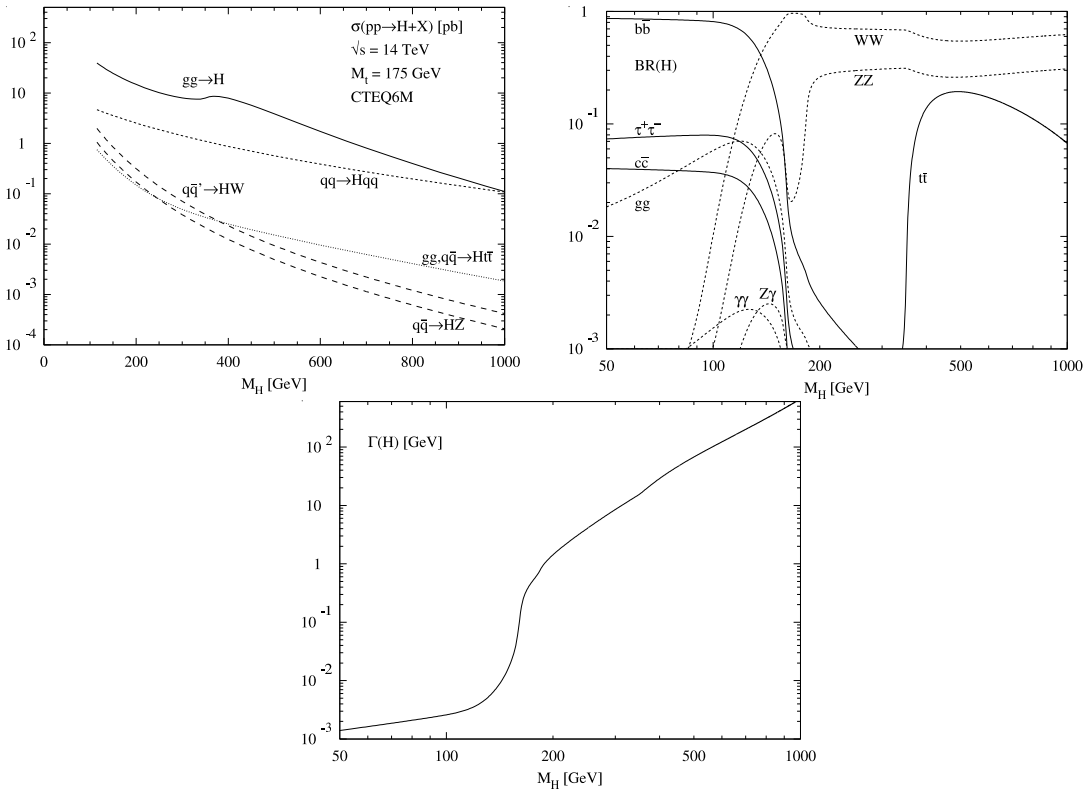

Figure 3.2: (Left) Higgs boson production cross sections at the LHC for the various production mechanisms as a function of the Higgs boson mass. The full QCD-corrected results for the gluon fusion gg → H, vector-boson fusion qq → VVqq → qqH, vector-boson bremsstrahlung $q\bar{q} \to V \to VH$, and associated production $gg, qq \to t\bar{t}H$ are shown. (Right) Branching ratios (partial widths) of the dominant decay modes of the SM Higgs particle. (Bottom) Total decay width (in GeV/c^2) of the SM Higgs boson as a function of its mass.

For Higgs boson masses above 135 GeV/c^2 the main decay modes are those into WW and ZZ. These decay modes dominate over the decay into $t\bar{t}$, whose branching ratio does not exceed $\sim 20\%$ for $m_H > 2m_W$. For $m_H < 2m_{W,Z}$ (below the kinematical threshold), one of the vector bosons is off-shell (the mass of the virtual W, Z boson is lower than $m_{W,Z}$). Both W and Z bosons decay mainly into quarks, giving rise to purely hadronic final states. These events are still difficult to detect over the large QCD background. The W and Z decays into leptons are cleaner and easier to isolate from other Standard Model processes.

The process $H \to WW^* \to \ell\nu\ell\nu$ is the main Higgs boson discovery decay channel in CMS for $m_H \sim 2m_W$ (150 GeV/$c^2 \leq m_H \leq$ 170 GeV/c^2). Several dedicated studies have established the CMS discovery potential of the Higgs boson using this channel [35, 56].

The process $H \to ZZ \to 4\ell$ (where $\ell = e, \mu$) is a very important discovery channel, since it

has a very clean signature with relatively small backgrounds for a large range of Higgs boson masses. The channels $\mathrm{H} \rightarrow \mathrm{ZZ}^{(*)} \rightarrow 4\mathrm{e}$ and $2\mathrm{e}2\mu$ have been studied in detail elsewhere [35, 57]. The process $\mathrm{H} \rightarrow \mathrm{ZZ}^{(*)} \rightarrow 4\mu$ is considered the golden discovery channel in CMS and has been the subject of my research work. It is described in detail in the rest of this chapter and in Chapter 4.

The total decay width of the Higgs boson, shown in Figure 3.2 (bottom) [35,55] as a function of m_{H}, is one of its intrinsic properties and its experimental determination is crucial to tell the Standard Model Higgs boson from other signals of new physics predicted by other models.

3.2 The golden channel: $\mathrm{H} \rightarrow \mathrm{ZZ}^{(*)} \rightarrow 4\mu$

The process $\mathrm{H} \rightarrow \mathrm{ZZ}^{(*)} \rightarrow \mu^+\mu^-\mu^+\mu^-$ has particular interest for the discovery of the Higgs boson as it provides clean events, with four high-p_{T} isolated muons with a narrow invariant mass distribution, while it is affected by a reasonably low amount of non-resonant ZZ background. It is the most sensitive channel, together with the other four-lepton final states, within a wide range of Higgs-boson masses. The Higgs boson decay into Z boson pairs, subsequently decaying into four muons, still has a significant branching ratio in the mass range $130\ \mathrm{GeV}/c^2 \leq m_{\mathrm{H}} \leq 150\ \mathrm{GeV}/c^2$, which enhances the importance of this channel for the discovery of a low mass Higgs boson.

In the following sections we outline a complete analysis strategy for discovering the Standard Model Higgs boson in the $\mathrm{H} \rightarrow \mathrm{ZZ}^{(*)} \rightarrow 4\mu$ channel. The explored range of Higgs boson masses is $115\ \mathrm{GeV}/c^2 - 600\ \mathrm{GeV}/c^2$.

Previous studies on the search for the Standard Model Higgs boson in this decay channel are described in [58, 59]. Other analyses establishing the CMS discovery potential of the Higgs boson using the decay channels $\mathrm{H} \rightarrow \mathrm{ZZ}^{(*)} \rightarrow \mathrm{e}^+\mathrm{e}^-\mathrm{e}^+\mathrm{e}^-$ and $\mathrm{e}^+\mathrm{e}^-\mu^+\mu^-$ are found in [57].

The signal process in this analysis is the production of a Higgs boson decaying into a pair of Z bosons, which subsequently decay into two muon pairs. The small number of cases in which one muon pair comes from the decay of a τ pair is also considered in the analysis. Other Higgs boson decays with four muons in the final state originating, for instance, from $\mathrm{Z} \rightarrow \mathrm{q\bar{q}} \rightarrow \mu^+\mu^- + \mathrm{X}$, are not considered, as the efficiency of the selection cuts for those events is close to zero.

The main background processes that also yield four muons in the final state are $\mathrm{pp} \rightarrow \mathrm{t\bar{t}}$, with $\mathrm{t} \rightarrow \mathrm{Wb} \rightarrow \mu\nu\mathrm{b}$; $\mathrm{pp} \rightarrow (\mathrm{Z}^{(*)}/\gamma^*)\mathrm{b\bar{b}}$ and $\mathrm{pp} \rightarrow (\mathrm{Z}^{(*)}/\gamma^*)(\mathrm{Z}^{(*)}/\gamma^*)$, with $\mathrm{Z}^{(*)}/\gamma^* \rightarrow 2\mu$ and the b-quark decaying semi-leptonically. These three backgrounds will be hereafter referred to as $\mathrm{t\bar{t}}$, $\mathrm{Zb\bar{b}}$, and ZZ, respectively. Other background candidates with significantly lower cross sections times branching ratio ($\mathrm{b\bar{b}b\bar{b}}$, $\mathrm{b\bar{b}c\bar{c}}$, $\mathrm{c\bar{c}c\bar{c}}$, single-top, $\mathrm{Zc\bar{c}}$, $\mathrm{Wb\bar{b}}$, $\mathrm{Wc\bar{c}}$, fake and π/K decay muons in QCD), as well as the interference between the main backgrounds and the Higgs boson signal, are negligible and therefore not considered in this analysis.

3.3 Simulated data samples

Both signal and background event samples are generated at the LO approximation, and NLO production cross-sections, computed using different methods, are used for their normalization.

Only events with two pairs of opposite-charged muons with pseudo-rapidity $|\eta| < 2.4$ and $p_{\mathrm{T}} > 3\ \mathrm{GeV}/c$ are considered in the generation, since muons outside these limits are not recon-

structed by CMS. Events where the invariant mass of the muon pairs coming from Z bosons is smaller than 5 GeV/c^2 are rejected.

The $H \to ZZ^{(*)} \to 4\mu$ sample is generated with the PYTHIA [60] program, interfaced with CMKIN [61], considering Higgs production through gluon and weak boson fusion processes at LO, and forcing the decay of the Higgs into a pair of Z bosons. Only leptonic decay modes of the Z bosons are included in the simulation. QED radiation from the final state muons is modelled with PHOTOS [62]. The mass of the generated Z bosons is restricted to be in the range from 5 GeV/c^2 to 150 GeV/c^2. A set of 18 signal samples are generated for different Higgs boson masses, ranging from 115 GeV/c^2 to 600 GeV/c^2.

The generated signal samples are normalized to the value of the total cross section at NLO [55], which includes all production mechanisms, multiplied by the branching ratios BR($H \to ZZ$) [55] and BR($Z \to \mu^+\mu^-$)^2 [63]. Figure 3.3 shows the cross section times the branching ratio of the process $H \to ZZ^{(*)} \to 4\mu$ as a function of the Higgs boson mass.

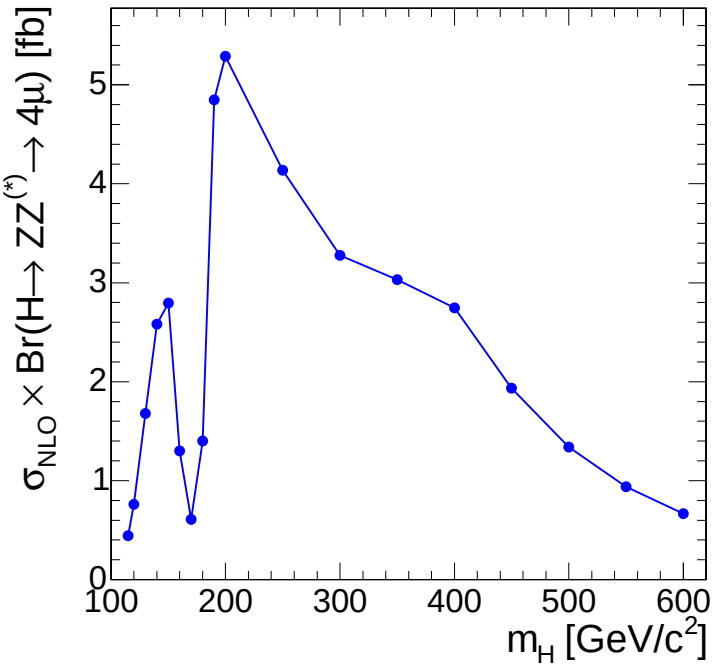

Figure 3.3: Total NLO cross-section times branching ratio for the process $H \to ZZ^{(*)} \to 4\mu$ as a function of the Higgs boson mass. The dots indicate the mass points at which the calculation has been preformed.

A correction factor is applied to the cross section to take into account the presence of two pairs of identical particles in the final state [64]. This correction factor has been calculated with CompHEP [65] and amounts to 1.130 ± 0.006 for $m_H = 115$ GeV/c^2 smoothly decreasing to one for $m_H \sim 2m_Z$.

The $t\bar{t}$ sample has been generated using PYTHIA including the LO processes $gg \to t\bar{t}$ and

$\mathrm{q\bar{q}} \to \mathrm{t\bar{t}}$. Only the top decays $\mathrm{t} \to \mathrm{Wb} \to \ell\nu\mathrm{b}$ are considered. The corresponding total NLO cross-section is $\sigma(\mathrm{pp} \to \mathrm{t\bar{t}}) \cdot BR(W \to \ell\nu)^2$, where $\sigma(\mathrm{pp} \to \mathrm{t\bar{t}}) = 840$ pb is taken from [66] and the branching ratio $BR(W \to \ell\nu) = 0.320$ [63].

The $\mathrm{Zb\bar{b}}$ background originates either from gluons or quarks in the initial state. This sample has been generated with CompHEP, including the matrix element generator for both initial states decaying into $\mu^+\mu^-\mathrm{b\bar{b}}$. No restrictions have been applied on the decay modes of the b and the $\bar{\mathrm{b}}$ quarks. CompHEP has been interfaced with PYTHIA for showering and hadronization. The NLO cross section, 278.4 pb, is obtained scaling the LO value provided by CompHEP with a K-factor, $\mathrm{K_{NLO}} = 2.4 \pm 0.3$, calculated with MCFM [67].

The ZZ background also originates either from gluons or quarks in the initial state. However, neither PYTHIA nor CompHep includes the process $\mathrm{gg} \to (\mathrm{Z}^{(*)}/\gamma^*)(\mathrm{Z}^{(*)}/\gamma^*)$, therefore only the $\mathrm{q\bar{q}}$ contribution is generated. Moreover, recent studies [68] have shown that the s-channel contribution to this process cannot be neglected as it may add up to 10% for low four-muon masses. Hence, the generation at LO is done using CompHEP as it includes both, t- and s-channel diagrams. The LO cross section of the process with both Z bosons decaying directly into muons is 113 fb. The processes in which one Z boson decays into a τ-lepton pair, subsequently decaying into a muon pair, are also considered in the analysis. This channel has a LO cross section of 4.7 fb.

The scaling to the NLO cross section for the ZZ background is done by means of a K factor, $\mathrm{K_{NLO}}(\mathrm{m}_{4\mu})$, that depends on the invariant mass of the four-muon system [69]. It is evaluated for the t-channel contribution with MCFM and MadGraph [70]. The mean value of $\mathrm{K_{NLO}}(\mathrm{m}_{4\mu})$, averaged over the four-muon mass range from 30 GeV/c^2 to 700 GeV/c^2, is 1.35. The same factor is used for the s-channel. The maximum relative error due to considering a unique K factor for both s- and t-channels amounts to 1.4%.

The gluon fusion contribution to the ZZ cross section is on average 20% of the LO quark-antiquark annihilation term [64], depending on the four-muon mass, with variations around $\pm$8% within the four-muon mass range 100 GeV/c^2 to 240 GeV/c^2. More recent calculations performed with TopREX [71] confirm this number, with the caveat that TopREX does not include γ^* contributions and the Z boson is restricted to be on-shell. The NLO ZZ cross section is rescaled to account for this contribution.

Events with four muons in the final state are fully simulated and reconstructed using the latest available at the moment official CMS simulation, OSCAR [72], and reconstruction, ORCA [73], software. Pile-up events corresponding to an instantaneous luminosity of 2×10^{33} cm^{-2} s^{-1} are included in the simulations.

3.4 Event Selection

The $\mathrm{H} \to \mathrm{ZZ}^{(*)} \to 4\mu$ signal presents a characteristic topology, which consists of two pairs of opposite-charged muons in the final state. The muons are isolated, have a high transverse momentum, and point to the same primary vertex. The dimuon invariant mass is compatible with the Z-boson mass, depending on the restrictions in the phase space introduced by the Higgs boson mass itself. The four-muon invariant mass accounts for the Higgs boson mass, within the detector resolution.

In $Zb\bar{b}$ and $t\bar{t}$ background events, two of the muons come from secondary vertices and are contained inside b-jets, with relatively low transverse momenta. These muons are clearly distinguishable from those originating in a Higgs particle decay. These backgrounds can be efficiently suppressed by applying high p_{T} and isolation cuts. In addition, the constraint of a dimuon pair to be compatible with the Z boson mass further reduces the $t\bar{t}$ background.

The topology of the ZZ background is quite similar to that of the signal, therefore it is not reduced by high p_{T} and isolation cuts. The four-muon mass distribution of these events is, however, non-resonant, unlike that of the Higgs boson signal.

This analysis uses a unique set of requirements, independent of the Higgs boson mass, which efficiently disentangles signal and background and is robust against slight variations in the cuts. An analysis based on cuts optimized for different four-muon mass values shows that the signal sensitivity does not improve significantly and has the disadvantage of being strongly dependent on the detailed and accurate simulation of the detector response [74].

CMS has been designed and optimized to detect and reconstruct muons. These particles provide a very clean signature and thus a very high trigger efficiency, with an average over 98% for the Level-1 Global Muon Trigger [75]. The inclusive muon triggers based on the selection of a single muon with $p_T > 19$ GeV/c or dimuons with $p_T > 7$ GeV/c assures an efficiency of practically 100% for collecting events with four high-p_{T} muons.

The selection of the $\mathrm{H} \rightarrow \mathrm{ZZ}^{(*)} \rightarrow 4\mu$ candidates requires at least four reconstructed muons within the acceptance of the detector, $p_T > 3$ GeV/c, and $|\eta| < 2.5$. In order to minimize muon reconstruction systematic uncertainties, muons in the barrel detector ($|\eta| < 1.1$) are required to have a transverse momentum $p_T > 7$ GeV/c, while those in the end-cap detector ($|\eta| > 1.1$) must have $p > 13$ GeV/c [76].

The mass of all possible combinations of unlike-charge reconstructed muon pairs is required to be larger than 12 GeV/c^2. This cut eliminates the low mass dimuon resonances, which are not included in the Monte Carlo simulation, and reduces substantially the s-channel contribution from ZZ background [68].

The efficiency of the cuts is shown in Figure 3.4 for the simulated Higgs boson masses and for the background. This efficiency is calculated as the ratio of the number of events surviving each cut to the total number of generated events before the acceptance cuts at generator level are applied. The numbers of signal and background events expected for an integrated luminosity of 30 fb^{-1} are listed in Table 3.1 after each selection cut.

The $\mathrm{H} \rightarrow \mathrm{ZZ}^{(*)}$ decay produces at least one on-shell Z boson. From all the muons in the event, the two unlike-sign muons for which the invariant mass is closest to the Z boson mass, 91.2 GeV/c^2, and the two remaining unlike-sign muons with highest p_{T} are associated to the Higgs boson. The invariant mass of the former muon pair is shown in Figure 3.5 for two Higgs mass hypotheses, 150 GeV/c^2 and 300 GeV/c^2, and for the background after the quality cuts described above. A loose requirement on this variable, 70 GeV/$c^2 < m_{\mu^+\mu^-} < 100$ GeV/c^2, has an efficiency for the signal higher than 90% while it eliminates around 50% of the $t\bar{t}$ contamination (Figure 3.4). The loss in the signal is due to the fact that radiated photons are not taken into account in the reconstruction of the Z-boson invariant mass. The percentage of charge mis-assignment is below 0.1% for muons with p_{T} lower than 500 GeV/c [77].

In the $Zb\bar{b}$ and $t\bar{t}$ background, the two muons coming from b decays have a softer p_{T} spectrum than those of the signal and are not isolated. The other two muons, coming from the decay of

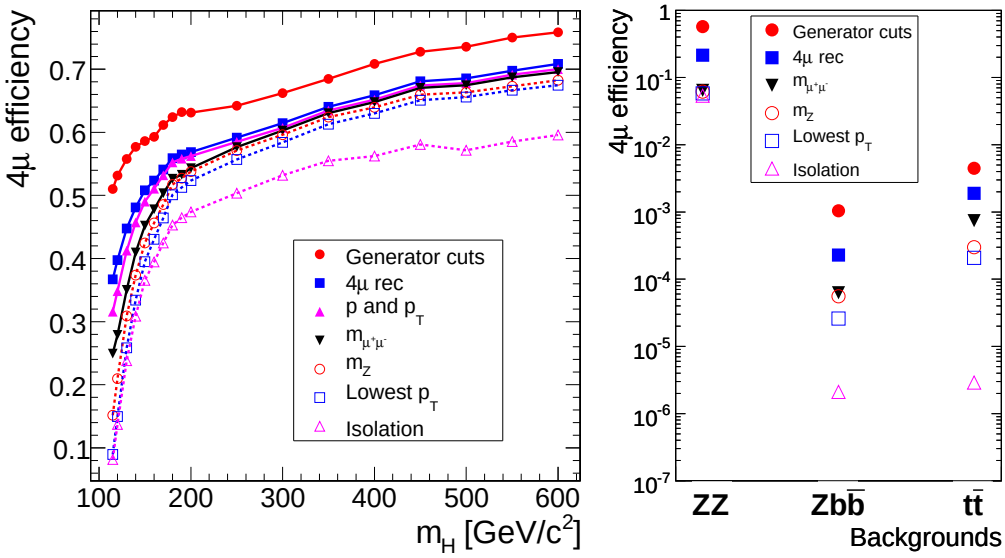

Figure 3.4: (Left) $\mathrm{H} \rightarrow \mathrm{ZZ}^{(*)} \rightarrow 4\mu$ efficiency versus m_{H} for different cuts applied to the event samples: generator acceptance cuts $p_T^{\mathrm{gen}} > 3$ GeV/c and $|\eta^{\mathrm{gen}}| < 2.5$ (red, circles), four muon reconstruction (blue, squares), $p_T > 7$ GeV/c and $p > 13$ GeV/c cuts (pink, triangles), $m_{\mu^+\mu^-} > 12$ GeV/c^2 cut (black, inverse-triangles), on-shell Z boson mass cut (red, open circles), p_{T} cuts (blue, open squares), and muon isolation cuts (pink, open triangles). (Right) Efficiency, for the same cuts, for the background processes $\mathrm{t\bar{t}}$, $\mathrm{Zb\bar{b}}$, and ZZ.

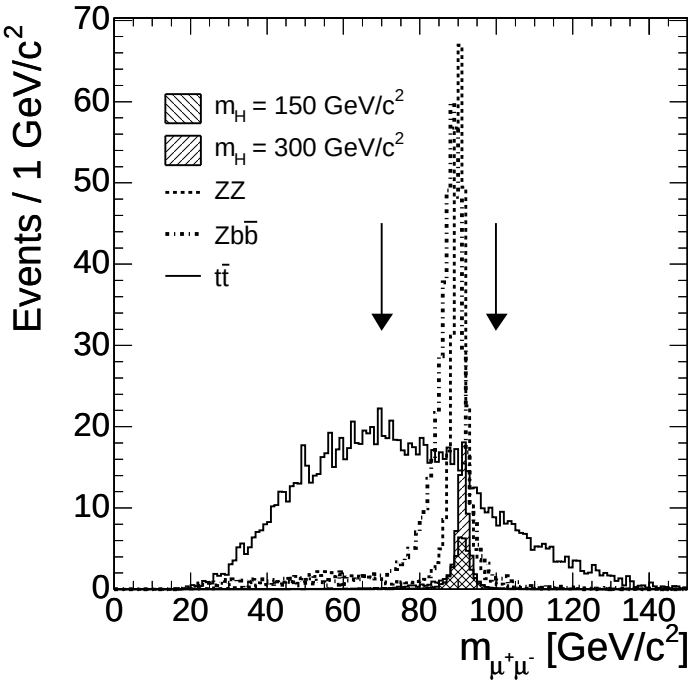

Figure 3.5: Distribution of the dimuon invariant mass, m_Z. The hatched histograms represent the Higgs boson signals of masses 150 GeV/c^2 and 300 GeV/c^2, while the solid, dashed, and dash-dotted lines indicate the contribution from the $t\bar{t}$, ZZ, and $Zb\bar{b}$ backgrounds, respectively. The arrows indicate the position of the cuts.

Process	generator	4μ rec.	p, p_{T}, and $m_{\mu^+\mu^-}$	m_{Z}	lowest p_{T}	isolation
$m_{\mathrm{H}} = 115$	8.3	6.0	4.1	2.5	1.5	1.3
$m_{\mathrm{H}} = 120$	14.5	10.9	7.6	5.7	4.1	3.8
$m_{\mathrm{H}} = 130$	32.9	26.4	20.7	18.2	15.2	14.0
$m_{\mathrm{H}} = 140$	51.1	42.6	36.3	33.1	29.6	27.3
$m_{\mathrm{H}} = 150$	55.2	47.8	42.6	40.0	37.2	34.4
$m_{\mathrm{H}} = 160$	25.6	22.6	20.6	19.7	18.6	17.0
$m_{\mathrm{H}} = 170$	12.2	10.8	10.0	9.7	9.3	8.5
$m_{\mathrm{H}} = 180$	28.4	25.5	24.0	23.6	22.8	20.6
$m_{\mathrm{H}} = 190$	100	89.6	84.5	83.6	81.3	73.7
$m_{\mathrm{H}} = 200$	109	98.4	94.0	93.1	90.6	82.0
$m_{\mathrm{H}} = 250$	87.1	80.2	78.2	77.5	75.5	68.3
$m_{\mathrm{H}} = 300$	71.1	66.0	64.8	64.1	62.8	57.2
$m_{\mathrm{H}} = 350$	68.0	63.6	62.6	62.0	60.9	55.1
$m_{\mathrm{H}} = 400$	63.7	59.2	58.3	57.5	56.6	50.6
$m_{\mathrm{H}} = 450$	46.2	43.3	42.6	41.9	41.4	36.9
$m_{\mathrm{H}} = 500$	32.3	30.1	29.6	29.1	28.8	25.1
$m_{\mathrm{H}} = 550$	23.1	21.5	21.1	20.7	20.5	18.0
$m_{\mathrm{H}} = 600$	16.6	15.5	15.2	14.9	14.7	13.0
ZZ	2766	1036	312	298	281	259
$\mathrm{Zb\bar{b}}$	8689	1907	531	467	217	17.8
$\mathrm{t\bar{t}}$	6961	2945	1157	465	325	4.5

Table 3.1: Numbers of signal and background events expected for an integrated luminosity of 30 fb^{-1} after each selection cut. For the signal, the Higgs boson mass is indicated in GeV/c^2 in the first column.

a Z boson, are harder and isolated, like the four muons of the signal and the ZZ background.

Figure 3.6 shows the p_{T} spectrum of the two muons of lowest p_{T} for two Higgs boson signals, 150 GeV/c^2 and 300 GeV/c^2, and for the background. Cuts of 12 GeV/c and 8 GeV/c are set on the p_{T} of the two lowest-p_{T} muons. The p_{T} of the two highest-p_{T} muons must be larger than 15 GeV/c. The latter cut has little effect on either the signal or the background, but is considered useful for eliminating unexpected background in real data. The efficiency of the p_{T} cuts in the signal is close to 90% while it suppresses around 50% of the remaining $\mathrm{Zb\bar{b}}$ events, 40% of the $\mathrm{t\bar{t}}$ events and about 10% of the ZZ background (Figure 3.4).

Isolation is defined as the amount of transverse energy in the calorimeter (calorimeter isolation), or the sum of the transverse momentum of the tracks reconstructed in the tracker (tracker isolation), inside a cone in η-ϕ space with a radius $R \equiv \sqrt{(\Delta\eta)^2 + (\Delta\phi)^2}$ defined with respect to the muon flight direction. Figures 3.7 and 3.8 show the distribution of these isolation variables for the two least isolated muons. Different cone radii and several energy and transverse momentum thresholds have been studied. Those yielding the maximum signal significance are,

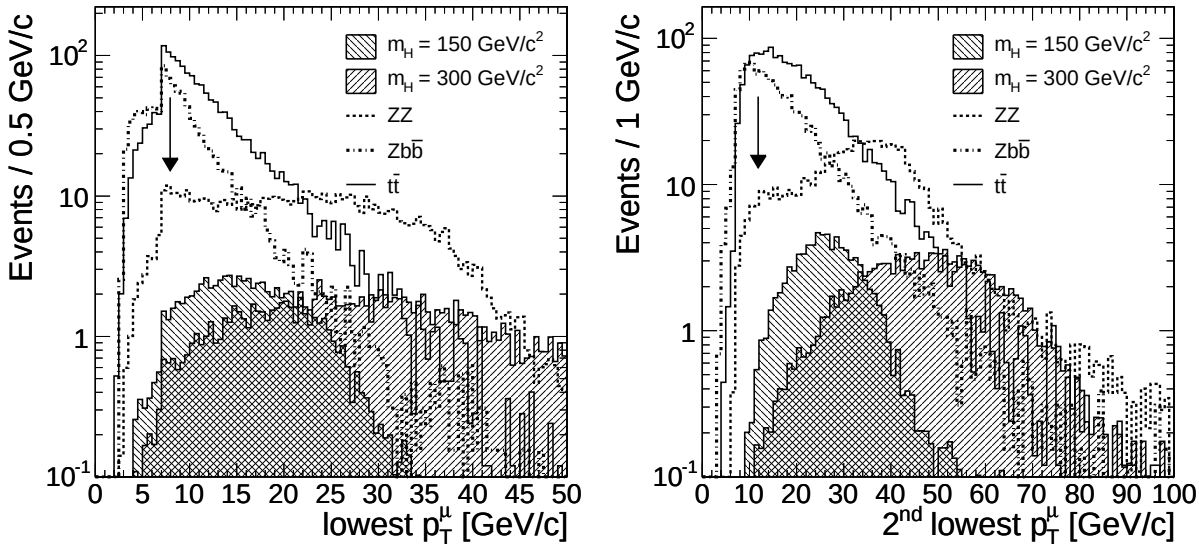

Figure 3.6: Distribution of the transverse momentum of the (left) lowest and (right) 2$^{\text{nd}}$ lowest p_{T} muon. The hatched histograms represent the Higgs boson signals of masses 150 GeV/c^2 and 300 GeV/c^2, while the solid, dashed, and dash-dotted lines indicate the contribution from the $\text{t}\bar{\text{t}}$, ZZ, and $\text{Zb}\bar{\text{b}}$ backgrounds, respectively. The arrows indicate the position of the cuts.

for calorimeter isolation, a cone radius of 0.24 rad and energy thresholds of 5 GeV and 9 GeV, while for tracker isolation a cone radius of 0.20 rad and p_{T} thresholds of 2.5 GeV/c and 4 GeV/c. Although a requirement on the isolation of the two most isolated muons does not increase the signal significance, following the same argument as in the case of the p_{T} cuts, a cut on 3.5 GeV and 5 GeV for the calorimeter isolation and 2 GeV/c and 2.5 GeV/c for the tracker isolation is set for the two most isolated muons.

The background rejection factors of the whole selection procedure are 99.9% for $\text{Zb}\bar{\text{b}}$ and $\text{t}\bar{\text{t}}$, and 90% for ZZ (Figure 3.4). While the dominant remaining background comes from ZZ events, the $\text{Zb}\bar{\text{b}}$ contribution is still visible for four-muon masses below 180 GeV/c^2. The $\text{t}\bar{\text{t}}$ background is reduced to negligible levels. The four-muon mass distribution of signal and background events that survive the selection cuts is displayed in Figure 3.9 for an integrated luminosity of 30 fb^{-1}.

Some other possible discriminating variables have been studied. Among them it is worth mentioning the χ^2 of the fit to a common vertex of all four muons in the event, the impact parameters of the muons, angular distributions of the muons, etc. Unfortunately, additional requirements on these variables do not increase the signal sensitivity. The investigated secondary vertex cuts have a smaller background rejection than the isolation cuts and would introduce additional detector systematic uncertainties.

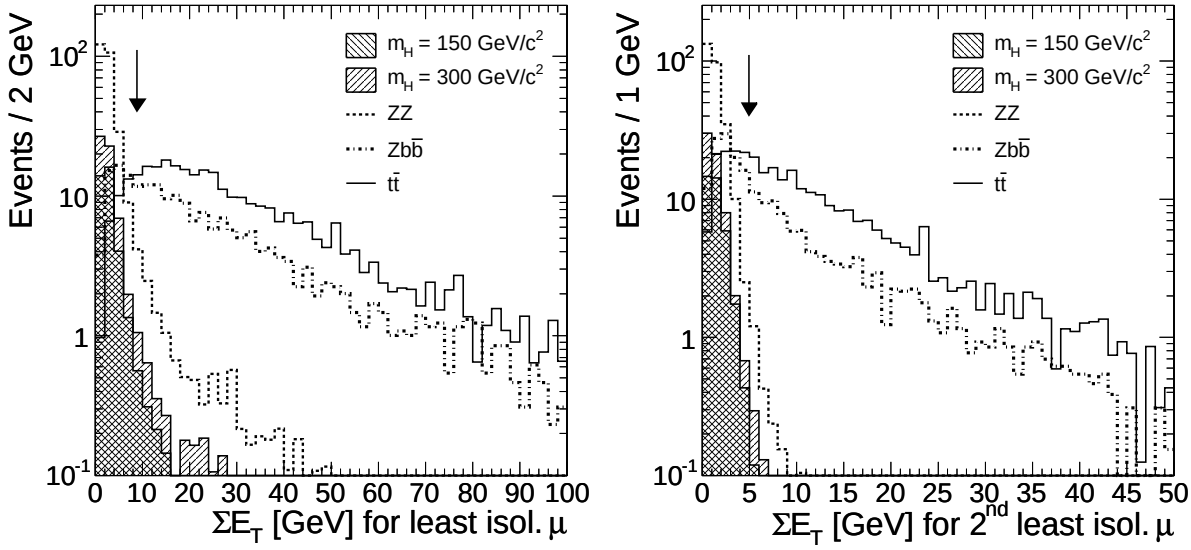

Figure 3.7: Calorimeter muon isolation, calculated as $\sum E_T$ inside a cone around the muon, for the (left) least and (right) 2$^{\mathrm{nd}}$ least isolated muon in the event. The hatched histograms represent the Higgs boson signals of masses 150 GeV/c^2 and 300 GeV/c^2, while the solid, dashed, and dash-dotted lines indicate the contribution from the $\mathrm{t\bar{t}}$, ZZ, and $\mathrm{Zb\bar{b}}$ backgrounds, respectively. The arrows indicate the position of the cuts.

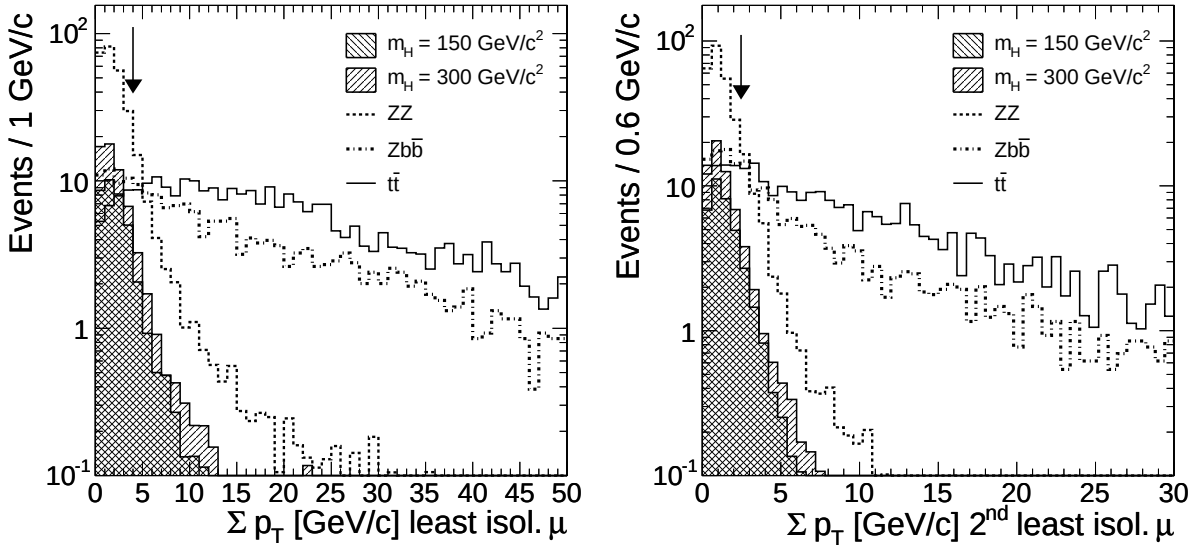

Figure 3.8: Tracker muon isolation, calculated as $\sum p_T$ inside a cone around the muon, for the (left) least and (right) 2$^{\text{nd}}$ least isolated muon in the event. The hatched histograms represent the Higgs boson signals of masses 150 GeV/c^2 and 300 GeV/c^2, while the solid, dashed, and dash-dotted lines indicate the contribution from the $t\bar{t}$, ZZ, and $Zb\bar{b}$ backgrounds, respectively. The arrows indicate the position of the cuts.

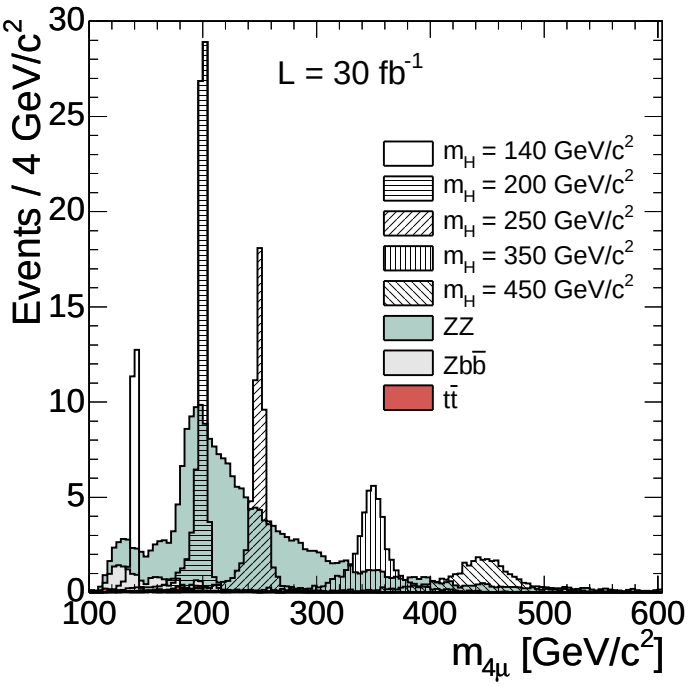

Figure 3.9: Reconstructed four-muon invariant mass distribution, for an integrated luminosity of 30 fb^{-1}, for background (shaded histograms) and several Higgs signals (hatched), after selection criteria have been applied. The $\mathrm{t\bar{t}}$ contribution, hardly visible, is around 0.25 events per bin in the mass range 100 GeV/$c^2$to 250 GeV/c^2.

3.5 Statistical Analysis

In order to estimate the statistical significance of the signal, the log-likelihood ratio statistical method [18,78] is used. The distribution to discriminate signal and background is the four-muon invariant mass (Figure 3.9). This distribution, for each Higgs boson mass hypothesis and for the background, is used to calculate the likelihood ratio, Q, as a function of m_{H}. The function Q is the ratio of the probability of observing the data in the presence of both the expected signal and the expected background, *signal plus background* hypothesis, to the probability of observing the data in the presence of only the expected background, *background-only* hypothesis. The log-likelihood ratio, used to evaluate the compatibility of the data with either hypothesis, is defined as

$$-2\ln Q \equiv 2\sum_{i=1}^{N}\left[s_i - n_i \ln\left(1+\frac{s_i}{b_i}\right)\right]$$

where the sum runs over the N bins of the final discriminant distribution. The numbers of expected signal, expected background, and observed events in the i^{th} bin are denoted by s_i, b_i, and n_i, respectively. The $-2\ln Q$ estimator is sensitive to both the normalization and the shape of the discriminant. Each event in the sum has a weight $\ln(1+s/b)$ which depends on the signal-to-background ratio, s/b, in the bin where it is found, which in turn depends on the m_{H} hypothesis.

In this method, each bin of the discriminant distribution is treated as a single Poisson counting experiment. Figure 3.10 shows the normalized $-2\ln Q$ distributions resulting from large numbers of pseudo-experiments according to either the signal-plus-background or the background-only four-muon mass spectra for Higgs boson signals of 140 GeV/c^2 and 250 GeV/c^2 masses. The numbers of events of the pseudo-experiments are those expected for integrated luminosities of 10 fb^{-1} and 30 fb^{-1}. The difference in the overlap of the shapes for the two hypotheses, background only and signal plus background, evidences the higher sensitivity at larger integrated luminosities, as well as for $m_{\mathrm{H}} = 250$ GeV/c^2 as compared to $m_{\mathrm{H}} = 140$ GeV/c^2. The outcome of a real experiment would appear in those graphs as a vertical line corresponding to the single $-2\ln Q$ value for that particular observation, eventually compatible with one of the two hypotheses.

The discovery potential of the analysis is quantified in terms of the statistical significance, S_L, of the Higgs boson signal in the presence of background. In the log-likelihood method, the significance estimator is obtained from the mean value of the $\ln Q$ distribution for the signal plus background hypothesis for a given m_{H} (Figure 3.10):

$$S_L = \sqrt{< 2\ln Q >}$$

The significance estimator squared is proportional to the total number of signal events, $\sum_{i=1}^{N} s_i$, and hence to the integrated luminosity. Figure 3.11 (left) displays the statistical significance of the Higgs boson search analysis, as a function of m_{H}, for integrated luminosities of 10 fb^{-1} and 30 fb^{-1}. This graph supports the potential of the $\mathrm{H} \to \mathrm{ZZ}^{(*)} \to 4\mu$ channel for discovering the Higgs boson in a wide range of masses for a relatively low integrated luminosity, about 10 fb^{-1}.

Systematic uncertainties on the normalization of the signal and background expectations arise mainly from detector effects and from the uncertainty of the theoretical predictions of the

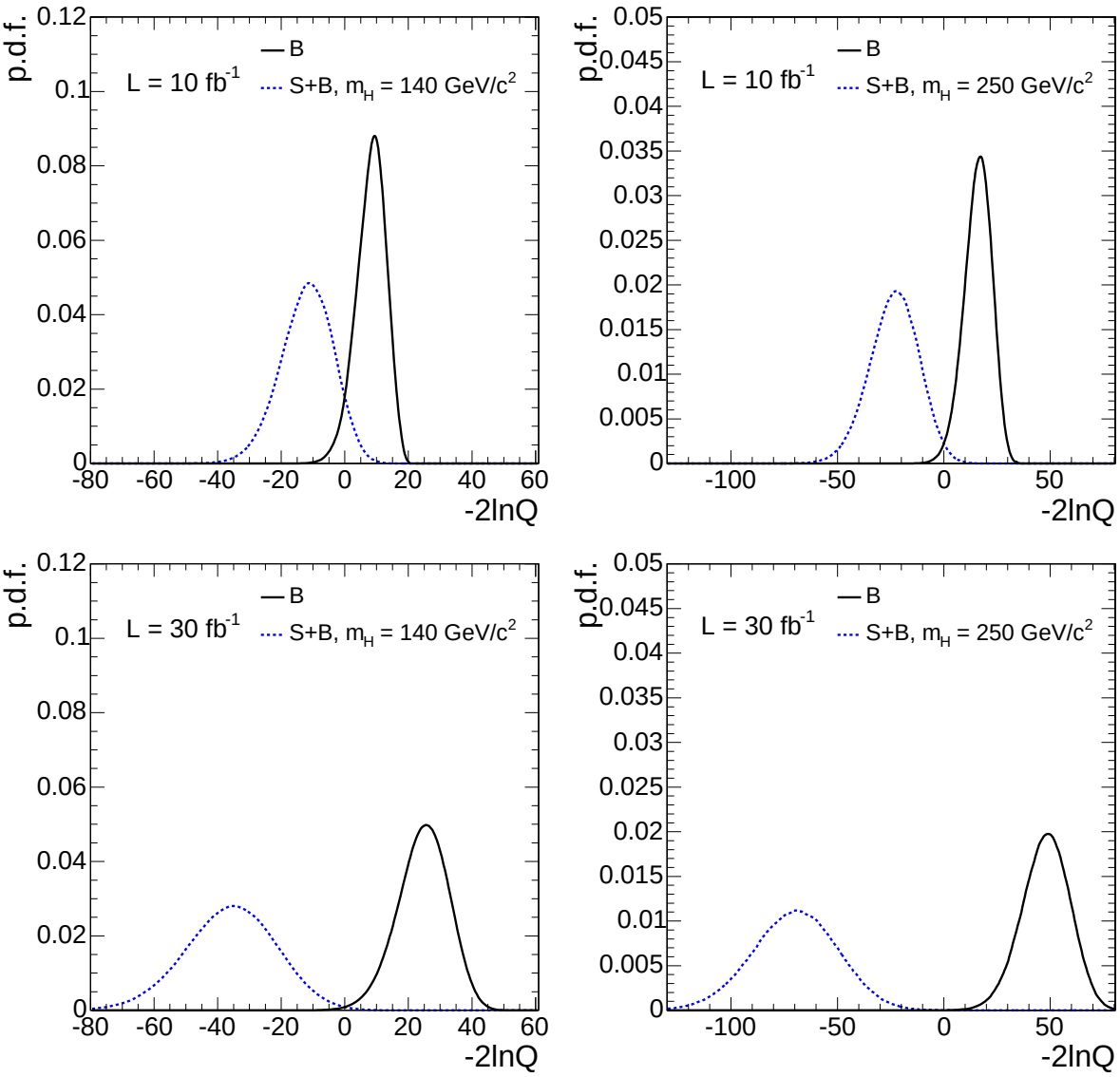

Figure 3.10: Probability density functions of $-2\ln Q$ for the background (solid) and signal plus background (dashed line) hypotheses for Higgs boson signals of $m_{\mathrm{H}} = 140$ GeV/c^2 (left) and 250 GeV/c^2 (right), for integrated luminosities of 10 fb^{-1} (top) and 30 fb^{-1} (bottom).

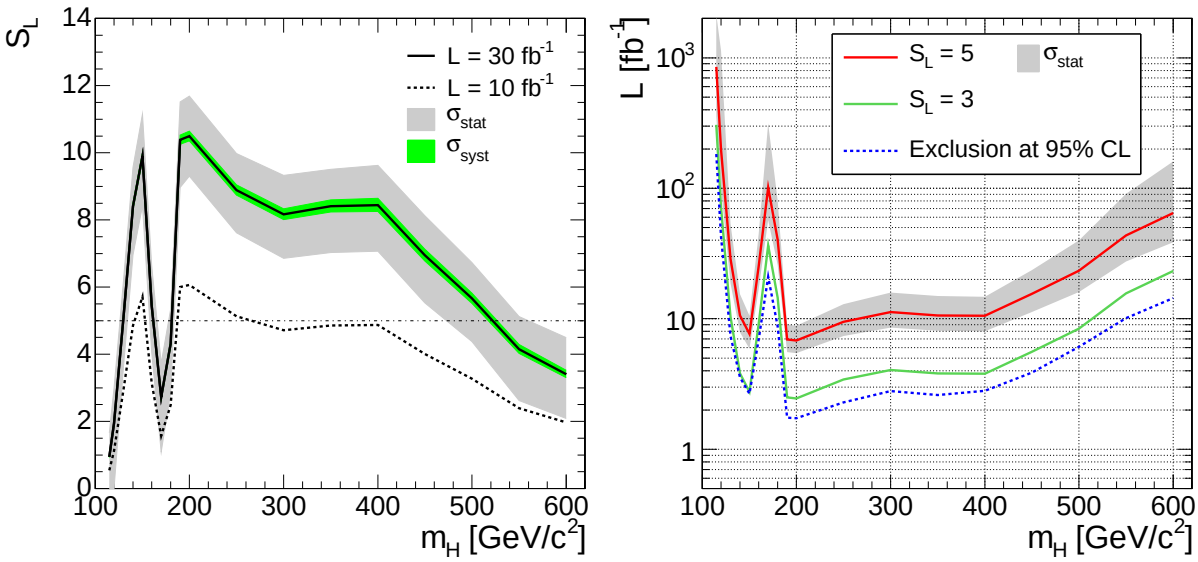

Figure 3.11: (Left) Statistical significance of the signal, S_L, as a function of the Higgs boson mass for integrated luminosities of 10 fb^{-1} and 30 fb^{-1}. The effect of the systematic uncertainties is shown as the shaded area. (Right) Integrated luminosity required to achieve a statistical significance of three (green) and five (red) standard deviations, as a function of the Higgs mass. The integrated luminosity required for excluding a Higgs boson signal at the 95% C.L. in a background-only experiment is also displayed (dashed). The light shaded area represents the statistical 1σ band on the significance (left) and on the integrated luminosity required for $S_L = 5$ (right).

signal and background cross sections. The uncertainties on the PDF (parton density function) and the QCD scale at NLO [79] have a slight dependence on the four-muon mass, varying from 1% to 6% in the mass range from 115 GeV/c^2 to 600 GeV/c^2. The uncertainty on the luminosity measurement is expected to be 5% for the first 10 fb^{-1} and 3% for 30 fb^{-1}. Muon reconstruction and isolation efficiencies are expected to be known within 2%, estimated from data [76]. The systematic uncertainty on the muon trigger efficiency and on the muon p_{T} resolution and scale are found to be negligible. The combined systematic uncertainty varies from 4% to 9%, for masses in the range from 115 GeV/c^2 to 600 GeV/c^2. The effect of including these systematic uncertainties in the calculation of S_L, also shown in Figure 3.11 (left), is well below the statistical uncertainty, $\Delta S_L \simeq 1$ to 1.6.

In a real experiment, a signal-like excess of observed events is considered to be at the discovery level when the probability for a fluctuation of the background to produce such an excess is less than 2.85×10^{-7}, which corresponds to a deviation of over 5σ on the positive tail of a Gaussian distribution. The relation between the number of standard deviations and the significance estimator can only be established if the Gaussian-like behavior is guaranteed, which does not happen in the low statistics limit.

Figure 3.11 (right) depicts the integrated luminosity required to reach a statistical significance of the signal of 3σ and 5σ, as a function of m_{H}. The signal significance is very close to 5σ, for an integrated luminosity of 10 fb^{-1}, for masses around 140 GeV/c^2 and between 180 GeV/c^2 and 400 GeV/c^2. The expected integrated luminosity required to exclude the signal at the 95% confidence level in a background-only experiment is also shown as a function of m_{H}.

Search Strategy

In order to quantify the degree of compatibility of the observed data with any of the two hypotheses, confidence levels are defined using the $-2\ln Q$ probability density functions, *p.d.f.*, for both the background-only and the signal-plus-background hypotheses. These confidence levels are used as statistical estimators.

The integral of the background $-2\ln Q$ probability density function for values larger than the observed one gives the so-called confidence level of the background, CL_b. The presence of a signal can be inferred from the behavior of $1 - \mathrm{CL}_b$ for the background-only hypothesis, which is the probability of observing in a sample of simulated background-only experiments a more signal-like value of $-2\ln Q$. If the background-only hypothesis is correct, $1 - \mathrm{CL}_b$ is uniformly distributed between zero and one, thus its median expected value is 0.5. The observation of the value $1 - \mathrm{CL}_b = 1.35 \times 10^{-3}$ (2.85×10^{-7}) indicates a 3σ (5σ) excess in the data with respect to the background expectation. Similarly, the integral of the signal plus background $-2\ln Q$ distribution for values larger than the observed one gives the confidence level of the signal plus background, CL_{s+b}.

For convenience, the confidence level of the signal is defined as $\mathrm{CL}_s \equiv \mathrm{CL}_{s+b}/\mathrm{CL}_b$ [78]. While CL_b quantifies the lack of compatibility of an excess of observed events with the background-only hypothesis, CL_s gives information about how compatible it is with an actual signal. In a background-only scenario, a signal hypothesis is excluded at the α confidence level when $1 - \mathrm{CL}_s \geq \alpha$. The effect of systematic errors in the confidence levels is expected to be small [78].

Distributions of $1 - \mathrm{CL}_b$ and $1 - \mathrm{CL}_s$, expected for a Higgs boson signal of 250 GeV/c^2

mass, are displayed in Figure 3.12, as a function of the Higgs boson mass hypothesis, for an integrated luminosity of 10 fb^{-1}. The 1σ and 2σ bands on $1-\mathrm{CL}_b$ and $1-\mathrm{CL}_s$ stem from the Poisson statistical fluctuations of the number of signal and background events in each bin of the discriminant distribution.

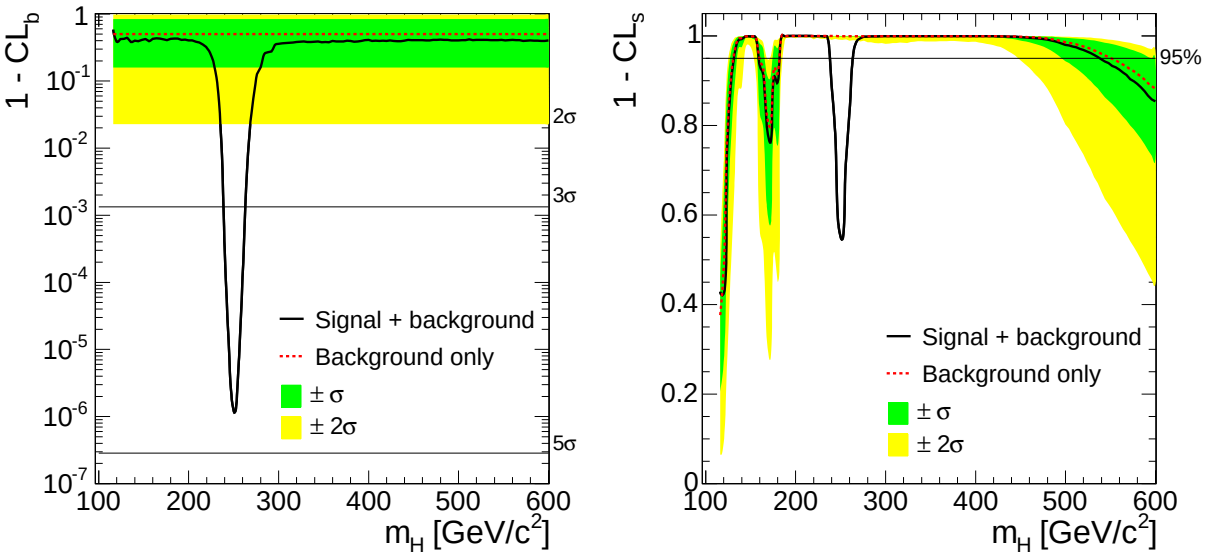

Figure 3.12: Distributions of $1-\mathrm{CL}_b$ (left) and $1-\mathrm{CL}_s$ (right), expected for a Higgs boson signal of 250 GeV/c^2 mass, as a function of the Higgs boson mass hypothesis, for an integrated luminosity of 10 fb^{-1}. The 1σ and 2σ bands on $1-\mathrm{CL}_b$ and $1-\mathrm{CL}_s$, originating from the Poisson statistical fluctuations of the number of background events in each bin of the discriminant distribution, are also drawn.

As an example, four-muon mass distributions for randomly selected pseudo-experiments, with the statistics expected for integrated luminosities of 5 fb^{-1} and 15 fb^{-1}, are shown in Figure 3.13, assuming a Higgs boson signal of 150 GeV/c^2. The corresponding $1-\mathrm{CL}_b$ distributions are also displayed.

While the Higgs boson signal has a low significance over the background expectation for 5 fb^{-1}, it is clearly visible after accumulating 10 fb^{-1} more, reaching a significance slightly above 3σ. Statistical fluctuations of the background are also visible in signal-free regions. The distribution of the event weight, $\log_{10}(s/b)$, is plotted in Figure 3.14 for the expected signals, the expected background, and the events observed in the pseudo-experiment for the integrated luminosity of 15 fb^{-1}. The observed events have different weights when interpreted under different Higgs boson mass hypotheses, $m_\mathrm{H} = 140$ GeV/c^2, 146 GeV/c^2, 150 GeV/c^2 and 154 GeV/c^2. The Higgs boson candidates have the highest weights for the true m_H hypothesis, 150 GeV/c^2, while remain background-like for other mass hypotheses.

The log-likelihood ratio method allows the evolution of the weight of the candidates, s/b, to be determined as a function of the luminosity and the Higgs boson mass hypothesis, which

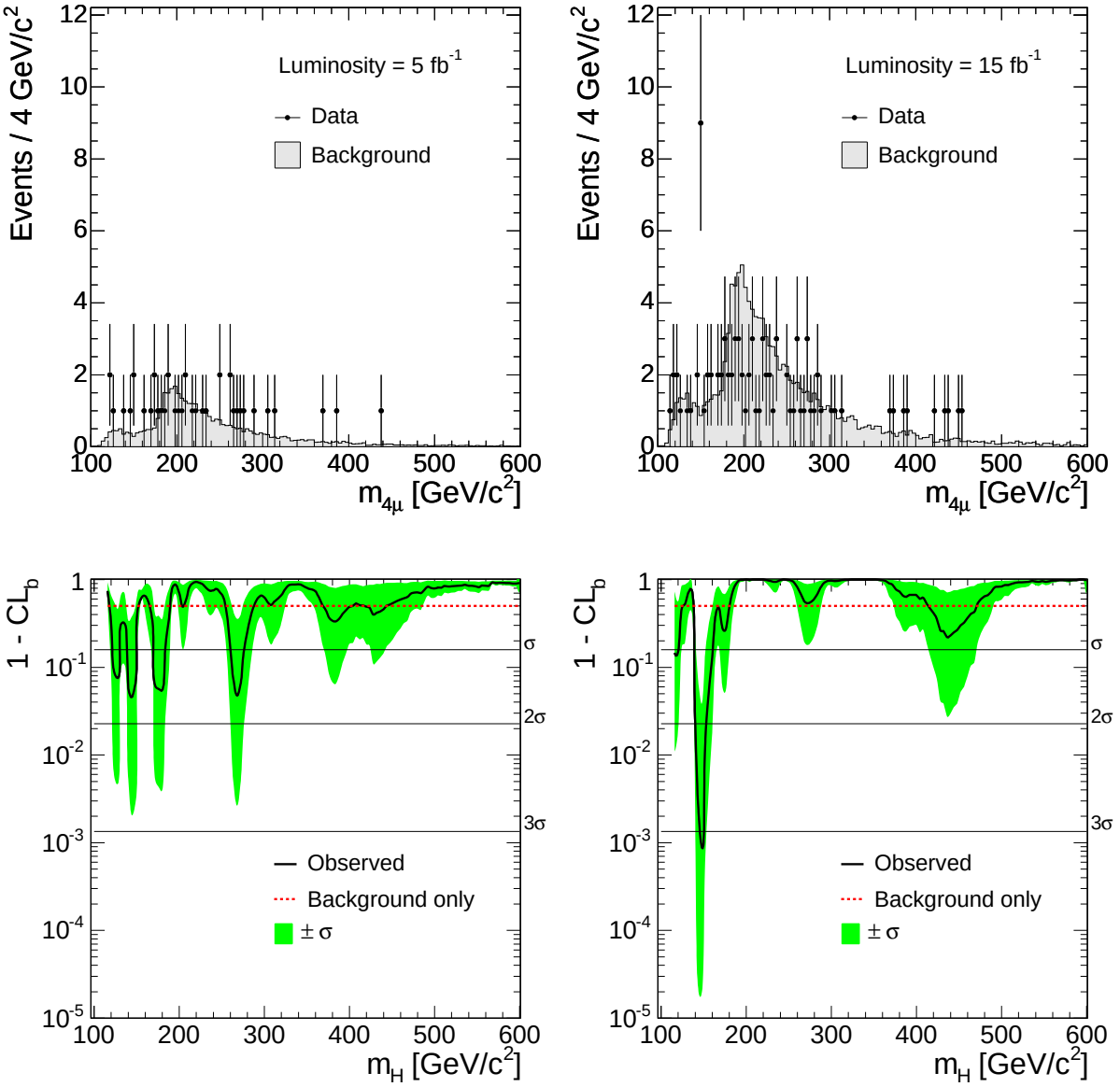

Figure 3.13: (Top) Four-muon mass distributions for randomly selected pseudo-experiments, labeled *data*, with the statistics expected for integrated luminosities of 5 fb^{-1} (left) and 15 fb^{-1} (right), assuming a Higgs boson signal of 150 GeV/c^2. (Bottom) The corresponding $1 - \mathrm{CL}_b$ distributions are also displayed, as a function of the Higgs boson mass hypothesis, for the expected background and for the observed events, together with the 1σ band around the observed value.

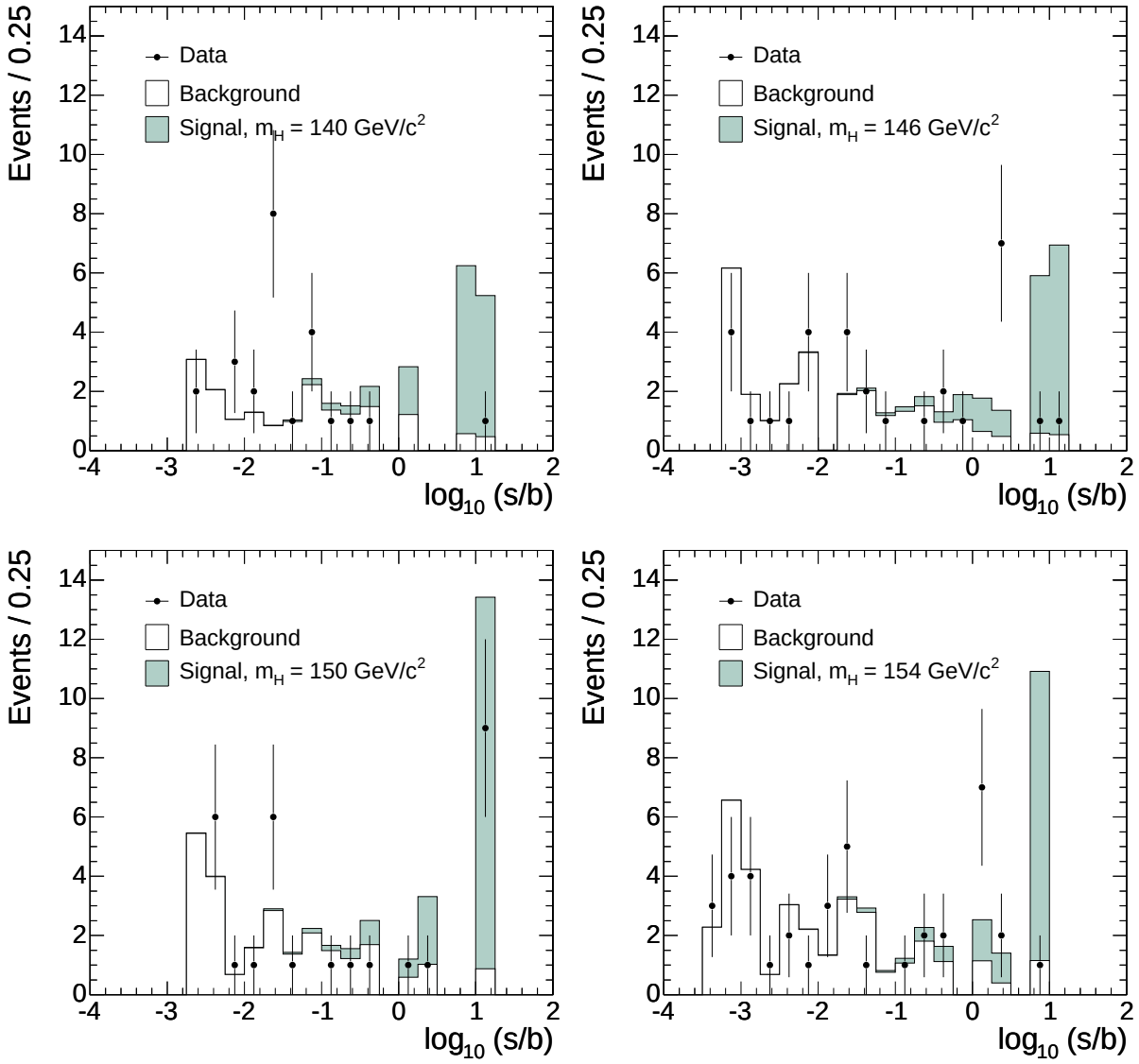

Figure 3.14: Distribution of $\log_{10}(s/b)$ for the randomly selected pseudo-experiment of Figure 3.13 (right), which correspond to an integrated luminosity of 15 fb^{-1}, for various Higgs boson mass hypotheses: (upper-left) $m_{\mathrm{H}} = 140$ GeV/c^2, (upper-right) 146 GeV/c^2, (lower-left) 150 GeV/c^2 and (lower-right) 154 GeV/c^2. The histograms denote the expected signals (shaded) and background (open) distributions, while the dots with error bars represent the data.

is an important instrument for the search of new particles. This method, previously exploited by the LEP experiments [18], also facilitates the statistical combination of search analyses for different physics channels, with different statistical power and discriminant distributions. Such combinations will improve significantly the sensitivity of CMS to possible Higgs boson signals. The internal consistency of the search results from different physics channels will reinforce the conclusions drawn by CMS with respect to eventual claims for discovery.

3.6 Conclusions

The $\mathrm{H} \rightarrow \mathrm{ZZ}^{(*)} \rightarrow 4\mu$ process has been shown to be a very clean channel for the discovery of the Standard Model Higgs boson in a wide range of masses. Higgs boson signal samples are selected with relatively high efficiency and purity using a mass-independent cut-based analysis. The signal significance, determined from the four-muon mass distribution of the signal events using the log-likelihood statistical method, is found to be close to 5σ, for an integrated luminosity of 10 fb^{-1}, for masses around 140 GeV/c^2 and between 180 GeV/c^2 and 400 GeV/c^2. The strategy for the Higgs boson search with data is outlined, based on the use of the confidence levels CL_b and CL_s and on the detailed knowledge of the s/b distribution of the expected background and signal events and the observed candidates.

Chapter 4

Determination of the Standard Model Higgs boson mass, cross section, and width

Assuming that a Standard Model Higgs boson is observed, the discovery will be followed by the measurement of its properties, such as the mass, cross section, and width. The knowledge of these parameters will provide a deeper understanding of the electroweak symmetry-breaking mechanism. The $H \rightarrow ZZ^{(*)} \rightarrow 4\mu$ decay channel possesses a high discovery potential for a wide range of masses. In addition, it provides the best sensitivity for a precise mass reconstruction. Previous studies on the reconstruction of the Higgs-boson mass and width can be found elsewhere [80].

In this chapter we present a measurement procedure of the Higgs-boson mass, inclusive production cross section, and width using the $H \rightarrow ZZ^{(*)} \rightarrow 4\mu$ decay channel at the CMS experiment, for Higgs-boson masses between 130 GeV/c^2 and 600 GeV/$c^2$and for an integrated luminosity of 30 fb^{-1}. The reconstructed four-muon mass spectrum, $m_{4\mu}$, of fully simulated signal and background events described in Section 3.3 is used for this purpose. The measurement of the mass, width, and the production cross section is done by fitting the $m_{4\mu}$ distribution with a suitable function that describes both the signal and the background contributions. This function takes into account the experimental resolution and the radiative tail due to internal bremsstrahlung in the final state, and depends on the parameters under study.

4.1 Fitting procedure

The capabilities of the CMS detector to measure the mass, cross section, and width of the Standard Model Higgs boson are determined for an integrated luminosity of 30 fb^{-1}. A function that depends on these parameters is fitted to the reconstructed invariant mass distribution of the four muons including the signal and background contributions after all the selection cuts described in Section 3.4 have been applied. The value of the parameters, together with their errors, are obtained directly from the fit.

A binned maximum likelihood fit to the reconstructed four-muon invariant mass is used to

measure the parameters of the Higgs-boson mass spectrum. The "observed" distribution, f_{sb}, is expressed in terms of the signal, p_s, and background, p_b, probability density functions (*p.d.f.*) as

$$f_{sb}(m_{4\mu}; m_{fit}, \Gamma, \alpha, N_{sb}) = N_{sb}\left[\alpha \cdot p_s(m_{4\mu}; m_{fit}, \Gamma) + (1-\alpha)\cdot p_b(m_{4\mu})\right]$$

where $N_{sb} = N_s + N_b$ is the normalization constant, m_{fit} the position of the mass peak, Γ the intrinsic width of the Higgs boson and α the fraction of signal events:

$$\alpha = \frac{N_s}{N_s + N_b}; \quad 1-\alpha = \frac{N_b}{N_s + N_b}$$

For convenience, the function f_{sb} can also be written as $f_{sb} = N_s \cdot p_s + N_b \cdot p_b$, where $N_s = N_{sb}\cdot\alpha$ is the number of signal events and $N_b = N_{sb}\cdot(1-\alpha)$ the number of background events.

A precise description of the reconstructed four-muon mass spectra must take into account both the experimental resolution and the radiative tail due to internal bremsstrahlung. The signal *p.d.f.* is therefore the sum of two contributions: a convolution of a Breit-Wigner signal shape with a Gaussian distribution that accounts for detector resolution, p_{core}, and a function that reproduces the radiative tail, p_{tail}:

$$p_s = \beta \cdot p_{core}(m_{4\mu}; m_{fit}, \Gamma, \sigma) + (1-\beta)\cdot p_{tail}(m_{4\mu}; m_{fit}, \tau)$$

where $1-\beta$ is the fraction of signal events in the radiative tail. The tail shape is parameterized *ad hoc* as

$$p_{tail} = \frac{(m_{4\mu} - m_{fit})^2}{2\tau^3}\exp\left(\frac{m_{4\mu} - m_{fit}}{\tau}\right)$$

if $m_{4\mu} < m_{fit}$ and is zero otherwise [59]. Figure 4.1 (top-left) illustrates the different contributions to the parameterization of the signal plus background distribution, f_{sb}.

The p_s function is fitted to the signal-only distributions to obtain the parameters of the radiative tail, which remain fixed in the fit to the signal plus background spectra. Some examples of signal distributions, for several Higgs boson masses, are shown in Figure 4.1, together with the result of a binned maximum likelihood fit.

For Higgs boson masses below 190 GeV/c^2, the intrinsic width is negligible compared to the mass spread introduced by the experimental resolution and the signal could be approximated by a Gaussian shape. For masses above 400 GeV/c^2, the natural width of the Higgs is much larger than the experimental resolution, hence the description using a pure Breit-Wigner function yields similar parameters to those obtained from the convolution.

The detector resolution is extracted from the $m_{4\mu}$ distribution of ZZ events with a four-muon mass above $2m_Z$, for which the kinematics are similar to that of the signal. For masses below $2m_Z$, the intrinsic Higgs boson width is negligible, therefore the resolution is measured directly from the width of the $m_{4\mu}$ distribution. This width has been found to be consistent with the extrapolation of the resolution determined using ZZ events. When real data become available, the experimental resolution is expected to be obtained from the width of the Z, J/ψ and Υ resonances, measured using their decays into muon pairs [81].

In order to determine the experimental resolution, a Gaussian fit is performed to the distribution of $(m_{4\mu} - m_{4\mu}^{gen})/m_{4\mu}^{gen}$ for several ranges of $m_{4\mu}$ (Figure 4.2), where $m_{4\mu}^{gen}$ is the true

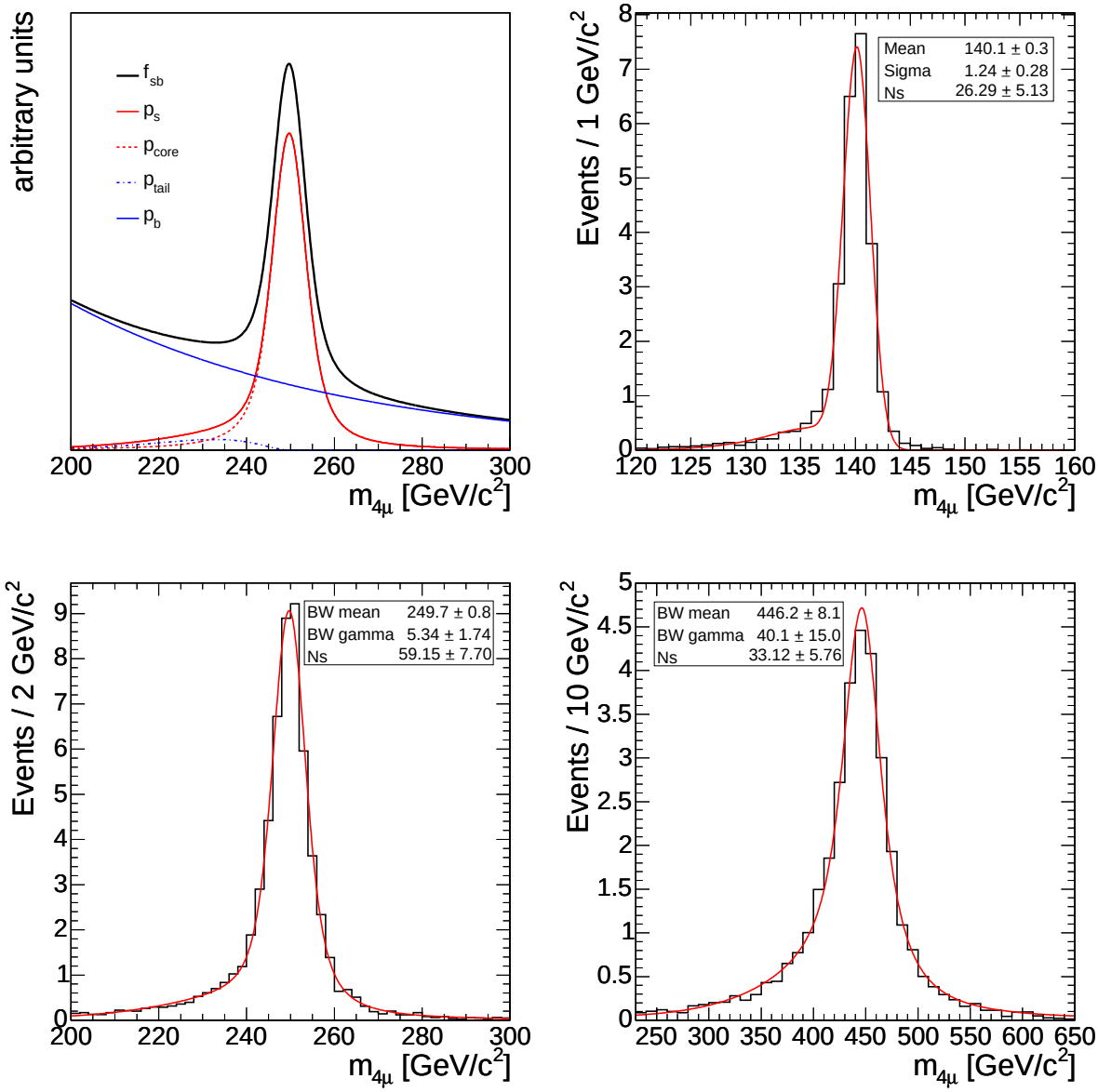

Figure 4.1: Example of the shapes of the different contributions to f_{sb} (top-left). Reconstructed four-muon mass distributions for Higgs signals corresponding to $m_{\mathrm{H}} = 140$ GeV/c^2, 250 GeV/c^2 and 450 GeV/c^2, together with the result of the fits (solid lines and numbers).

four-muon mass. The evolution of the width of the Gaussian with $m_{4\mu}$ (Figure 4.3) is parameterized with a linear function. The resolution obtained from this parameterization is a fixed parameter in the fit, allowing for an independent determination of the Higgs boson intrinsic width.

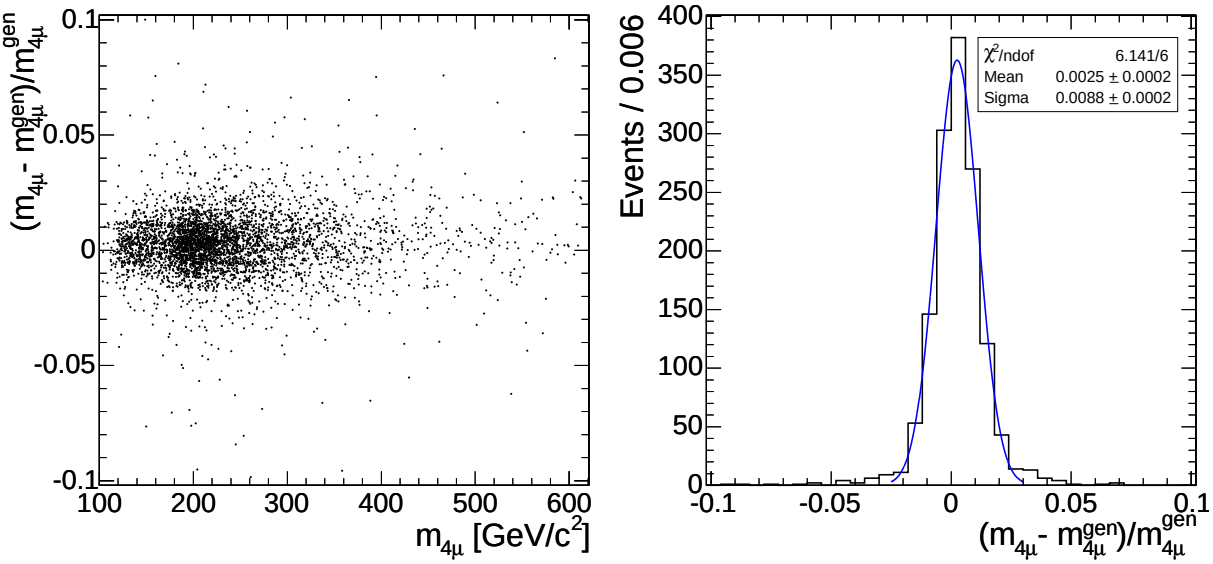

Figure 4.2: (Left) Distribution of $(m_{4\mu} - m_{4\mu}^{gen})/m_{4\mu}^{gen}$ as a function of $m_{4\mu}$, for ZZ events. (Right) Gaussian fit to the $(m_{4\mu} - m_{4\mu}^{gen})/m_{4\mu}^{gen}$ distribution for $m_{4\mu}$ in the range between 200 GeV/c^2 and 250 GeV/c^2.

The background *p.d.f.*, p_b, is approximated by either a polynomial or an exponential function, depending on the mass region under study. The parameters are determined by performing a binned maximum likelihood fit to the background sample. The parameters defining the shape of the background are fixed in the global fit to signal plus background, but the normalization is a free parameter.

4.2 Results

A binned maximum likelihood fit to the reconstructed $m_{4\mu}$ signal plus background distribution is performed using the function f_{sb}. The fits to the signal plus background distributions are shown in Figures 4.4, 4.5 and 4.6, for all the simulated Higgs boson masses. For $m_{4\mu} < 190$ GeV/c^2 a Gaussian with free width is used for the signal, while for larger masses the convolution of a fixed-width Gaussian and a free-width Breit-Wigner is used.

The free parameters of the fit correspond to the physical parameters that describe the Higgs boson resonance: normalization, mass, and width. The precision in the determination of the production cross section is computed using the number of signal events obtained from the fit.

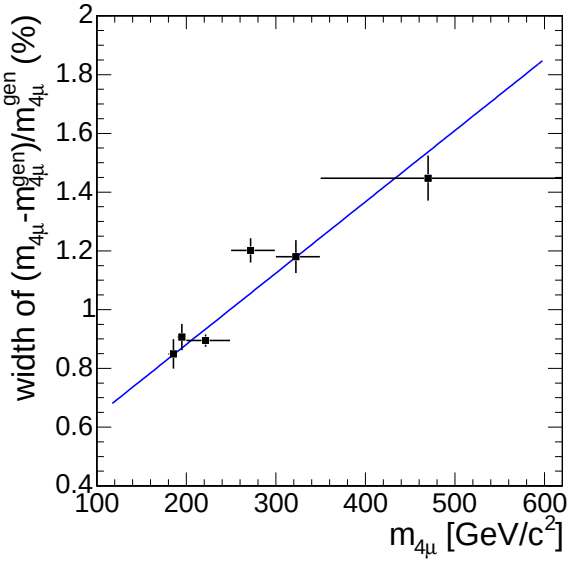

Figure 4.3: Evolution of the width of the $(m_{4\mu} - m_{4\mu}^{gen})/m_{4\mu}^{gen}$ distribution with $m_{4\mu}$, obtained from ZZ events. The dots with error bars indicate the result of the Gaussian fits performed in the selected mass ranges. The line represents the linear fit to those points.

Figure 4.7 (left) depicts the relative shift of the fitted Higgs boson mass with respect to the true mass, together with its statistical error. These values are compatible with zero in the full range of masses, which means that the true mass is accurately recovered after applying the fitting method to the reconstructed sample. The evolution of the relative error as a function of the true mass is displayed in Figure 4.7 (right), showing that the mass can be measured with a precision from 0.1% to 5.4%. The increase in this error around 170 GeV/c^2 is due to the smaller number of signal events caused by the suppression of the $H \to ZZ^{(*)}$ decay at the opening of the $H \to W^+W^-$ resonant channel. The increasing uncertainty at higher masses is due to the smaller production cross sections, the larger intrinsic width of the Higgs boson, and, to a lesser extent, the worse resolution for high p_T muons.

The number of signal and background events is obtained from the fit. The relative error in the cross-section measurement is determined from the number of signal events (N_s) and its statistical uncertainty (ΔN_s) as $\Delta N_s/N_s$, shown in Figure 4.8 as a function of the Higgs boson mass. The contribution of the background is properly taken into account, as its normalization is a free parameter in the fit. The cross section can be determined with a precision between 20% and 45%, except for masses below 130 GeV/c^2, where the branching ratio of the Higgs boson into four muons is low.

The remaining physical parameter obtained from the fit is the width of the Higgs boson. The measured width and its statistical error are presented in Figure 4.9 as a function of the true mass, together with the theoretical calculation. The width can be determined above 190 GeV/c^2 with an error between 35% and 45%. Below this mass the intrinsic theoretical width is of the

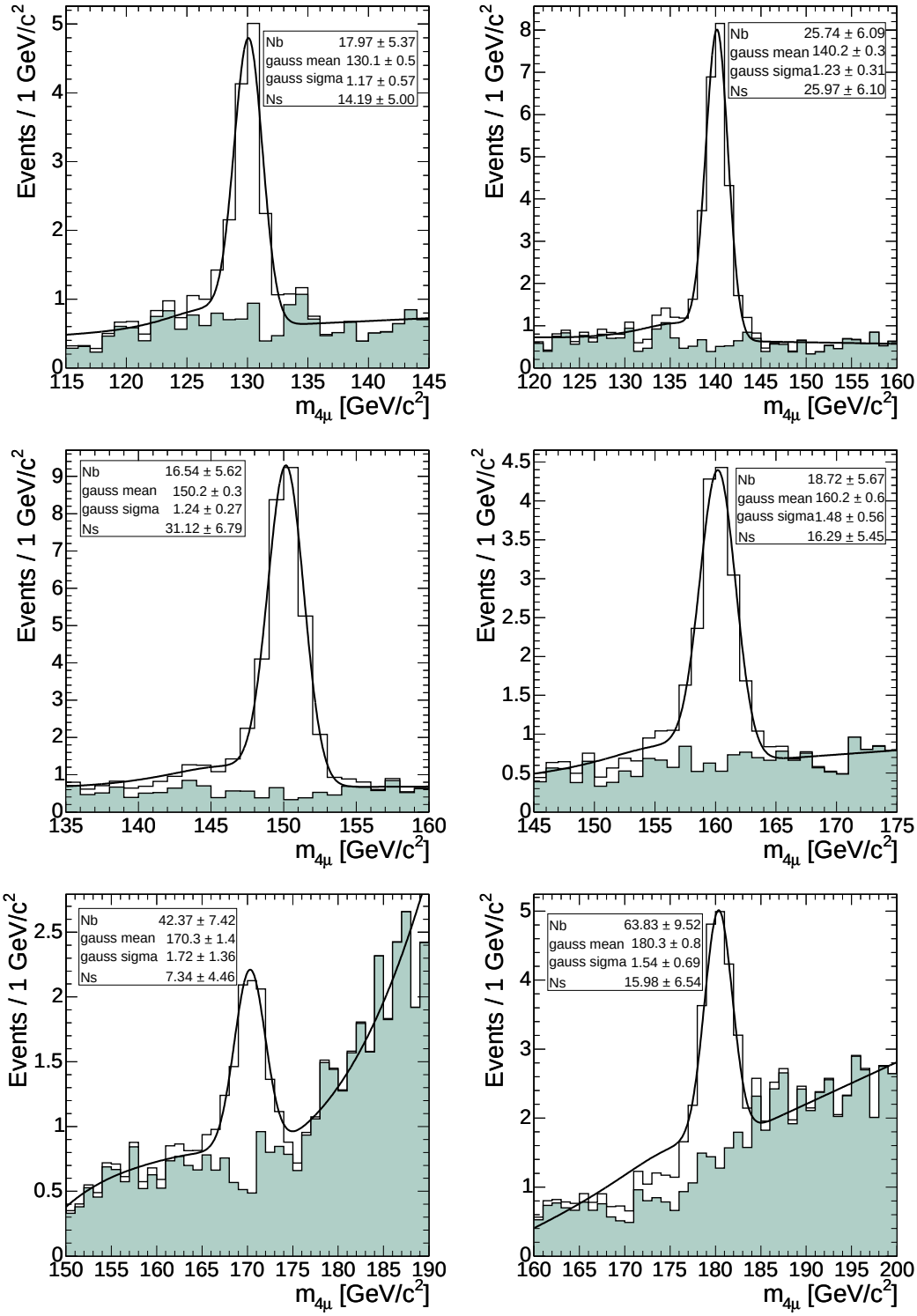

Figure 4.4: Distributions of the reconstructed signal (open histograms) plus background (shaded) four-muon mass distributions, for an integrated luminosity of 30 fb^{-1}, together with the fit results (solid line), for masses in the range from 130 GeV/c^2 to 180 GeV/c^2. The fit parameters and their errors are also shown.

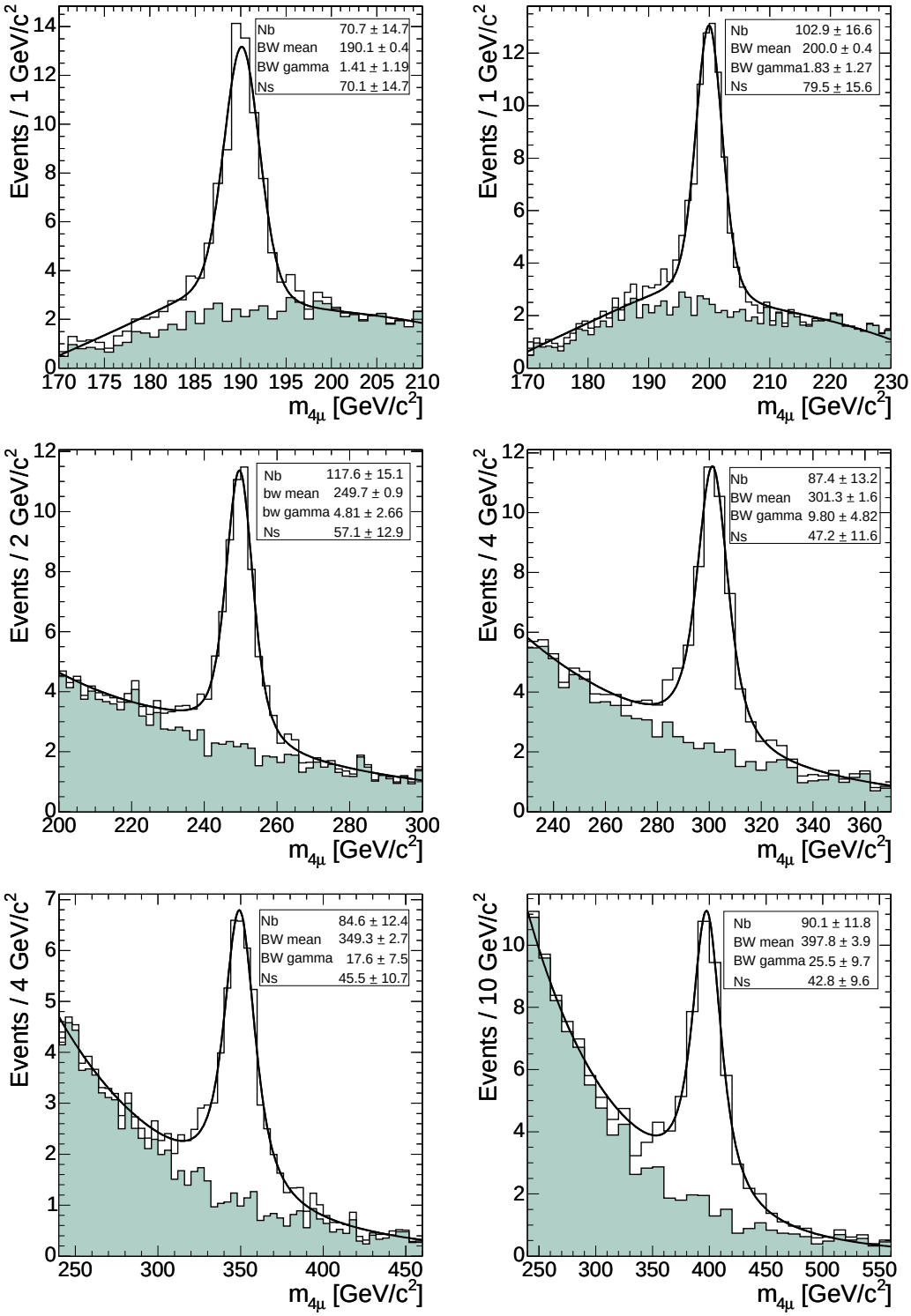

Figure 4.5: Distributions of the reconstructed signal (open histograms) plus background (shaded) four-muon mass distributions, for an integrated luminosity of 30 fb^{-1}, together with the fit results (solid line), for masses in the range from 190 GeV/c^2 to 400 GeV/c^2. The fit parameters and their errors are also shown.

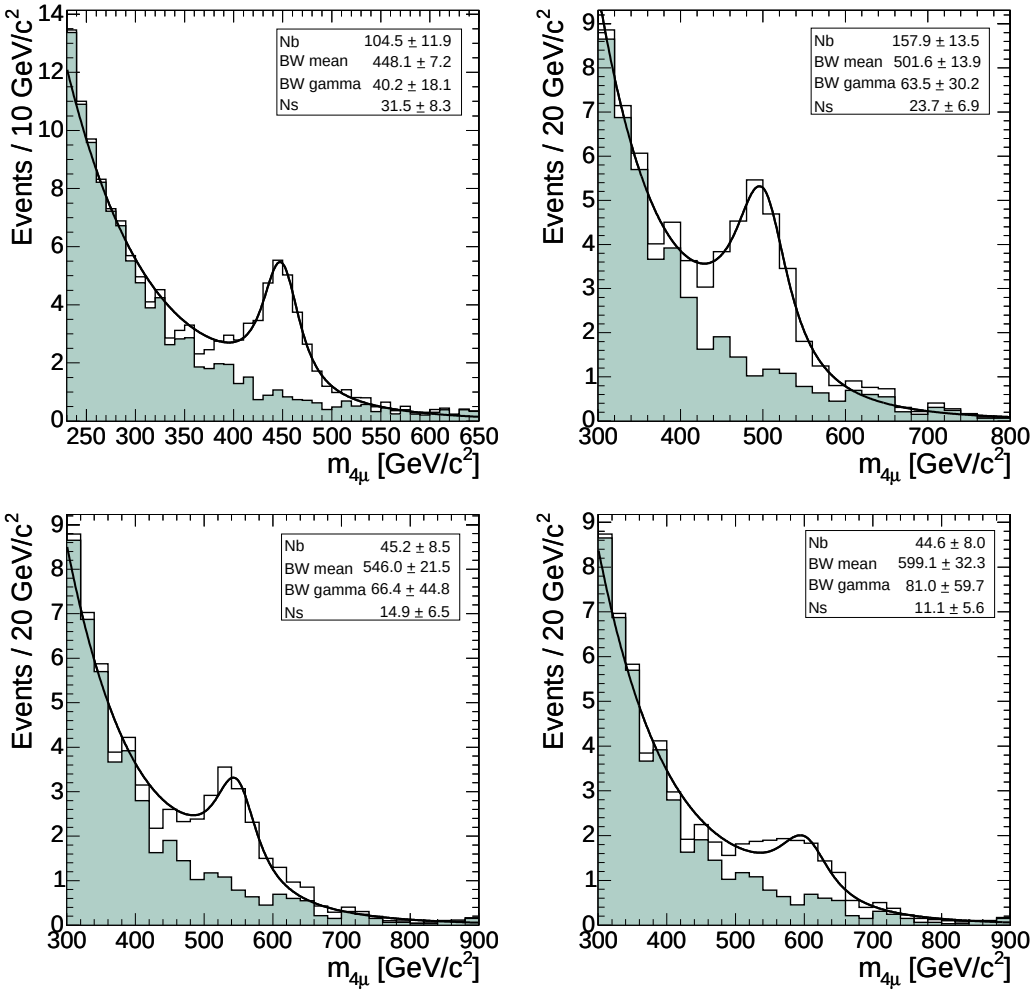

Figure 4.6: Distributions of the reconstructed signal (open histograms) plus background (shaded) four-muon mass distributions, for an integrated luminosity of 30 fb^{-1}, together with the fit results (solid line), for masses in the range from 450 GeV/c^2 to 600 GeV/c^2. The fit parameters and their errors are also shown.

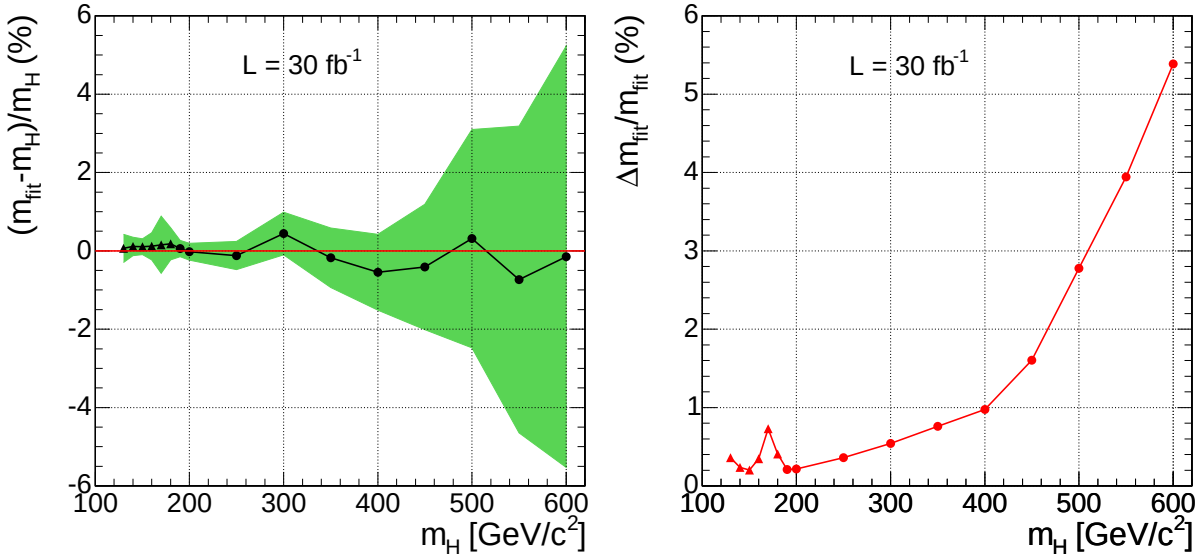

Figure 4.7: (Left) Relative shift of the fitted value of the Higgs boson mass with respect to the input m_{H} value, as a function of m_{H}. The shaded area is the error in the determination of the peak value from the fit for an integrated luminosity of 30 fb^{-1}, also shown as a function of the Higgs boson mass (Right). The dots correspond to the result of the convolution and the triangles to the Gaussian approximation.

order of 10^{-3} GeV/c^2 – 10^{-1} GeV/c^2, around two to three orders of magnitude less than the experimental detector resolution. There is no sensitivity to perform a direct measurement of the Higgs boson width for $m_{\mathrm{H}} < 190$ GeV/c^2, and upper limits at 95% C.L. are set. For comparison, the width obtained by fitting only a Gaussian for masses below 200 GeV/c^2 and only a Breit-Wigner for masses above 200 GeV/c^2 is also shown, together with the statistical uncertainty. The Breit-Wigner-only fits do not take into account the detector resolution, and therefore the intrinsic theoretical values are not recovered.

The determination of the Higgs boson parameters is affected by systematic uncertainties in the muon momentum resolution (obtained from data), in the muon reconstruction efficiency (around 2%), and those associated with the selection cuts (close to 1%) [2]. The cross-section measurement is also affected by the uncertainty in the luminosity determination, which is 3% for integrated luminosities above 30 fb^{-1}. These systematic uncertainties are mostly uncorrelated. The impact on the measured mass and width is expected to be small. Figure 4.8 shows the effect of the systematic uncertainties on the determination of the cross section.

The reconstructed four-muon mass spectra used in this analysis are obtained by weighting the fully simulated signal and background events down to the number of events expected for an integrated luminosity of 30 fb^{-1}. For assessing the robustness of the fitting procedure, a large number of pseudo-experiments has been performed for Higgs boson signals for which the expected number of events at 30 fb^{-1} is significantly low. The values of the parameters and their

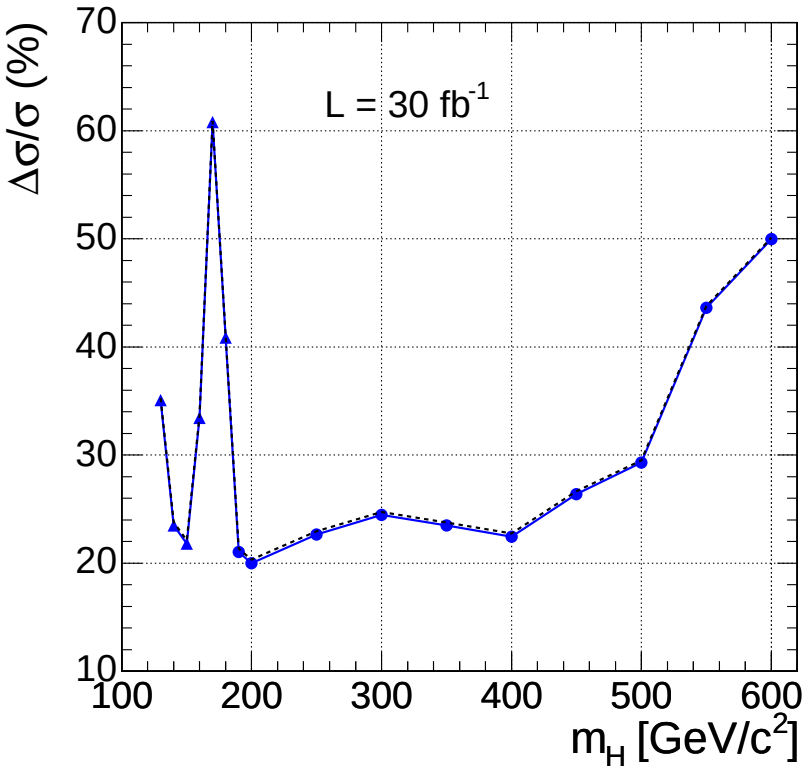

Figure 4.8: Relative error (solid line) in the cross-section measurement as a function of the Higgs boson mass calculated as $\Delta N_s/N_s$. N_s is the number of signal events and ΔN_s the statistical error obtained from the fit. The dots correspond to the result of the convolution and the triangles to the Gaussian approximation. The dashed line indicates the impact of the systematic uncertainties in the cross-section measurement arising from the luminosity measurement and the overall efficiency of the event selection and detector performance.

uncertainties, obtained from the fit to these distributions, are in agreement with the fit results using weighted distributions. This is true for the whole Higgs boson mass range under study, 130 GeV/c^2 < m_{H} < 600 GeV/c^2. As an example, the results of the fits corresponding to four Higgs boson signals are shown in Figure 4.10 for expected distributions in data. These results are compatible with the true values of the parameters within their statistical uncertainties.

For extending the measurement of the Higgs boson parameters to smaller masses or to lower luminosities, it would be more appropriate to extract the parameters from a large set of randomly chosen four-muon mass distributions with the correct number of events. This procedure can be applied to other four-lepton final states. The combination of these decay channels will improve the precision in the determination of the parameters.

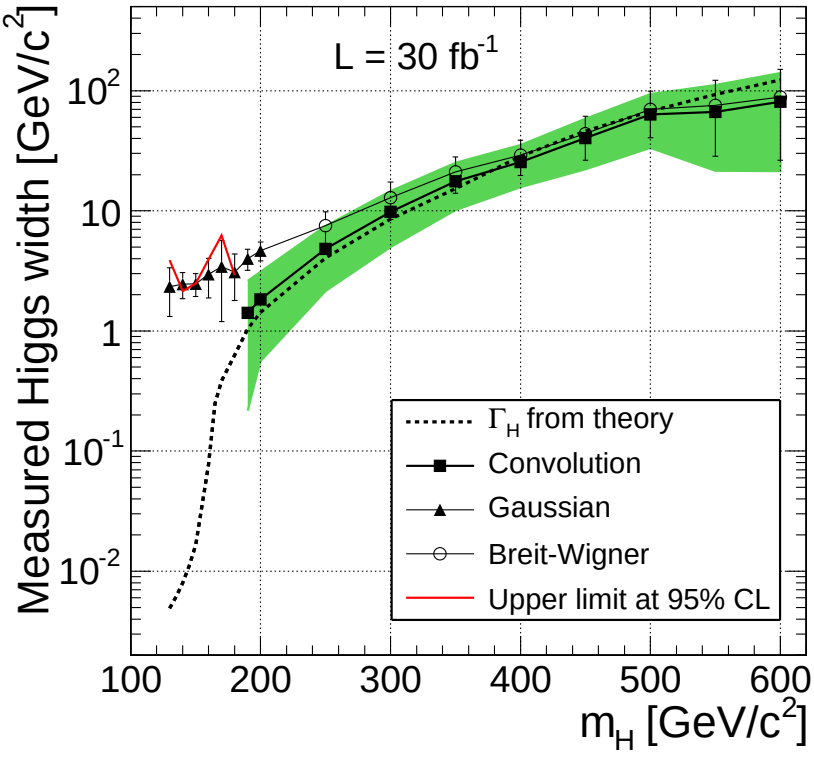

Figure 4.9: Measured Higgs boson width from a fit to the signal plus background distribution (squares), for the simulated Higgs boson masses. The error on the width from the fit is indicated by the solid band. There is no sensitivity to this parameter for masses below 190 GeV/c^2, therefore upper limits at 95% C.L. are shown (solid line). The results of a Gaussian fit to $m_{\mathrm{H}} \leq 200$ GeV/c^2 (triangles) and Breit-Wigner fit to $m_{\mathrm{H}} > 200$ GeV/c^2 (open circles) are also shown for comparison. The dashed line represents the theoretical calculation of Γ_{H}.

4.3 Conclusions

The $\mathrm{H} \rightarrow \mathrm{ZZ}^{(*)} \rightarrow 4\mu$ decay channel has been shown to be very sensitive for the determination of the Higgs boson mass, cross section, and width, for Higgs boson masses between 130 GeV/c^2 and 600 GeV/c^2. A robust method has been developed to measure accurately these parameters, using a binned maximum likelihood fit to the reconstructed $m_{4\mu}$ distribution, obtained from fully simulated events. The true values of the parameters are accurately recovered in the full range of masses. For an integrated luminosity of 30 fb^{-1}, the mass can be measured with a precision between 0.1 % and 5.4 %. The intrinsic width can only be measured when the Higgs boson is heavier than 190 GeV/c^2, with a precision around 35%, the experimental resolution dominating for lower masses. The production cross section can be determined with a precision around 30% for masses in the range 130 GeV/c^2- 150 GeV/c^2 and above 190 GeV/c^2.

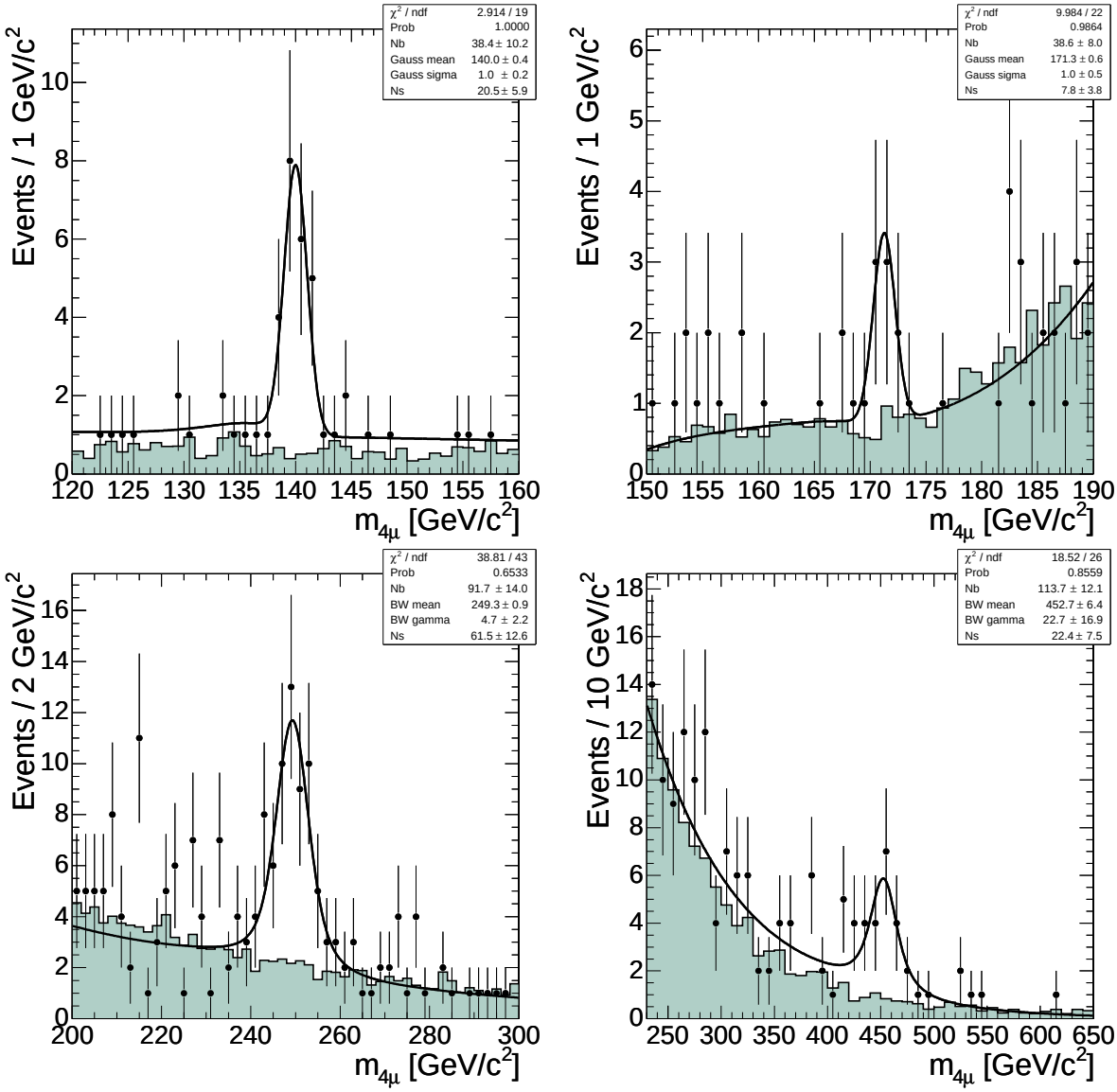

Figure 4.10: Data-like distributions expected for Higgs boson signals of $m_{\mathrm{H}} = 140$ GeV/c^2, 170 GeV/c^2, 250 GeV/c^2 and 450 GeV/c^2, for an integrated luminosity of 30 fb^{-1}, together with the result of the fits (solid lines). The shaded areas represent the expected background. These pseudo-experiments are selected randomly.

Chapter 5

Conclusions

The LHC will be the first accelerator to provide parton-parton collisions up to energies of about 1 TeV, the energy scale relevant to the electroweak symmetry breaking and at which beyond the Standard Model phenomena are expected to appear. If the elusive Standard Model Higgs boson exists, LHC will enable its production in the entire range of its allowed possible mass (from 114.4 GeV/c^2 to $\sim$ 1 TeV/c^2). An early discovery of the Higgs boson is one of the most important goals of the CMS experiment. This will require a good understanding of both the detector and the data to ensure the optimal performance of CMS when LHC delivers the first beams (summer of 2008).

The research work presented in this thesis, which I have carried out since 2004 within the High Energy Physics group at CIEMAT, is an important contribution to both the better understanding of the CMS detector and the potential of CMS to discover the Standard Model Higgs boson signal. The main results are summarized below.

We have performed the first measurement of a physical quantity using real data in the CMS experiment: the measurement of the ratio of positive- to negative-charge cosmic muons as a function of the muon momentum, using data collected at the *Magnet Test and Cosmic Challenge* (MTCC) and exploiting the capabilities of the muon barrel drift tube chambers. While physics studies were beyond the scope of the MTCC and cosmic muon physics is not among the goals of CMS, we have succeeded to obtain a result of good quality, also accounting for the most important systematic uncertainties that affect the measurement. The cosmic muon charge ratio is found to be independent of the muon momentum in the considered range, which is in good agreement with previous measurements within the experimental uncertainties. In addition to the inherent interest of the measurement, for the CMS collaboration it has meant a successful test of the complete analysis chain before the LHC start-up, since it has been performed in an environment, CMS and Grid wise, similar to that designed for the analysis of the data coming from proton-proton collisions, using standard CMS reconstruction software, data distribution and job submission tools. Furthemore, it has provided a complementary check of the detector performance, allowing us to address important issues concerning both the alignment constants of the muon detector and the reconstruction code of CMS. As a result, the measurement of the cosmic muon charge ratio has been included in the "to-do" list of detector calibration tests for the cosmic runs at zero and 4 T that have already started to be taken at CMS, almost completely

assembled and installed in the experimental cavern since February 2008.

We have also presented the search analysis of the Standard Model Higgs boson using the $H \rightarrow ZZ^{(*)} \rightarrow 4\mu$ decay channel in the CMS experiment. The $H \rightarrow ZZ^{(*)} \rightarrow 4\mu$ process has been shown to be a very clean channel for the discovery of the Standard Model Higgs boson in a wide range of masses. Higgs boson signals, ranging from 115 GeV/c^2 to 600 GeV/c^2, and background samples are generated at LO and normalized to the value of the total cross section at NLO. The latest available at the moment, official CMS software has been used to fully simulate the detector response and reconstruct the events. Higgs boson samples are selected with relatively high efficiency and purity using a mass-independent cut-based analysis that exploits the relatively narrow shape of the invariant mass distribution of the four muons in the final state. The expected signal significance is determined from the four-muon mass distribution of the signal events using the log-likelihood statistical method, and is found to be close to 5σ, for an integrated luminosity of 10 fb^{-1}, for masses around 140 GeV/c^2 and between 180 GeV/c^2 and 400 GeV/c^2. The strategy for the Higgs boson search with data is outlined, based on the use of the confidence levels CL_b and CL_s that caracterize either the background-only or the signal-plus-background likeliness of the data and on the detailed knowledge of the s/b distribution of the expected background and signal events and the observed candidates.

The $H \rightarrow ZZ^{(*)} \rightarrow 4\mu$ decay channel has also been shown to be very sensitive for the determination of the Higgs-boson mass, cross section, and width, for Higgs-boson masses between 130 GeV/c^2 and 600 GeV/c^2. A robust method has been developed to measure accurately these parameters, using a binned maximum likelihood fit to the reconstructed four-muon mass distribution, obtained from fully simulated and reconstructed events. The function describes both the signal and the background contributions and takes into account the experimental resolution and the radiative tail due to internal bremsstrahlung in the final state, and depends on the parameters under study. The true values of the parameters are accurately recovered in the full range of masses already for an integrated luminosity of 30 fb^{-1}. The mass can be measured with a precision between 0.1% and 3.7%. The intrinsic width can only be measured when the Higgs boson is heavier than 190 GeV/c^2, with a precision around 25%, the experimental resolution dominating for lower masses. The production cross section can be determined with a precision around 20% for masses in the range 130 GeV/c^2 - 150 GeV/c^2 and above 190 GeV/c^2.

I plan to continue my research work and exploit the experience accumulated in data analysis and the developed analysis strategies to the LHC data, making significant contributions to the search for the Standard Model Higgs boson and other new physics signals beyond the Standard Model that can be found in LHC.

Bibliography

[1] M. Aldaya, P. Garcia-Abia, *Measurement of the charge ratio of cosmic muons using CMS data*, CMS NOTE 2008 approved by the referees; waiting for ID number to be assigned.

[2] M. Aldaya et al., *Discovery potential and search strategy for the Standard Model Higgs boson in the* $H \rightarrow ZZ^{(*)} \rightarrow 4\mu$ *decay channel using a mass-independent analysis*, CMS NOTE 2006/106.

[3] M. Aldaya et al., *A method for determining the mass, cross-section and width of the Standard Model Higgs boson using the* $H \rightarrow ZZ^{(*)} \rightarrow 4\mu$ *decay channel*, CMS NOTE 2006/107.

[4] CMS Collaboration, *CMS Technical Design Report, Volume II: Physics Performance*, J. Phys. G: Nucl. Part. Phys. 34 (2007) 995-1579; CERN-LHCC-2006-021 (2006); section 3.1.

[5] The LHC Study Group, *The Large Hadron Collider Conceptual Design*, CERN/AC 95-05 (1995);
LHC Project, http://lhc.web.cern.ch/lhc/.

[6] CMS Collaboration, *The CMS experiment at the CERN LHC*, to be published in the Journal of Instrumentation (JINST), 2008.

[7] CMS Physics TDR, Volume I, CERN-LHCC-2006-001 (2006).

[8] S. L. Glashow, Nucl. Phys. 22 (1961) 579;
S. Weinberg, Phys. Rev. Lett. 19 (1967) 1264;
A. Salam, *Elementary Particle Theory*, ed. N. Svartholm (Almqvist and Wiksell, Stockholm, 1968), p. 367.

[9] M. Gell-Mann, Phys. Lett. 8 (1964) 214;
G. Zweig, CERN-Report 8182/TH401 (1964);
H. Fritzsch, M. Gell-Mann, H. Leutwyler, Phys. Lett. B 47 (1973) 365;
D. Gross, F. Wilczek, Phys. Rev. Lett. 30 (1973) 1343;
H.D. Politzer, Phys. Rev. Lett. 30 (1973) 1346;
G. 't Hooft, Marseille Conference on Yang Mills Fields, 1972.

[10] P.A.M. Dirac, Proc. Roy. Soc. Lond. A 114 (1927) 243;
P. Jordan, W. Pauli, Z. Phys. 47 (1928) 151;
W. Heisenberg, W. Pauli, Z. Phys. 56 (1929) 1;

S. Tomonaga, Progr. Theoret. Phys. 1 (1946) 27;
J. Schwinger, Phys. Rev. 73 (1948) 416;
R. Feynman, Phys. Rev. 76 (1949) 749.

[11] E. Fermi, Nuovo Cim. 11 (1934) 1;
E. Fermi, Z. Phys. 88 (1934) 161;
R. Feynman, M. Gell-Mann, Phys. Rev. 109 (1958) 193.

[12] G. 't Hooft, Nuclear Phys. B 33 (1971) 173;
G. 't Hooft, Nuclear Phys. B 35 (1971) 167;
G. 't Hooft, M. Veltman, Nuclear Phys. B 44 (1972) 189.

[13] N. Cabibbo, Phys. Rev. Lett. 10 (1963) 531;
M. Kobayashi and K. Maskawa, Prog. Theor. Phys. 49 (1973) 652.

[14] P.W. Higgs, Phys. Rev. Lett. 13 (1964) 508;
P.W. Higgs, Phys. Rev. 145 (1966) 1156;
F. Englert, R. Brout, Phys. Rev. Lett. 13 (1964) 321;
G.S. Guralnik, C.R. Hagen, T. Kibble, Phys. Rev. Lett. 13 (1965) 585;
T. Kibble, Phys. Rev. 155 (1967) 1554.

[15] The ALEPH, DELPHI, L3, OPAL, SLD Collaborations, the LEP Electroweak Working Group, the SLD Electroweak and Heavy Flavour Groups, *Precision Electroweak Measurements on the Z Resonance*, Phys.Rept. 427 (2006) 257, CERN-PH-EP/2005-041 (hep-ex/0509008).

[16] T. Hambye and K. Riesselmann, *Matching conditions and Higgs mass upper bounds revisited*, Phys. Rev. D 55 (1997) 7255.

[17] B. W. Lee, C. Quigg and H. B. Thacker, Phys. Rev. D16 (1977) 1519.

[18] ALEPH, DELPHI, L3 and OPAL Collaborations and the LEP Working Group for Higgs Boson Searches, *Search for the Standard Model Higgs boson at LEP*, Phys. Lett. B 565 (2003) 61, (hep-ex/0306033).

[19] Tevatron New Phenomena, Higgs Working group (TEVNPHWG), for the CDF Collaboration, the D0 Collaboration, *Combined CDF and D0 Upper Limits on Standard Model Higgs-Boson Production*, arXiv:0712.2383v1 [hep-ex].

[20] http://lepewwg.web.cern.ch/LEPEWWG/ (Status of March 2008).

[21] F. Zwicky, Astrop. J. 86 (1937) 217;
M. S. turner Phys. Rep. 333 (2000) 619;
Will J. Percival et al. MNRAS 381 (2007) 1053.

[22] Adam G. Riess et al (Supernova Search Team) Astronomical J. 116 (1998) 1009;
S. Perlmutter et al (Supernova Cosmology Project) Astrophysical J. 517 (1999) 565.

[23] E. Komatsu et al, Submitted to Astrop. J. Supp. (2008), arXiv:0803.0547 [astro-ph].

[24] D. J. Eisenstein et al. (SDSS Coll.) Astrophys. J. 633 (2005) 560.

[25] J. Hosaka et al. (SuperK Coll.) Phys. Rev. D73 (2006) 112001;
Q. R. Ahmad et al. (SNO Coll.) Phys. Rev. Lett. 89 (2002) 011301 and 011302;
B. Aharmim et al. (SNO Coll.) Phys. Rev. C72 (2005) 055502;
T. Araki et al. (KamLAND Coll.) Phys. Rev. Lett. 94 (2005) 081801;
Y. Fukuda et al. (SuperK Coll.) Phys. Rev. Lett. 81 (1998) 1562;
E. Aliu et al. (K2K Coll.) Phys. Rev. Lett. 94 (2005) 081802.

[26] A. Riotto, hep-ph/9807454 (CERN-TH/98-204);
A. D. Dolgov, hep-ph/9707419.

[27] CERN, http://www.cern.ch/.

[28] ATLAS Collaboration, http://atlas.web.cern.ch/Atlas/index.html.

[29] CMS Collaboration, http://cms.cern.ch/.

[30] LHCb collaboration, http://lhcb.web.cern.ch/lhcb/.

[31] ALICE Collaboration, http://aliceinfo.cern.ch/.

[32] The CERN Bulletin, Issue No. 14-15/2008, *A word from the DG: The home straight*.

[33] G. Altarelli and M. L. Mangano (editors), *Proceedings of the Workshop on Standard Model Physics (and more) at the LHC* (2000) CERN 2000-004.

[34] Ian Foster, Carl Kesselman, Steven Tuecke, *The Anatomy of the Grid. Enabling Scalable Virtual Organizations*.

[35] CMS Collaboration, *CMS Technical Design Report, Volume II: Physics Performance*, J. Phys. G: Nucl. Part. Phys. 34 (2007) 995-1579; CERN-LHCC-2006-021 (2006).

[36] The CMS Collaboration, *Technical Proposal*, CERN/LHCC 94-38, LHCC/P1 (1994).

[37] The CMS Collaboration, *The Tracker Project: Technical Design Report*, CERN/LHCC 98-006, CMS TDR 5 (1998);
The CMS Collaboration, *Addendum to the CMS Tracker Technical Design Report*, CERN/LHCC 2000-016, CMS TDR 5 Addendum 1 (2000).

[38] The CMS Collaboration, *The Electromagnetic Calorimeter Project: Technical Design Report*, CERN/LHCC 97-33, CMS TDR 4 (1997).

[39] The CMS Collaboration, *The Hadronic Calorimeter: Technical Design Report*, CERN/LHCC 97-31, CMS TDR 2 (1997).

[40] The CMS Collaboration, *The Magnet Project: Technical Design Report*, CERN/LHCC 97-10, CMS TDR 1 (1997).

[41] The CMS Collaboration, *The Muon Project, Technical Design Report*, CERN/LHCC 97-32, CMS TDR 3 (1997).

[42] CMS Collaboration, *The CMS Magnet Test and Cosmic Challenge (MTCC Phase I and II) Operational Experience and Lessons Learnt*, CMS-NOTE 2007/005.

[43] T. Hebbeker, C. Timmermans, Astropart. Phys. 18 (2002) 107-127;
J.M. Baxendale, C.J. Hume, M.G. Thompson, J. Phys. G 1 (1975) 781-788;
B.C. Rastin, J. Phys. G 10 (1984) 1629-1638.

[44] P. Achard *et al.*, L3 Collaboration, Phys. Lett. B 598 (2004) 15-32.

[45] The MINOS Collaboration, *Measurement of the Atmospheric Muon Charge Ratio at TeV Energies with MINOS*, arXiv:hep-ex/0705.381v4.

[46] P. Biallass, T. Hebbeker, K. Hoepfner, *Simulation of Cosmic Muons and Comparison with Data from the Cosmic Challenge using Drift Tube Chambers*, CMS-NOTE 2007/024.

[47] PhEDEx, *Physics Experimental Data Export*, http://cern.ch/cms-project-phedex/.

[48] CRAB, *CMS Remote Analysis Builder*, http://cmsdoc.cern.ch/cms/ccs/wm/www/Crab/.

[49] CMS Technical Design Report *The TriDAS Project, Volume 1: The Trigger Systems*, CERN/LHCC 98-6, CMS TDR 5 (1998).

[50] Version CMSSW_1_1_1 is used. There is not a publication specific to CMSSW. More information can be found in the web pages:
https://twiki.cern.ch/twiki/bin/view/CMS/WorkBook
https://twiki.cern.ch/twiki/bin/view/CMS/SWGuide.

[51] C. Liu, N. Neumeister, *Reconstruction of Cosmic and Beam-Halo Muons*, CMS-NOTE 2008/001.

[52] A.T. Meneguzzo *et al.*, *Method for the Measure of the Time of the Track Passage and of the Drift Velocity in the Drift Tube Chambers of CMS*, CMS NOTE in preparation.

[53] A. Calderón *et al.*, *Muon System alignment with tracks*, CMS-NOTE 2006/016;
A. Calderón *et al.*, *Link Alignment System MTCC Results*, CMS-IN 2007/050.

[54] J.F. Fuchs, R. Goudard and J.D. Maillefaud, *CMS-SUMMARY. YBs and YEs Position w.r.t. YB0 in SX5*, CMS-SG-UR-0490 (2006).

[55] A. Djouadi, J. Kalinowski, M. Spira, *HDECAY: a Program for Higgs Boson Decays in the Standard Model and its Supersymmetric Extension*, arXiv:hep-ph/9704448;
M. Spira, *HIGLU: A Program for the Calculation of the Total Higgs Production Cross Section at Hadron Colliders via Gluon Fusion including QCD Corrections*, arXiv:hep-ph/9510347.

[56] E. Yazgan *et al.*, *Search for a Standard Model Higgs Boson in CMS via Vector Boson Fusion in the* $H \to WW \to \ell\nu\ell\nu$ *Channel*, CMS NOTE 2007/011;
F. Beaudette *et al.*, *Search for a Light Standard Model Higgs Boson in the* $H \to WW^* \to e^+\nu e^-\bar{\nu}$ *Channel*, CMS NOTE 2006/114;
G. Davatz, M. Dittmar and A.-S. Giolo-Nicollerat, *Standard Model Higgs Discovery Potential of CMS in the* $H \to WW \to \ell\nu\ell\nu$ *Channel*, CMS NOTE 2006/047.

[57] S. Baffioni *et al.*, *Discovery potential for the SM Higgs boson in the* $H \to ZZ^{(*)} \to e^+e^-e^+e^-$ *decay channel*, CMS NOTE 2006/115;
D. Futyan and D. Giordano, *Search for the Standard Model Higgs Boson in the Two-Electron and Two-Muon Final State with CMS*, CMS NOTE 2006/136.

[58] M. Sani, *Search for the Standard Model Higgs Boson in four-Muon final state with CMS*, CMS CR-2004/035, proceedings of *Physics at LHC*, Vienna, Austria, July 2004.

[59] V. Bartsch, *Simulation of Silicon Sensors and Study of the Higgs Decay* $H \to ZZ \to 4\mu$ *for CMS (LHC)*, Ph.D. thesis, IEKP-KA/2003-26 University of Karlsruhe (2003).

[60] T. Sjostrand, L. Lonnblad and S. Mrenna, *PYTHIA 6.2 Physics and Manual, report LU-TP-01-21*, Aug 2001, arXiv:hep-ph/0108264.

[61] CMKIN, *CMS Interface for Event Generators*, http://cmsdoc.cern.ch/cmsoo/projects/CMKIN.

[62] E. Barberio and Z. Was, Computer Phys. Commun. 79 (1994) 291; E. Barberio, J. van Eijk and Z. Was, Computer Phys. Commun. 66 (1991) 115.

[63] Particle Data Group, Review of Particle Properties, Phys. Lett. B 562 (2004) 1.

[64] C. Zecher, T. Matsuura and J.J. van der Bij, Zeit. fur Phys. C 64 (1994) 219.

[65] CompHEP collaboration, *CompHEP: A package for evaluation of Feynman diagrams and integration over multi-particle phase space. User's manual for version 33*, arXiv:hep-ph/9908288.

[66] F. Maltoni, *Theoretical Issues and Aims at the Tevatron and LHC*, proceedings of the *1st Hadron Collider Physics Symposium (HCP 2005)*, Les Diablerets, Switzerland, July 2005.

[67] J. M. Campbell, arXiv:hep-ph/0105226, *W/Z + B anti-B / jets at NLO using the Monte Carlo MCFM*.

[68] S. Abdullin *et al.*, *Relative contribution of t- and s-channels to the* $ZZ \to 4\mu$ *process*, CMS NOTE-2006/057.

[69] P. Bartalini *et al.*, *NLO vs. LO: kinematical differences for signal and background in the* $H \to ZZ^{(*)} \to 4\mu$ *analysis*, CMS NOTE 2006/130.

[70] F. Maltoni and T. Stelzer, *MadEvent: Automatic Event Generation with MadGraph*, arXiv:hep-ph/0208156, JHEP 0302 (2003) 027.

[71] S.R. Slabospitsky and L. Sonnenschein, *TopREX 4.12*, Comput. Phys. Commun. 148 (2002) 87.

[72] OSCAR, *Object-oriented Simulation for CMS Analysis and Reconstruction*, http://cmsdoc.cern.ch/OSCAR.

[73] ORCA, *Object-oriented Reconstruction for CMS Analysis*, http://cmsdoc.cern.ch/ORCA.

[74] S. Abdullin *et al.*, *Search strategy for the Standard Model Higgs boson in the* $H \to ZZ^{(*)} \to 4\mu$ *decay channel using M(4*μ*)-dependent cuts*, CMS NOTE 2006/122.

[75] CMS Physics TDR, Volume I, CERN-LHCC-2006-001 (2006); section 3.4.7. (page 127).

[76] D. Acosta *et al.*, *Measuring Muon Reconstruction Efficiency from Data*, CMS NOTE-2006/060; S. Abdullin *et al.*, *Sensitivity of the Muon Isolation Cut Efficiency to the Underlying Event Uncertainties*, CMS NOTE-2006/033.

[77] CMS Muon TDR, CERN-LHCC-1997-32 (1997).

[78] A.L. Read, *Modified Frequentist Analysis of Search Results (The CLs Method)*, in the *1st Workshop on Confidence Limits* (2000), CERN, Geneva, Eds. L. Lyons, Y. Perrin and F. James, CERN-EP/2000-005.

[79] S. Abdullin *et al.*, *Study of PDF and QCD scale uncertainties in* $pp \to ZZ \to 4\mu$ *events at the LHC*, CMS NOTE-2006/068.

[80] V. Drollinger and A. Sopczak, *Comparison of Higgs boson mass and width determination of the LHC and a linear collider*, Eur. Phys. Jour. direct C3 (2001).

[81] CMS Physics TDR, Volume I, CERN-LHCC-2006-001 (2006); sections 3.6.4. (page 144), and 9.1.3. (pages 334-342).